Portable MRI and ^{129}Xe Signal Amplification by Gas Extraction

by

Dominic Michael Graziani

A dissertation submitted in partial satisfaction of the
requirements for the degree of
Doctor of Philosophy

in

Chemistry

in the

GRADUATE DIVISION
of the
UNIVERSITY OF CALIFORNIA, BERKELEY

Committee in charge:
Professor Alexander Pines, Chair
Professor David Wemmer
Professor Jeffrey Reimer

Spring 2011

Portable MRI and ^{129}Xe Signal Amplification by Gas Extraction

Abstract

Portable MRI and ^{129}Xe Signal Amplification by Gas Extraction

by

Dominic Michael Graziani

Doctor of Philosophy in Chemistry

University of California, Berkeley

Professor Alexander Pines, Chair

Magnetic resonance has had an impact on nearly every branch of science from fundamental physics to neurobiology. Despite its pervasiveness, it remains a relatively inaccessible technique due to the costs associated with the powerful and highly precise instrumentation needed for sensitive detection. In this work, two techniques focused on improving the accessibility of magnetic resonance are presented. First, a low cost and portable volume imaging system is described with the unique ability to scan the homogeneous region of the magnetic field through a sample of interest. This system addresses the fundamental challenge of producing a compact imaging sensor while maintaining a sensitive region large enough to extract relevant information from the sample. The design of a suitable set of single-sided gradient coils compatible with the adjustable imaging system is presented first, followed by imaging results obtained with this apparatus. The second technique described in this work involves the use of xenon as a chemical sensor. Xenon's chemical shift sensitivity to its environment make it and ideal probe of its surroundings. Spin exchange optical pumping has made detection of dilute xenon solutions possible through hyperpolarization. However, optical pumping requires high power circularly polarized laser light, limiting applications of xenon from widespread use. An alternative method for signal amplification is presented, in which xenon is extracted from solution and compressed prior to detection. A description of the method is followed by several applications as well as a detailed description of the apparatus involved in the gas extraction and compression technique.

To my parents,
for their unconditional support.

Contents

List of Figures

Acknowledgments

The work presented in this thesis would not have been possible without the professional and personal support of many people. First and foremost, I would like to thank my adviser, Alex Pines. Alex's expertise and passion for science is truly inspiring, and the academic environment he has fostered is unparalleled. His enthusiasm permeates throughout the group of post-docs, graduate students, undergrads, and visiting scholars collectively known as the "Pinenuts." The vast majority of my learning in graduate school has been from interacting with fellow Pinenuts, and I am forever indebted to them. I would especially like to thank Xin Zhou, with whom I worked on the xenon projects presented in this thesis. No matter how busy he was with writing book chapters, setting up a new lab, and raising two kids, he would always make time to teach me something new, listen to an idea, or help with an experiment. I greatly appreciate his generosity. I also owe a great deal to Alyse Jacobson for her work (often behind the scenes) in keeping the lab running smoothly on a day to day basis. Outside of the group, I'd like to thank the rest of my committee members, Dave Wemmer and Jeff Reimer, for critical feedback of my work.

I would never have even attempted this journey if not for the encouragement of two people. As an undergraduate at UCSD with no research experience and a mediocre GPA, Bob Continetti took a chance and gave me the opportunity to experience academic research through a summer position in his group. I ended up working in his lab for two more years, during which he was very generous with his support, both academically and financially. The origin of my career in science, I owe to Batman - better known by his alter ego, Mr. Gibbons. I cannot imagine another teacher making a subject as potentially dull as A.P. physics so exciting and fun on a daily basis.

I had the somewhat rare opportunity to attend graduate school within a short drive of the majority of my family. I cannot express thoroughly enough the gratitude I have for their love and support during this process. I'd also like to thank Stephanie, not only for her patience, but also for her beautiful smile which could brighten even the worst day of null results and broken equipment. Finally, to those who know me as "F.D.N." - Thanks...I think?

Abbreviations

CEST	Chemical Exchange Saturation Transfer
CPMG	Carr-Purcell-Meiboom-Gill
DNP	Dynamic Nuclear Polarization
EMF	Electromotive Force
MR	Magnetic Resonance
MRI	Magnetic Resonance Imaging
NMR	Nuclear Magnetic Resonance
PCB	Printed Circuit Board
PHIP	Para-Hydrogen Induced Polarization
RF	Radio Frequency
SAGE	Signal Amplification by Gas Extraction
SEOP	Spin Exchange Optical Pumping
SNR	Signal to Noise Ratio
SQUID	Superconducting Quantum Interference Device
TOF	Time of Flight

Chapter 1

Introduction to portable magnetic resonance imaging

1.1 Background

Since the discovery of nuclear magnetic resonance in the 1940s [11, 83], no other form of spectroscopy has had such a broad impact across all branches of science. The entire field has originated from a curiosity in physics, since at its root, NMR is based on a purely quantum mechanical phenomenon, the concept of spin. Upon the discovery of the chemical shift in the late 40s and early 50s [81, 25, 85], NMR spectroscopy blossomed as a technique for probing the chemical structure of molecules. Today it is arguably the single most important analytical tool for synthetic chemistry. The geophysics community has utilized NMR in another form, relaxometry, to probe the internal structures of oil well formations for decades [50, 49]. More recently, magnetic resonance has been applied in biology to probe the structure and function of proteins [9, 105, 19] and to trace complex metabolic processes [96, 80]. With the development of magnetic resonance imaging in the 1970s [52, 57, 23], the technique has made remarkable breakthroughs in medicine by providing a means to non-invasively study anatomy and physiology with unprecedented contrast. Even psychology, a field tangled in complexity when compared to the basic physics describing NMR, has benefited greatly through the development of functional imaging techniques.

From probing the elementary physical properties of the universe to examining the complex thoughts of a specific human being, there is no questioning the impact and versatility of magnetic resonance. None of these innovations would be possible, however, without the remarkable advances in the NMR instrumentation itself over the past 60+ years. Present day superconducting magnets can produce ultra-stable fields up to nearly 25 Tesla with variations of only one part in a billion. The electronics involved in pulse programming and data acquisition exhibit picosecond precision in order to achieve phase control to a fraction of a degree. Modern amplifiers are regularly achieving several kilowatts of radio frequency power and hundreds of amps of direct current in fractions of a second. All of these components are required when attempting to resolve one of hundreds of NMR active

sites in a protein or a microscopic tumor in the brain. However, this level of performance comes at the cost of accessibility. Conventional MR spectroscopy and imaging systems can cost upwards of several million dollars. The large superconducting magnets and high power electronics involved make the systems intrinsically non-portable and the cryogens required for the superconducting wire limits the installation geography to areas that have reasonable access to liquid helium. These limitations, have motivated scientists and engineers to push the envelope of what can be accomplished with a low cost, portable, non-cryogenic system. With recent advances in the production of high-quality, powerful rare earth magnets and low cost miniature electronics, portable magnetic resonance has become a budding field.

1.2 Challenges

The advantages of portable low cost magnetic resonance sensors are clear, but significant challenges exist in creating a practical device. Portability comes at the cost of lower field strengths, reduced homogeneity, and for imaging, smaller sensitive regions. The consequences of these sacrifices along with potential solutions will be examined in the following sections.

1.2.1 Weak magnetic fields

Superconducting magnets are not ideal for portable magnetic resonance sensor designs. A significant amount of bulk and weight must be utilized for thermal insulation, fundamentally limiting portability. Additionally, the magnets are expensive and require cryogens, making them less stable for transportation and limited to developed areas with access to liquid helium. Similarly, a powerful resistive magnet is limited by the size, weight, and energy requirements of a power supply. Such a magnet would also likely need a substantial cooling system, adding to the complexity, cost, and size of the system. This leaves the relatively weak fields of permanent magnets ranging from the 0.5 G magnetic field of the earth, to at best, the 1.4 T remanent field of a NdFeB rare earth magnet. These limited field strengths have a significant effect on the signal intensity of a magnetic resonance experiment. Traditionally, NMR detection is done with a resonant circuit including a coil of wire surrounding the sample of interest. With such an arrangement, the magnitude of the voltage induced in the circuit from the sample is proportional to the time derivative of the magnetic flux in the coil

$$|\varepsilon| \propto \left| \frac{d\Phi}{dt} \right| \tag{1.1}$$

where ε is the EMF, and Φ is the magnetic flux. Because of the time derivative dependence, inductive detection is proportional to the nuclear frequency of oscillation, known as the Larmor frequency ω_0. The Larmor frequency is described by

$$\omega_0 = \gamma B_0 \tag{1.2}$$

where γ is the gyromagnetic ratio of the nucleus and B_0 is the applied magnetic field. It therefore follows that the magnitude of the inductively detected signal is at least proportional to the magnetic field strength. However, the magnetic flux itself is also dependent upon the applied field since the magnetization of the sample can be described by [19]

$$M_0 \approx \frac{N\gamma^2\hbar^2 B_0}{4k_B T} \tag{1.3}$$

for spin $1/2$ nuclei, the most commonly studied nuclei in magnetic resonance. N is the number of spins in the sample, $\hbar$ is Plank's constant divided by 2π, k_B is Boltzmann's constant, and T is the temperature of the sample. The signal then scales as the square of the magnetic field, which can be significant, even when comparing a modest high field system of 9.4 T, to the highest attainable field with a permanent magnet of 1.4 T (Fig. 1.1).
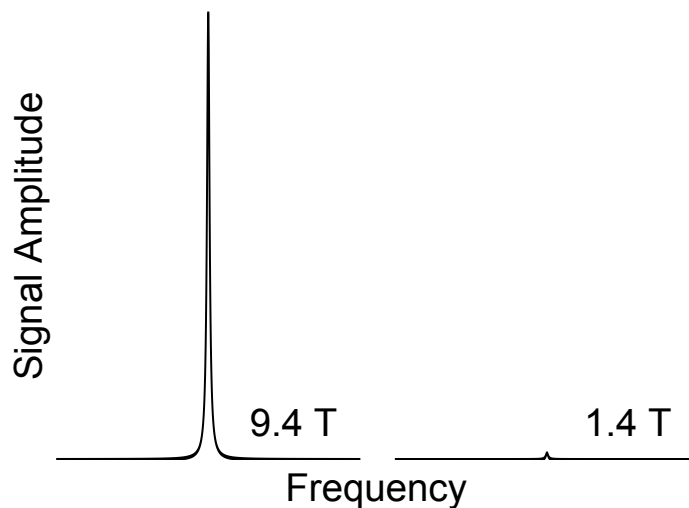
Figure 1.1: Magnitude of the NMR signal from a sample at a modest superconducting magnetic field strength of 9.4 T (left) compared to the signal from a sample in a 1.4 T field (right), the highest field attainable with a rare earth permanent magnet. Because of the B_0^2 dependence, the signal is dramatically reduced.

The considerable decrease in the signal to noise ratio when moving to lower fields is arguably the single most significant barrier to widespread adoption of portable magnetic resonance systems. However, technologies are currently being developed which can alleviate this limitation. Devices which measure magnetic flux directly, such as superconducting quantum interference devices (SQUIDs) [29] and atomic magnetometers [15, 62] are essentially field independent in terms of sensitivity. As such, the performance of such devices can be significantly better than inductive detectors at fields below $\sim$1 T as can be seen in figure 1.2. Magnetic resonance experiments using these non-inductive detectors have shown substantial improvements in sensitivity [98, 91, 110].
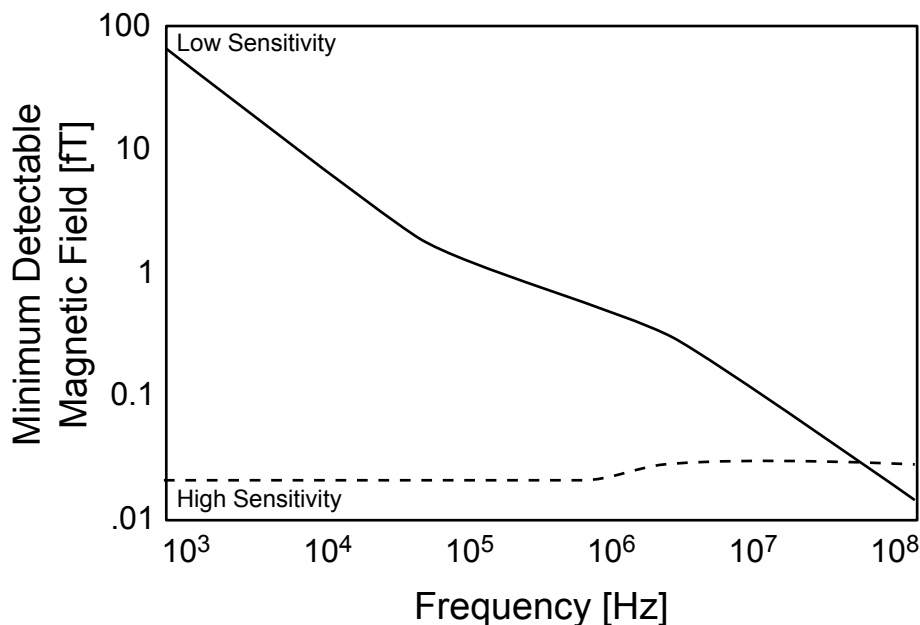
Figure 1.2: Comparison of the sensitivity of non-inductive (dashed line) and inductive (solid line) detection versus frequency. Figure adapted from Savukov et al. [92]

.

In addition to non-inductive detection, hyperpolarization techniques are making substantial gains in sensitivity. By transferring angular momentum from a highly polarized system to the sample of interest, the magnetization of the sample can be enhanced beyond the thermal equilibrium dictated by the Boltzmann distribution. Spin exchange optical pumping (SEOP) [33] of noble gases and parahydrogen induced polarization (PHIP) [14] are especially attractive for portable magnetic resonance systems since the maximum polarization attainable in these techniques is field independent. Dynamic nuclear polarization (DNP) [56] is less attractive, since at its root, it relies on the thermal polarization of the electron and therefore benefits greatly from large magnetic fields. Despite this characteristic, DNP may be a valuable technique at moderate field strengths produced by permanent magnet arrays. As opposed to non-inductive detection techniques which have the potential to enhance the sensitivity of any magnetic resonance experiment, hyperpolarization techniques would likely be limited to specialized acquisition schemes. However, as hyperpolarization methods gain widespread use and more of these acquisition schemes are developed, it's no doubt that the combination of non-inductive detection and hyperpolization could make for a highly sensitive portable sensor.

1.2.2 Inhomogeneous fields

Inhomogeneous magnetic fields pose another significant challenge for the development of a low cost portable magnetic resonance system. The magnetization of permanent magnets

generally varies slightly over the volume of the magnet, and even the highly uniform magnetic field produced by the earth is easily distorted by ferromagnetic building materials and other items common in inhabited areas. Since the frequency of the NMR signal is proportional to the magnetic field strength (Eqn. 1.2.1), a distribution of magnetic field values will manifest in a distribution of NMR frequencies. The effect of the inhomogeneities then is to broaden the signal and reduce the peak amplitude. This of coarse poses a problem as a large portion of the signal falls below the noise threshold.
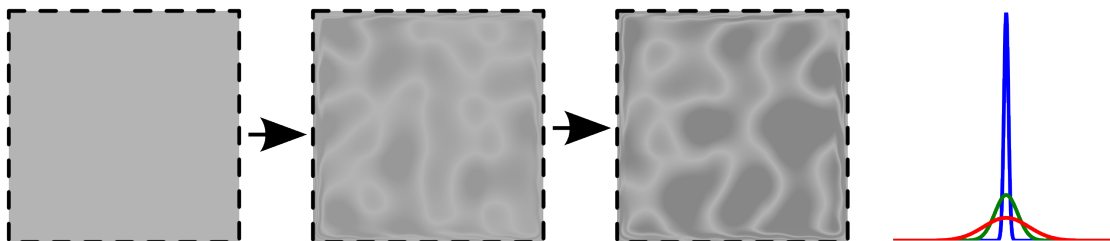
Figure 1.3: Effect of inhomgeneity on the NMR signal. As the magnetic field becomes less and less homogeneous, the signal broadens, reducing the peak amplitude.

Fortunately, the dephasing caused by static field inhomegeities can be reversed by applying a Hahn echo [36] as seen in figure 1.4. When these echoes are performed in rapid succession, called an echo train (or depending on the phase of the pulses a CPMG train [17, 66]), much of the signal can be recovered. By summing over the collected echoes, the SNR can approach that of the same spectrum acquired in a homogeneous field. There is a limitation however. When dealing with diffusive samples such as liquids and gases, the magnetic field experienced by a given nucleus changes over time as the molecule undergoes Brownian motion and diffuses through the magnetic field inhomogeneities. Because the field is changing over time, the spins are not precisely refocused during an echo, and the echo amplitudes are attenuated over the course of the echo train. This is known as diffusion attenuation and can be described by the following formula using a uniform gradient field in one dimension to simplify the calculation [17]

$$M_{xy}(t) = M_0 e^{\left(-\gamma^2 G^2 D t^3 / 12 n^2\right)} \tag{1.4}$$

where $M_{xy}(t)$ is the transverse magnetization at the peak of each echo (ignoring other forms of relaxation), M_0 is the initial magnetization, G is the magnitude of the gradient, D is the diffusion coefficient, and n is the number of refocusing pulses or echoes making up the echo train. Two things are immediately obvious from this equation. First, the squared dependence on the magnitude of the gradient in the exponential means even moderate gradients can have devastating consequences in terms of diffusion attenuation. Second, when the number of refocusing pulses becomes large, the effects of diffusion attenuation are negligible. If the time between echoes is short compared to the correlation time for Brownian motion, the field experienced by each nucleus after the refocusing pulse is highly correlated to the field
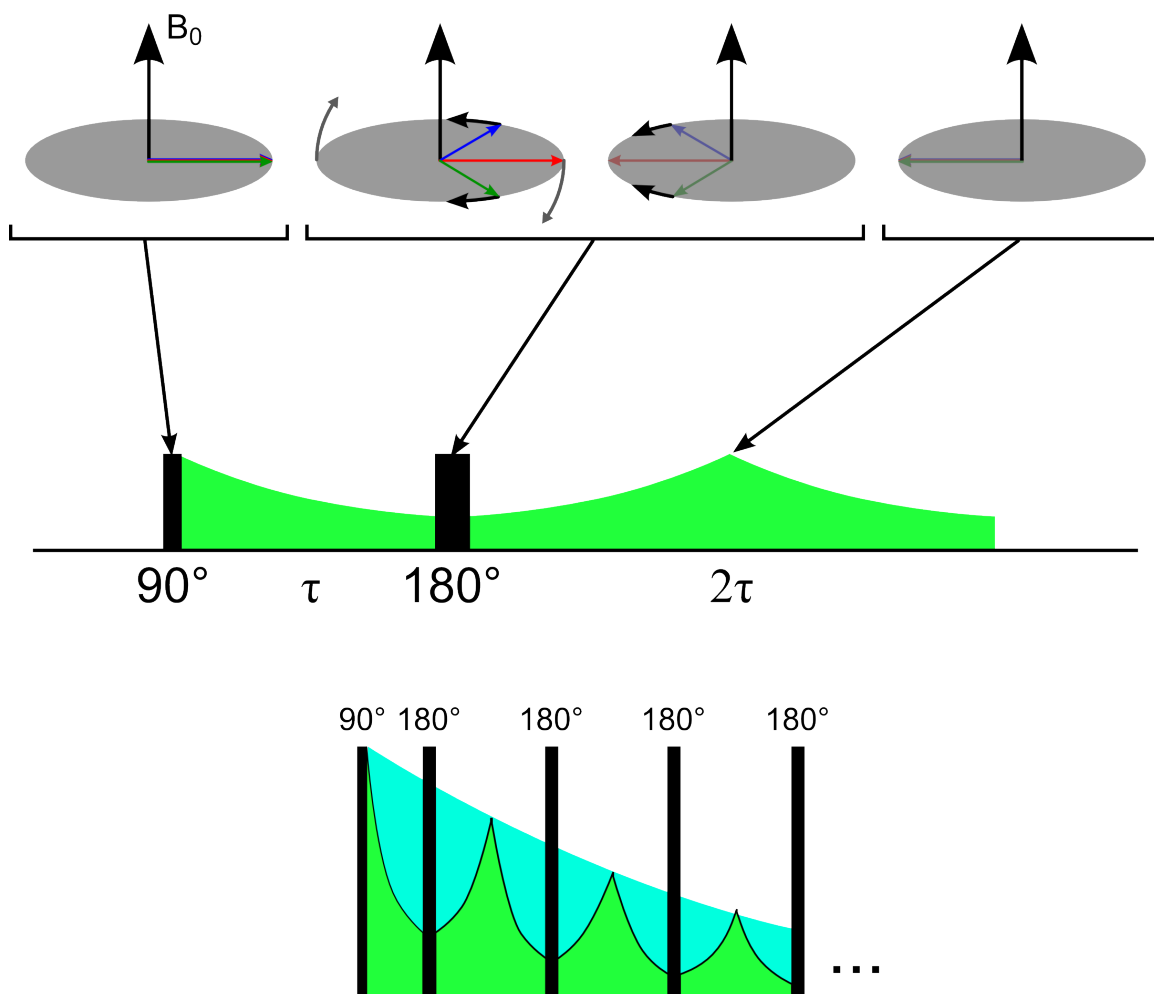
Figure 1.4: **Top:** vector schematic of a Hahn echo. Once excited, all isochrmats (colored arrows) are in phase in the transverse plane. Because the various isochromats oscillate at different frequencies, they disperse over time from the average field isochromat (red). After a time τ, a 180° pulse is applied, flipping the isochromats in the transverse plane. Although they are now a mirror image of their state before the 180° pulse, they are still experiencing the same magnetic field as before the pulse and continue to move in the same direction relative to each other. After another time τ, the isochromats have refocused in the transverse plane. **Middle:** RF pulse sequence showing the initial decay of the signal over the first interval τ due to dispersion. After the 180° pulse, the signal begins to accrue until it is completely refocused after a second interval of τ, at which point it begins to dephase again. **Bottom:** Shown in blue is the natural decay of the signal due to T_2 relaxation in a homogeneous field. The green signal represents the same sample but now being continuously refocused in an inhomogeneous field. From this figure, it is clear that with rapid refocusing, a majority of the signal intensity can be recovered.

experienced before the pulse, and the spins are then effectively rephased. There is, however, a practical limit to the number of echoes that can be acquired since the excitation pulses have a finite pulse width. Additionally, there are generally experimental imperfections such as electronic and mechanical ringing from the high power RF pulses that need to dissipate before acquiring the weak NMR signals. In general, with reasonable field gradients, signals from moderately diffusive samples such as water can be acquired with only a minimal loss in SNR due to inhomogeneous fields.

Besides the effect that broadening has on the peak amplitude, the increased line widths themselves are a considerable challenge to overcome. Traditional NMR spectroscopy relies on very narrow, well resolved lines to extract as much chemical information as possible from a molecule. With the inhomogeneous fields involved in portable magnetic resonance, the information is typically blurred beyond recognition (Fig. 1.5). This issue is exacerbated by the fact that the chemical shift is proportional to the magnetic field strength so the signals are already close together at low fields. Although the Hahn echo is capable of refocusing the effects of the static magnetic field responsible for broadening, it also refocuses any evolution due to chemical shift and the information cannot be recovered. The effect is prevalent with imaging experiments as well and manifests as a blurred image along the frequency encoding dimension. Additionally, if the static field gradients are greater than the uniform gradient field pulses responsible for spatial encoding, frequency encoding is not possible. In this case imaging must be done with pure phase encoding techniques, adding an additional dimension to the experiment and slowing it down considerably.
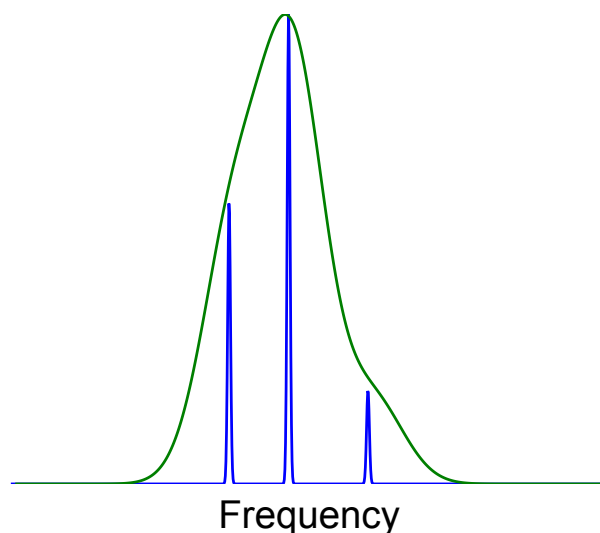
Figure 1.5: The effect of inhomogeneous magnetic fields on chemical information. A spectrum acquired in a uniform field (blue) shows three highly resolved peaks. When the same sample is placed in a non-uniform field, the signal (green) is blurred such that none of the three original peaks can be distinguished. The amplitude of each spectrum was scaled by its intensity for the sake of visualization.

In order to extract relevant information from samples in these relatively low and inhomogeneous fields, a variety of approaches have been developed. Relaxation information can provide a wealth of information and has been used in the oil industry for decades to determine properties of well formations such as porosity, permeability, as well as relative water, oil, and gas content [50]. Significant efforts have also been made to shim permanent magnet arrays to a high enough degree of uniformity to perform traditional NMR spectroscopy and imaging experiments [79, 24]. RF pulse sequences have also been developed that take advantage of correlations between static field inhomogeneities and RF field inhomogeneities in order to extract chemical spectroscopic information [68, 104, 30].

1.2.3   Limited sensitive region

Another major challenge to low field portable magnetic resonance is producing a large sensitive region while maintaining a compact and portable design. For spectroscopy this is not especially important since a larger sensitive region will simply correspond to higher SNR assuming enough sample is available to fill that volume. Imaging on the other hand benefits greatly from a large sensitive region which directly corresponds to the size of samples that can be studied. It is fruitful at this point to compare the different families of portable imaging magnets. The ultimate in portability is utilizing the earth's magnetic field. This magnet comes pre-installed everywhere and is uniform over very large volumes making it ideal to study samples of all different shapes and sizes. However, because the field is so weak, the sensitivity of such a system will be low, and the utility of this design will rely primarily on the advancement of non-inductive detection and hyperpolarization techniques. This leaves magnets constructed from rare earth permanent magnets. These permanent magnet arrays come in two main varieties. The first is an enclosed array of magnets in which the field of interest resides in the bore of the array, such as a Halbach magnet. These magnets benefit from relatively strong and uniform fields produced by the constructive interference of each magnet in the array, but are limited to samples that can fit in the bore of the magnet. The second variety are the so called "ex-situ," "inside-out," or simply "single-sided" magnet designs in which the field of interest is not enclosed by the magnet array. These magnets benefit from an open geometry which enables the study of almost any sample, but they suffer from intrinsically inhomogeneous fields. Because of the versatility provided by the open design, we will focus on the use of single-sided magnets for the task of portable imaging.

Despite the open geometry, single-sided sensors still suffer from limited sensitive regions. Unlike conventional high field imaging, where the maximum field of view is primarily determined by the dimensions of the RF coil, the maximum field of view in a portable system with a relatively inhomogeneous field is determined primarily by its bandwidth. As a tuned circuit, the RF coil is only sensitive to a range of frequencies determined by the full width at half maximum of the transmission curve of the circuit (Fig. 1.6).

In terms of single-sided magnet designs, there are two general approaches. The first is a simple bar magnet design which produces a dipolar field that decays from the surface of the magnet. With this geometry, the resulting sensitive region corresponds to a narrow slice
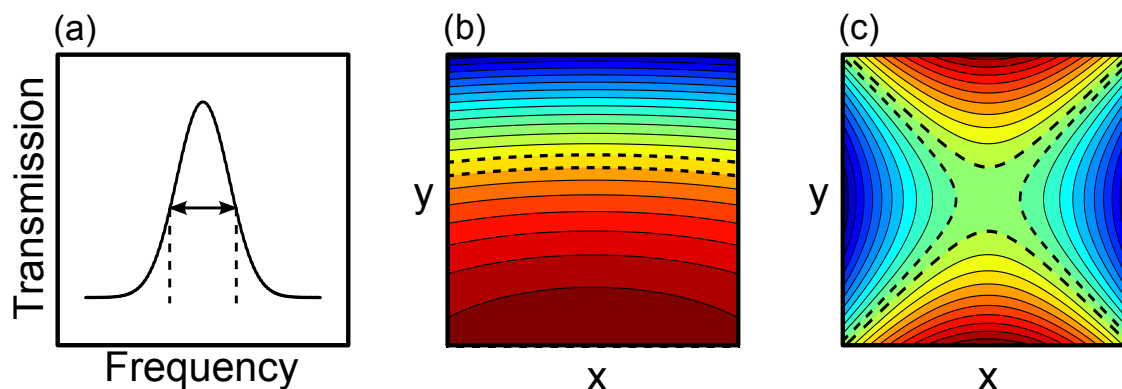
Figure 1.6: Restricted fields of view dictated by the resonant circuit bandwidth. (a) Typical transmission response of an LC circuit. This type of circuit is primarily sensitive to the frequencies falling within the full width at half maximum of the curve. (b) Magnetic field profile for a typical dipolar magnet design. The contour highlighted with dashed lines falls within the bandwidth of the tuned circuit and represents the sensitive region of the magnet. (c) Same as (b), but for a quadrupolar magnetic field profile.

running parallel to the dipole of the magnet. Additionally, the effective size of the sensitive region can be adjusted by changing the resonant frequency of the RF circuit. By doing so, various slices can be excited at various distances from the surface of the magnet. The other approach to single-sided magnet designs is to use two or more magnet elements in an orientation that creates a quadrupolar field profile. This geometry produces a relatively homogeneous volume that resembles a hyperbolic function as can be seen in figure 1.6 (c). The relatively uniform volume means diffusion attenuation is reduced, and this type of sensor is therefore more suitable for studying diffusive samples such as water and biological tissue. However, unlike the dipolar magnet design, changing the resonant frequency would simply excite shells of the original sensitive volume, and is not an efficient way to increase the field of view. Instead, a magnet design made up of adjustable elements was developed and is capable of producing homogeneous volumes over a continuous range of positions above the surface of the magnet. Such a design provides the accessibility and portability of a single-sided geometry, while reducing effects of diffusion attenuation and maintaining a reasonably sized imaging volume. A brief overview of the magnet design is described in the following section. A detailed description of the design can be found in reference [77], and imaging results obtained with this magnet are described in chapter 3.

1.3   Single-sided adjustable sensor

The underlying principle in the development of a single-sided volume imaging magnet with a movable sensitive region is an array of magnetic elements which are independently adjustable. The design chosen was an array of four cylindrical NdFeB magnets with their respective dipoles oriented perpendicular to the cylindrical axes. Each element was mounted

in the magnet chassis in such a way that they could be rotated 360° about the cylindrical axis. For a detailed description and technical drawings of the magnet housing, see reference [75]. In order to determine the optimal orientations for each magnet rod, a least squared target field inversion technique was utilized. First, a target field is specified with a given field profile and spatial coordinates. For this magnet, the target field is a uniform field centered somewhere above the surface of the magnet. The total magnetic field in this region can be broken down into the vector sum of the dipolar fields contributed by each magnetic rod. Furthermore, each dipole can be broken down into its vector components providing a finite basis set for least squared regression (Fig. 1.7). The regression is constrained since each magnetic dipole has a fixed magnitude. The final dimensions of magnet array including the mechanical housing are 6 cm tall, by 23 cm along the cylindrical axis, and 16 cm deep. It is capable of producing a 5-10 cm^3 imaging volume up to 10 cm from the surface of the magnet. The next step, and the subject of the following chapter, is producing a set of single-sided gradient coils which are compatible with the adjustable nature of the magnet.
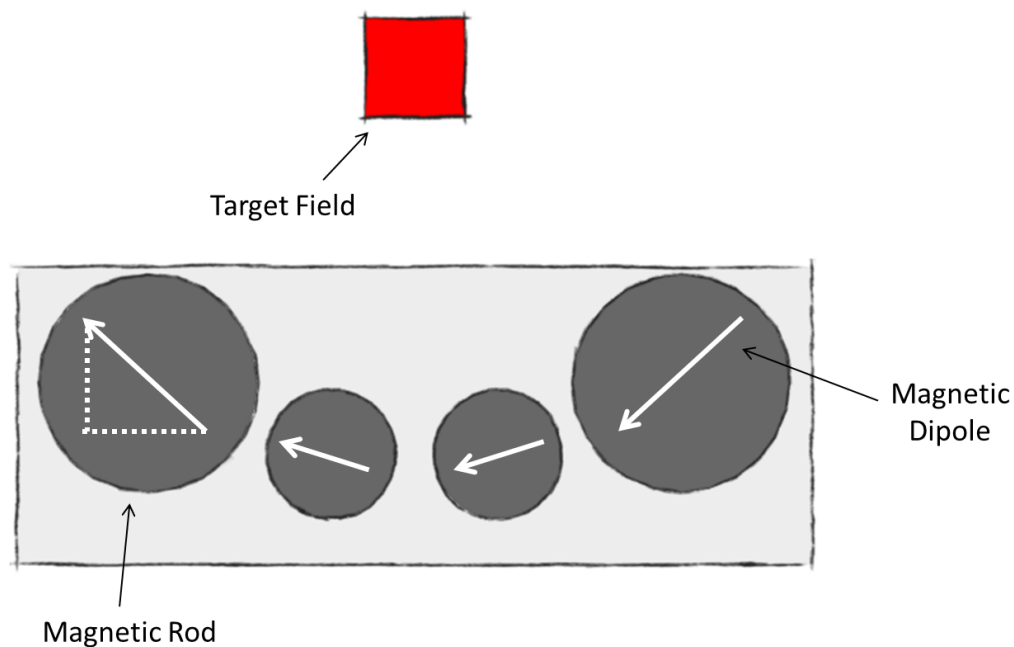
Figure 1.7: Adjustable single-sided magnet concept. The magnet consists of four cylindrical magnets magnetized perpendicular to their cylindrical axes (gray circles). They are mounted in a mechanical chassis (gray rectangle) which allows for independent rotation of each element. To determine the precise relative orientations, a target field is specified (red box) and a least squared regression is performed using the vector components of each dipolar field as the basis set.

Chapter 2

Uniplanar gradient coil design

2.1 Introduction

In designing gradient coils for an adjustable single-sided imaging system, several factors need to be taken into account. First of all, the design needs to be computer optimized. Most importantly, this ensures that the final product is the optimal design given the restraints of the geometry. Secondarily, it allows for fast production of multiple sets of coils to accommodate the various imaging volumes producible by the adjustable magnet. The second consideration is the geometry itself. A hemispherical coil design would provide a strong and relatively homogeneous gradient field [34] and is ideal in situations where the imaging volume is a significant distant from the surface of the magnet. However, such a geometry would require a different physical design for each imaging volume, and wouldn't be able to accommodate imaging volumes at the surface of the magnet without sacrificing the open design. A uniplanar design sacrifices field strength and homogeneity for simplicity and robustness. Uniplanar gradients can be easily manufactured with commercial printed circuit board (PCB) techniques, and the same geometry can accommodate imaging volumes at a variety of positions above the magnet.

The computer optimization of a gradient coil design involves inverting a specified magnetic field into a current density on a surface, also known as a target field approach. This technique has been thoroughly developed for a variety of coil geometries including cylindrical [106], spherical [54], and biplanar [60]. Optimizations for uniplanar geometries have also been developed [2], primarily for the medical imaging community. For conventional cylindrical coils, the gradient power scales approximately as the fifth power of the diameter of the coil [107]. Because of this, there is a strong motivation to explore alternative geometries which can accommodate a large sample, such as a human, at much lower powers. The compact nature of uniplanar gradients allows for a much larger gradient strength for a given power. For medical imaging, maximum gradient strength is the ultimate goal, but for single-sided MRI, power efficiency is the primary objective. To maintain portability, low power systems are required for both their compact nature and energy efficiency, especially if the device will be running off of battery power.

Uniplanar gradient coils can be optimized for a variety of parameters. Arguably the most important characteristic of the design should be field linearity in order to minimize image distortions. Other parameters to consider are inductance, force, power density, and restricted geometry. Minimizing the inductance of a set of gradient coils maximizes the switching times or slew rates. This is an important factor for high field conventional imaging as it allows for fast imaging techniques such as echo planar imaging [100]. Fast imaging sequences are difficult if not impossible at low field simply because the signal to noise ratio is too small. However, fast switching times are still important in order to minimize additional signal lost due to T_2 relaxation. The force experienced by the coil is an important consideration at high field as the coupling between the pulsed magnetic field of the gradient coil and the static field of the magnet can tear the coil apart. With the lower magnetic fields and gradient powers of single-sided portable MRI, this optimization becomes unnecessary. Likewise, in most cases, optimal power density is not as important a factor at low field because of the reduced duty cycle involved in "slow" imaging techniques. Restricting the geometry of uniplanar gradient designs adds considerable complexity to the inversion problem, but it may be necessary to produce the most compact designs. For the set of coils described in this chapter, geometric restriction was not required as sufficient space was available for the design relative to size of the imaging sensitive volume. Maximum linearity and the lowest possible inductance were decided to be the most important parameters to optimize in the design of uniplanar gradients for single-sided portable imaging.

The technique described in the following sections is an extension of a biplanar gradient coil design described in Martens et al. [60] to a uniplanar geometry. The stored energy of the system, or equivalently, the inductance is minimized while constraining the magnetic field to a specified geometry.

2.2 Theory

The target field approach to gradient design involves three steps (Figure 2.1), each of which will be described in detail below. First, the location and geometry of a desired field is specified. The field is then mathematically inverted into a current density on a surface. For uniplanar gradient coils, that surface is simply a plane. The inversion is done by minimizing a cost function subject to a set of constraints. For the method described below, the stored energy of the system is minimized subject to the constraint that the field that is ultimately produced matches the target field at a specified set of points. The second step in the optimization is taking the resulting continuous current density from step one and discretizing it into a set of wires. This can easily be done with a streamline method [107]. The final step involves verifying the discretized current reproduces the desired target field. This is also easily done by numerically evaluating the Biot-Savart law. The code for implementing the three steps described above can be found in appendix A.
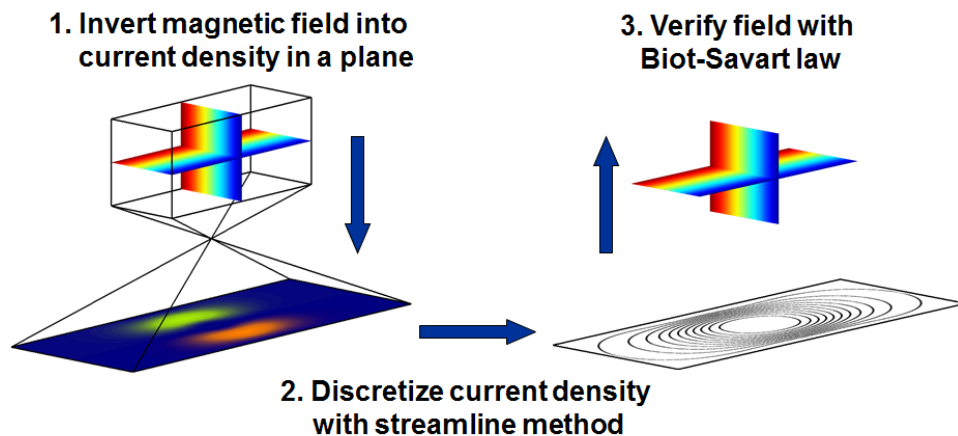
Figure 2.1: Diagram of the three steps involved in the target field approach to uniplanar gradient coil design.
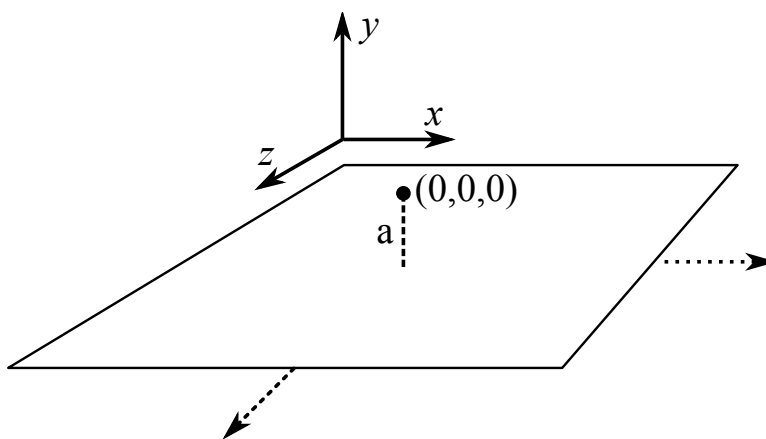
Figure 2.2: Coordinate system for uniplanar gradient coil design. The target field is centered about the origin and the current density is restricted to the $y = -a$ plane.

2.2.1 Inversion

We start by defining the coordinate system for our apparatus (Figure 2.2). The static magnetic field was designed to be parallel with the surface of the magnet. To be consistent with conventional high field NMR, this dimension will be defined as z. The x coordinate will arbitrarily be assigned to the other parallel dimension, leaving y perpendicular to the face of the magnet. For this optimization, the target field will be centered about the origin and the current density will be restricted to the $y = -a$ plane. To start, an equation needs to be derived relating the magnetic field to the current density defined as

$$\mathbf{J}(\mathbf{r}) = [J_x(x, z)\hat{x} + J_z(x, z)\hat{z}]\delta(y + a) \tag{2.1}$$

Starting from Maxwell's equations

$$\nabla \cdot \mathbf{E} = \frac{\varrho}{\epsilon_0} \tag{2.2}$$

$$\nabla \cdot \mathbf{B} = 0 \tag{2.3}$$

$$\nabla \times \mathbf{E} = -\frac{\partial \mathbf{B}}{\partial t} \tag{2.4}$$

$$\nabla \times \mathbf{B} = \mu_0 \left(\mathbf{J} + \epsilon_0 \frac{\partial \mathbf{E}}{\partial t} \right) \tag{2.5}$$

Since the steady state magnetic field is all that we care about, the time derivatives all go to zero. This leaves the following two equations describing the magnetic field and current density.

$$\nabla \cdot \mathbf{B} = 0 \tag{2.6}$$

$$\nabla \times \mathbf{B} = \mu_0 \mathbf{J} \tag{2.7}$$

Equation 2.6 and the vector identity $\nabla \cdot (\nabla \times \mathbf{A})$, allow us to define $\mathbf{B}$ in terms of the curl of a vector potential $\mathbf{A}$.

$$\mathbf{B} = \nabla \times \mathbf{A} \tag{2.8}$$

Substituting equation 2.8 into equation 2.7 results in

$$\nabla \times (\nabla \times \mathbf{A}) = \mu_0 \mathbf{J} \tag{2.9}$$

Using another vector identity: $\nabla \times (\nabla \times \mathbf{A}) = \nabla (\nabla \cdot \mathbf{A}) - \nabla^2 \mathbf{A}$, equation 2.9 becomes

$$\nabla (\nabla \cdot \mathbf{A}) - \nabla^2 \mathbf{A} = \mu_0 \mathbf{J} \tag{2.10}$$

At this piont, it is important to note that since the curl of a gradient of a scalar is zero ($\nabla \times \nabla \psi = 0$), the vector potential $\mathbf{A}$ can be transformed to $\mathbf{A} - \nabla \psi$ without changing the magnetic field $\mathbf{B}$ in equation 2.8. This is called a gauge transformation. A result of this gauge invariance is that we are free to choose the value of $\nabla \cdot \mathbf{A}$. Choosing the Coulomb gauge of $\nabla \cdot \mathbf{A} = 0$ and substituting it into equation 2.10 results in a Poisson equation

$$\nabla^2 \mathbf{A} = -\mu_0 \mathbf{J} \tag{2.11}$$

The general solution to a Poisson equation is

$$\mathbf{A}(\mathbf{r}) = -\mu_0 \int G(\mathbf{r}, \mathbf{r}') \mathbf{J}(\mathbf{r}') d^3 \mathbf{r}' \tag{2.12}$$

Where $G(\mathbf{r}, \mathbf{r}')$ is a Green's function and is defined by

$$\nabla^2 G(\mathbf{r}, \mathbf{r}') = \delta(\mathbf{r} - \mathbf{r}') \tag{2.13}$$

One such function that satisfies equation 2.13 is

$$G(\mathbf{r}, \mathbf{r}') = -\frac{1}{4\pi|\mathbf{r} - \mathbf{r}'|} \tag{2.14}$$

The factor of -4π comes about from the Laplacian of $\frac{1}{|\mathbf{r}-\mathbf{r}'|}$

$$\nabla^2 \left(\frac{1}{|\mathbf{r} - \mathbf{r}'|} \right) = -4\pi\delta^3(\mathbf{r} - \mathbf{r}') \tag{2.15}$$

Substituting equation 2.14 into equation 2.12 results in a general expression relating the magnetic vector potential to current density

$$\mathbf{A}(\mathbf{r}) = \frac{\mu_0}{4\pi} \int_V \frac{1}{|\mathbf{r} - \mathbf{r}'|} \mathbf{J}(\mathbf{r}') d^3\mathbf{r}' \tag{2.16}$$

The calculation can be simplified by expanding the Green's function into its Fourier components

$$
\begin{aligned}
G(\mathbf{r}, \mathbf{r}') &= -\frac{1}{|\mathbf{r} - \mathbf{r}'|} \\
&= \frac{1}{2\pi} \int\limits_{-\infty}^{\infty} \int\limits_{-\infty}^{\infty} \frac{dk_x dk_z}{\sqrt{k_x^2 + k_z^2}} e^{ik_x(x-x')} e^{ik_z(z-z')} e^{-\sqrt{k_x^2+k_y^2}(y-y')}
\end{aligned} \tag{2.17}
$$

It is also useful at this point to define the Fourier transform pairs

$$j_x(k_x, k_z) = \int\limits_{-\infty}^{\infty} \int\limits_{-\infty}^{\infty} dx dz e^{-ik_x x} e^{-ik_z z} J_x(x, z) \tag{2.18}$$

$$J_x(x, z) = \frac{1}{4\pi^2} \int\limits_{-\infty}^{\infty} \int\limits_{-\infty}^{\infty} dk_x dk_z e^{ik_x x} e^{ik_z z} j_x(k_x, k_z) \tag{2.19}$$

and

$$j_z(k_x, k_z) = \int\limits_{-\infty}^{\infty} \int\limits_{-\infty}^{\infty} dx dz e^{-ik_x x} e^{-ik_z z} J_z(x, z) \tag{2.20}$$

$$J_z(x,z) = \frac{1}{4\pi^2} \int\limits_{-\infty}^{\infty} \int\limits_{-\infty}^{\infty} dk_x dk_z e^{ik_x x} e^{ik_z z} j_z(k_x, k_z) \tag{2.21}$$

Substituting equation 2.17 into equation 2.16, we get

$$\mathbf{A}(\mathbf{r}) = \frac{\mu_0}{8\pi^2} \int_{x'} \int_{y'} \int_{z'} dx' dy' dz' \mathbf{J}(\mathbf{r}') \dots$$
$$\int_{k_x} \int_{k_z} \frac{dk_x dk_z}{\sqrt{k_x^2 + k_z^2}} e^{ik_x(x-x')} e^{ik_z(z-z')} e^{-\sqrt{k_x^2+k_y^2}(y-y')} \tag{2.22}$$

By inserting equation 2.1 into equation 2.22, we will end up with two terms. For the sake of clarity, let us only examine the first term.

$$\mathbf{A}(\mathbf{r}) = \frac{\mu_0}{8\pi^2} \int_{x'} \int_{y'} \int_{z'} dx' dy' dz' J_x(x', z')\delta(y' + a) \dots$$
$$\int_{k_x} \int_{k_z} \frac{dk_x dk_z}{\sqrt{k_x^2 + k_z^2}} e^{ik_x(x-x')} e^{ik_z(z-z')} e^{-\sqrt{k_x^2+k_y^2}(y-y')} + \dots \tag{2.23}$$

In order to simplify this equation, we start by rearranging to

$$\mathbf{A}(\mathbf{r}) = \frac{\mu_0}{8\pi^2} \int_{k_x} \int_{k_z} \frac{dk_x dk_z}{\sqrt{k_x^2 + k_z^2}} e^{ik_x x} e^{ik_z z} \dots$$
$$\int_{y'} dy' e^{-\sqrt{k_x^2+k_y^2}(y-y')} \delta(y' + a) \dots$$
$$\int_{x'} \int_{z'} dx' dz' e^{-ik_x x'} e^{-ik_z z'} J_x(x', z') + \dots \tag{2.24}$$

Using the relation $\int dx \delta(x - a) f(x) = f(a)$ and equation 2.18, equation 2.24 simplifies to the following

$$\mathbf{A}(\mathbf{r}) = \frac{\mu_0}{8\pi^2} \int_{k_x} \int_{k_z} \frac{dk_x dk_z}{\sqrt{k_x^2 + k_z^2}} e^{ik_x x} e^{ik_z z} e^{-\sqrt{k_x^2+k_z^2}(y+a)} j_x(k_x, k_z) + \dots \tag{2.25}$$

This simplification can be repeated for the second term, and the resulting equation can be split into its three Cartesian components

$$A_x(\mathbf{r}) = \frac{\mu_0}{8\pi^2} \int_{k_x} \int_{k_z} \frac{dk_x dk_z}{\sqrt{k_x^2 + k_z^2}} e^{ik_x x} e^{ik_z z} e^{-\sqrt{k_x^2+k_z^2}(y+a)} j_x(k_x, k_z) \tag{2.26}$$

$$A_z(\mathbf{r}) = \frac{\mu_0}{8\pi^2} \int_{k_x} \int_{k_z} \frac{dk_x dk_z}{\sqrt{k_x^2 + k_z^2}} e^{ik_x x} e^{ik_z z} e^{-\sqrt{k_x^2+k_z^2}(y+a)} j_z(k_x, k_z) \tag{2.27}$$

and

$$A_y(\mathbf{r}) = 0 \tag{2.28}$$

Ultimately we want an expression for the magnetic field in terms of current density. Even though these gradient coils were designed for a low field magnet, the main field produced by the permanent magnet array is much stronger than the concomitant fields of the gradient coils, even at moderate pulse powers. We therefore only need to consider the z component of the gradient field in the optimization. We can easily get this expression by expanding $\mathbf{B}(\mathbf{r}) = \nabla \times \mathbf{A}(\mathbf{r})$ and simplifying

$$
\begin{aligned}
\mathbf{B}(\mathbf{r}) &= \nabla \times \mathbf{A}(\mathbf{r}) \\
&= \left(\frac{\partial A_z}{\partial y} - \frac{\partial A_y}{\partial z}\right)\hat{x} + \left(\frac{\partial A_x}{\partial z} - \frac{\partial A_z}{\partial x}\right)\hat{y} + \left(\frac{\partial A_y}{\partial x} - \frac{\partial A_x}{\partial y}\right)\hat{z}
\end{aligned} \tag{2.29}
$$

$$B_z(\mathbf{r}) = \left(\frac{\partial A_y}{\partial x} - \frac{\partial A_x}{\partial y}\right)\hat{z} = -\frac{\partial A_x}{\partial y} \tag{2.30}$$

Substituting equation 2.26 into equation 2.30 and simplifying, we arrive at the final expression for $B_z(\mathbf{r})$

$$B_z(\mathbf{r}) = -\frac{\mu_0}{8\pi^2}\int_{k_x}\int_{k_z} dk_x dk_z e^{ik_x x}e^{ik_z z}e^{-\sqrt{k_x^2+k_z^2}(y+a)}j_x(k_x, k_z) \tag{2.31}$$

In addition to an expression for the z component of the magnetic field, we also need an expression relating the stored energy to the current density. We start with the following equation

$$W = \frac{1}{2}\int_V \mathbf{A}(\mathbf{r}) \cdot \mathbf{J}(\mathbf{r})d^3\mathbf{r} \tag{2.32}$$

Expanding $\mathbf{A} \cdot \mathbf{J}$ we get

$$W = \frac{1}{2}\int_x\int_y\int_z dx dy dz\left[A_x(\mathbf{r})J_x(x,z)\delta(y+a) + A_z(\mathbf{r})J_z(x,z)\delta(y+a)\right] \tag{2.33}$$

Next, we substitute equation 2.26 into equation 2.33 and simplify with the Fourier representations of the current density and the relation $\int dx\delta(x-a)f(x) = f(a)$. Again, since this substitution results in two terms, we'll only examine the first one and simplify the second term similarly.

$$
\begin{aligned}
W &= \frac{\mu_0}{16\pi^2}\int_x\int_y\int_z dx dy dz\int_{k_x}\int_{k_z}\frac{dk_x dk_z}{\sqrt{k_x^2+k_z^2}}\dots \\
&\quad e^{ik_x x}e^{ik_z z}e^{-\sqrt{k_x^2+k_z^2}(y+a)}j_x(k_x, k_z)J_x(x,z)\delta(y+a) + \dots
\end{aligned} \tag{2.34}
$$

$$W = \frac{\mu_0}{16\pi^2} \int_{k_x} \int_{k_z} \frac{dk_x dk_z}{\sqrt{k_x^2 + k_z^2}} j_x(k_x, k_z) \dots$$
$$\int_y dy e^{-\sqrt{k_x^2 + k_z^2}(y+a)} \delta(y+a) \dots$$
$$\int_x \int_z dx dz e^{ik_x x} e^{ik_z z} J_x(x, z) + \dots \tag{2.35}$$

$$W = \frac{\mu_0}{16\pi^2} \int_{k_x} \int_{k_z} \frac{dk_x dk_z}{\sqrt{k_x^2 + k_z^2}} |j_x(k_x, k_z)|^2 + \dots \tag{2.36}$$

The second term simply has j_x replaced with j_z. Since our expression for the magnetic field (equation 2.31) only contains the x component of the current density, it would be useful to simplify equation 2.36. For that we invoke the conservation of current

$$\nabla \cdot \mathbf{J}(\mathbf{r}) = 0 \tag{2.37}$$

$$\frac{\partial}{\partial x} J_x(x, z) + \frac{\partial}{\partial z} J_z(x, z) = 0 \tag{2.38}$$

Substitute in the Fourier representation of the current density and simplify

$$\frac{\partial}{\partial x} J_x(x, z) = \frac{1}{4\pi^2} \frac{\partial}{\partial x} \int_{-\infty}^{\infty} \int_{-\infty}^{\infty} dk_x dk_z e^{ik_x x} e^{ik_z z} j_x(k_x, k_z)$$
$$= ik_x J_x(x, z) \tag{2.39}$$

Now we are ready to find a suitable expression relating j_x to j_z

$$k_x J_x(x, z) + k_z J_z(x, z) = 0 \tag{2.40}$$

Similarly, since the Fourier transform is a linear operation

$$k_x j_x(k_x, k_z) + k_z j_z(k_x, k_z) = 0 \tag{2.41}$$

$$|j_z(k_x, k_z)|^2 = \frac{k_x^2}{k_z^2} |j_x(k_x, k_z)|^2 \tag{2.42}$$

Substituting equation 2.42 into equation 2.36 and simplifying, we arrive at our final expression for the stored energy as a function of $j_x(k_x, k_z)$

$$W = \frac{\mu_0}{16\pi^2} \int_{k_x} \int_{k_z} \frac{dk_x dk_z}{\sqrt{k_x^2 + k_z^2}} \left(1 + \frac{k_x^2}{k_z^2}\right) |j_x(k_x, k_z)|^2 \tag{2.43}$$

Now that we have an expression for the stored energy (eqn. 2.43) and the z component of the magnetic field (eqn. 2.31), we can plug them into our cost function, otherwise known as an energy functional

$$E\left[j_x(k_x, k_z)\right] = W - \sum_{j=1}^{N} \lambda_j \left[B_z(\mathbf{r}_j) - \mathcal{B}_{z,j}\right] \tag{2.44}$$

Where $\mathbf{r}_j$ is a set of points where the target field will be defined, $\mathcal{B}_{z,j}$ is the value of the target field at these points, and λ_j are the Lagrange multipliers. To minimize this energy functional, we take its first variation with respect to j_x. The first variation of E is defined as

$$\delta E\left[h\right] = \frac{d}{dt} E\left[y_0 + th\right]_{t \to 0} \tag{2.45}$$

where j_x has been replaced by an expansion around y_0 with a perturbation th. We can then take its derivative and let $t \to 0$. Setting the variation δE to 0 and solving for y_0 results in an expression for j_x. W varies as the square of j_x so

$$\frac{d}{dt}(y_0 + th)^2_{t \to 0} = \frac{d}{dt}(y_0^2 + 2thy_0 + t^2h^2)_{t \to 0} = 2hy_0 \tag{2.46}$$

$$\frac{d}{dt}W = \frac{\mu_0}{16\pi^2} \int_{k_x} \int_{k_z} \frac{dk_x dk_z}{\sqrt{k_x^2 + k_z^2}} \left(1 + \frac{k_x^2}{k_z^2}\right)(2hy_0) \tag{2.47}$$

B_z varies with the first power of j_x, so

$$\frac{d}{dt}(y_0 + th)_{t \to 0} = h \tag{2.48}$$

$$\frac{d}{dt}\sum_{j=1}^{N} \lambda_j B_z(\mathbf{r}_j) = -\frac{\mu_0}{8\pi^2} \sum_{j=1}^{N} \lambda_j \int_{k_x} \int_{k_z} dk_x dk_z e^{ik_x x_j} e^{ik_z z_j} e^{-\sqrt{k_x^2 + k_z^2}(y_j + a)} h \tag{2.49}$$

finally, $\mathcal{B}_{z,j}$ does not vary with j_x, so

$$\frac{d}{dt}\sum_{j=1}^{N} \lambda_j \mathcal{B}_{z,j} = 0 \tag{2.50}$$

Solving for $y_0 = j_x$

$$j_x(k_x, k_z) = -\frac{\sqrt{k_x^2 + k_z^2}}{\left(1 + \frac{k_x^2}{k_z^2}\right)} \sum_{j=1}^{N} \lambda_j e^{ik_x x_j} e^{ik_z z_j} e^{-\sqrt{k_x^2 + k_z^2}(y_j + a)} \tag{2.51}$$

Multiplying by k_z^2/k_z^2 results in our final simplified expression for j_x

$$j_x(k_x, k_z) = -\frac{k_x^2}{\sqrt{k_x^2 + k_z^2}} \sum_{j=1}^{N} \lambda_j e^{ik_x x_j} e^{ik_z z_j} e^{-\sqrt{k_x^2 + k_z^2}(y_j + a)} \tag{2.52}$$

To determine the Lagrange multipliers λ_j, we solve the following matrix equation

$$\mathcal{B}_{z,j} = \sum_{j=1}^{N} C_{i,j} \lambda_j \tag{2.53}$$

where

$$C_{i,j} = \frac{\mu_0}{8\pi^2} \int\limits_{-\infty}^{\infty} \int\limits_{-\infty}^{\infty} dk_x dk_z \frac{k_x^2}{\sqrt{k_x^2 k_z^2}} \cdots$$

$$e^{ik_x(x_i - x_j)} e^{ik_z(z_i - z_j)} e^{\sqrt{k_x^2 + k_z^2}(y_j - y_i)} \tag{2.54}$$

and is numerically evaluated for the given points $\mathbf{r}_{i,j}$. Once the Lagrange multipliers have been evaluated, they can be inserted into equation 2.52. $j_x(k_x, k_z)$ can then be Fourier transformed to the Cartesian current density $J_x(x, z)$. The corresponding z component of the current density can be found once again through the conservation of current and equation 2.41.

2.2.2 Discretization

Once the optimized current density has been obtained, it needs to be discretized into a set of wires for it to be of any practical value. A common way of accomplishing this task is with a streamline technique [107]. Since current is conserved, meaning

$$\nabla \cdot \mathbf{J}(\mathbf{r}) = 0 \tag{2.55}$$

we know that the current density can be described by a vector potential, $\mathbf{S}(\mathbf{r})$, defined as

$$\nabla \times \mathbf{S}(\mathbf{r}) = \mathbf{J}(\mathbf{r}) \tag{2.56}$$

$$\left(\frac{\partial S_z}{\partial y} - \frac{\partial S_y}{\partial z}\right) \hat{x} + \left(\frac{\partial S_x}{\partial z} - \frac{\partial S_z}{\partial x}\right) \hat{y} + \left(\frac{\partial S_y}{\partial x} - \frac{\partial S_x}{\partial y}\right) \hat{z} = J_x \hat{x} + J_y \hat{y} + J_z \hat{z} \tag{2.57}$$

Since we are dealing with current that is confined to the x-z plane, the only relevant component of the vector potential is S_y

$$-\frac{\partial S_y}{\partial z} \hat{x} + \frac{\partial S_y}{\partial x} \hat{z} = J_x \hat{x} + J_z \hat{z} \tag{2.58}$$
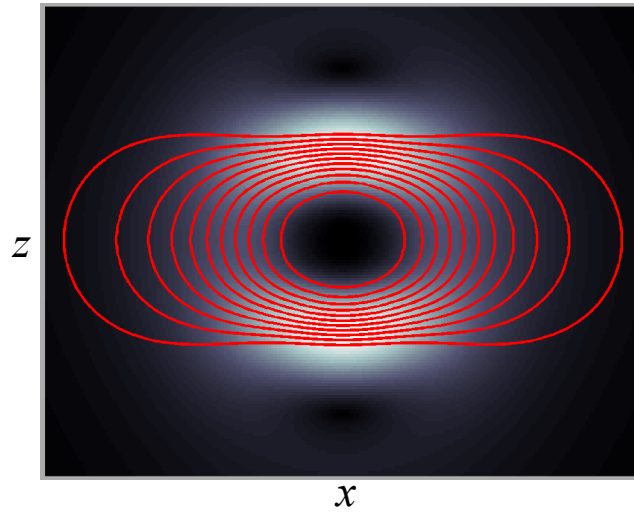
Figure 2.3: An example of the discretization of current density to a set of wires. The red lines are the contours of the stream function and represent the discretized wires. The black and white image represents the continuous current density for this particular set of coils. The light regions are ares of high current density and have a correspondingly high wire density.

The stream function can be evaluated by numerically integrating either

$$S_y(x, z) = - \int_{-\infty}^{\infty} dz' J_x(x, z') \tag{2.59}$$

or

$$S_y(x, z) = - \int_{-\infty}^{\infty} dx' J_z(x', z) \tag{2.60}$$

Plotting the contours of S_y yields a discrete set of wires. Figure 2.3 shows an example of this result. In places of high current density, there are many wires packed together, and in places of low current density, the wires are sparse. Positive and negative values of S_y correspond to current flowing in counter-clockwise and clockwise directions respectively.

2.2.3 Verification

Once the optimized continuous current density has been discretized into a set of wires, the field produced by these wires needs to be evaluated to ensure no significant distortions were introduced in the discretization process. In addition to verifying linearity, it is also important to ensure the coil has a reasonable efficiency. Coils that produce highly linear

fields often do so at the cost of gradient strength per unit current. The expected magnetic field can be approximated by evaluating the Biot-Savart law. Given an infinitesimally small section of wire $d\mathbf{l}$ and current I, the magnetic field at a point dictated by the displacement vector $\mathbf{r}$ can be calculated with the following formula

$$\mathbf{B}(\mathbf{r}) = \int \frac{\mu_0}{4\pi} \frac{I d\mathbf{l} \times \mathbf{r}}{|r|^3} \tag{2.61}$$

Analytical evaluation of this equation is only practical for a handful of idealized geometries. For an arbitrarily shaped coil, the integral can be approximated by breaking the wire down into N small but finite segments.

$$\mathbf{B}(\mathbf{r}) \approx \sum_{j=1}^{N} \frac{\mu_0}{4\pi} \frac{I \Delta\mathbf{l}_j \times \mathbf{r}}{|r|^3} \tag{2.62}$$
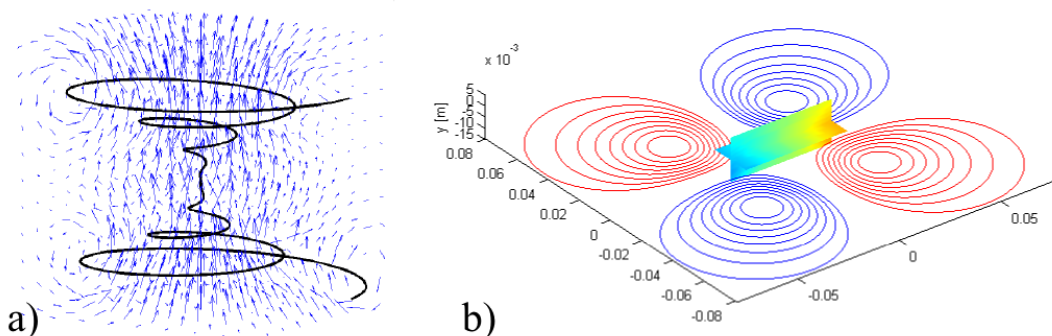
Figure 2.4: Magnetic field approximation of an arbitrarily shaped piece of wire a), and a set of multiple wires making up a gradient coil b).

2.3 Designs

Optimal designs for x and z gradient coils were produced using the method described above. The optimal coil geometry for the y gradient turns out to be a set of parallel evenly spaced wires running under the region of interest. As such, the y gradient design was produced by intuition and not computer optimized. The details of its design and performance will therefore be omitted. The specified target fields for the final designs of the x and z gradient coils are shown in table 2.1 and 2.2 respectively. The coils were designed for a target field that was 5 cm along x, and 2 cm along y and z, centered 1.5 cm above the surface of the magnet. Schematics of all three gradient coil designs are shown in figure 2.5.

The finalized designs were printed by a commercial PCB (Printed Circuit Board) manufacturer called Advanced Circuits. To make them functional, the designs had to be modified from the contour representation into a spiral pattern so that current could flow from one loop

x-gradient, $a = 1.5$ cm

j	x_j	y_j	z_j	$B_{z,j}$
1	0.025	0.000	0.000	0.010
2	0.025	1.000	0.000	0.200
3	2.000	0.000	0.000	1.125
4	0.025	0.000	1.000	0.008
5	0.200	-1.000	0.000	0.200
	cm	cm	cm	arb.

Table 2.1: Target field specification for the x-gradient coil

z-gradient, $a = 1.5$ cm

j	x_j	y_j	z_j	$B_{z,j}$
1	0.000	0.000	0.025	0.010
2	0.000	1.000	0.075	0.568
3	2.000	0.000	0.025	0.008
4	0.000	0.000	1.000	1.125
5	0.000	-1.000	0.075	0.568
	cm	cm	cm	arb.

Table 2.2: Target field specification for the z-gradient coil

to the next. For convenience and minimum field distortion, it is best to have both leads from the gradient coil to the gradient amplifier in the same location on the board. To accomplish this, a minimum of two layers is needed in order to channel the current from the center of the spiral back to the outside. The current flows between the layers through small plated holes called vias. We chose a four layer construction for our coils to maximize the gradient strength per unit current. Several long connecting wires were necessary to guide the current from one loop to the next. However, with the additional degrees of freedom provided by a four layer board, most of these wires could be paired with another wire on a different layer that had current flowing in the opposite direction. As a result, the potentially distorting fields from these wires would cancel with each other. An example of the four layer winding pattern of the x gradient is shown in figure 2.6 and a photograph of the printed result is shown in 2.7.

Each printed circuit board is 1.7 mm thick, corresponding to a total thickness of less than 6 mm for the entire gradient stack. Because the coils are stacked one upon another, the distance from each coil to the target region varies. Since they were all designed for a target field precisely 1.5 cm from their surface, significant field distortions might be expected. However, the sensitive region of the imaging scanner extended only 1 cm vertically, and the gradient coils were optimized over a region of 2 cm for additional flexibility.
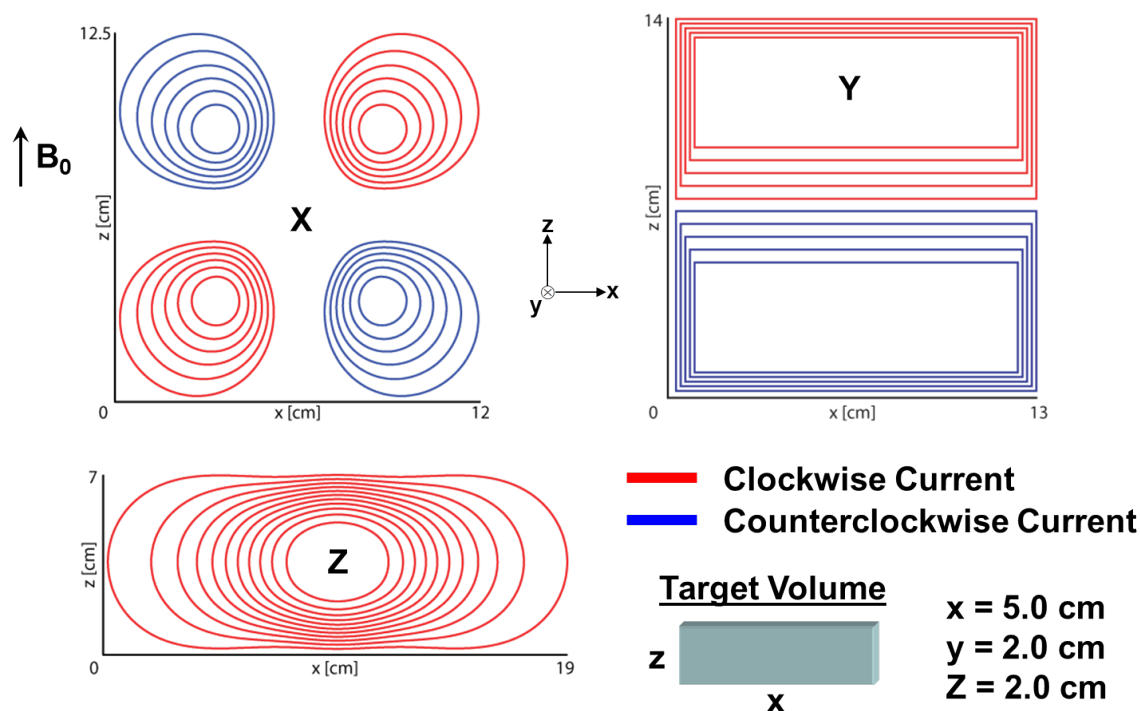
Figure 2.5: x, y, and z gradient coil designs. The x and z coils were computer optimized to produce a target field 1.5 cm above their surface. The y gradient coil was designed by intuition and trial and error.

2.4 Results

The maximum slew rates for each of the optimized gradient coils were determined by supplying a 400 μs, 1.7 A square pulse and measuring the observed current as a function of time (Figure 2.8). These pulses correspond to a peak gradient of 1.0 G/cm and 1.2 G/cm for the x and z coils respectively. The slew rate for the x coil was measured to be 37 G/cm/ms with an efficiency of 0.6 G/cm/A. Typical slew rates for a commercial high field imaging system are around 5-20 G/cm/ms. The elevated slew rate compared to the commercial system is due to the uniplanar geometry. Efficiencies for conventional high field systems are on the order of 2.5 G/cm/A and are expected to be much higher than the coils presented in this chapter due to the more efficient cylindrical geometry. The z coil had similar properties with a maximum slew rate of 20 G/cm/ms and an efficiency of 0.7 G/cm/A. To ensure there was sufficient heat dissipation, both coils were tested with the maximum gradient amplifier output of 6 A at a 1 % duty cycle. Only minimal heating was observed under these conditions.

To test the linearity of each gradient, a miniature RF coil surrounding a piece of rubber was mounted to a micro translation stage. The sample was swept through the gradient dimension along the center line of the target field. At each position, a one dimensional image was obtained. The field of view of the image was calibrated by the estimated gra-

dient strength from the Biot-Savart approximations. The observed position in the imaging dimension was plotted versus the physical position of the translation stage (Figure 2.9). The results show that along the centerline of the target field, both the x and z gradient fields are sufficiently linear. Additionally, the slope of each line is close to unity implying the Biot-Savart approximations were fairly accurate. Due to the time consuming nature of this measurement and the lack of computer automation, a full three dimensional field map was not obtained. Examining the simulated field maps, significant distortions can be seen towards the edges of the imaging volume. However, due to the limited degrees of freedom of the magnet design, the homogeneous region of the static field was significantly smaller than the target field of the gradient coil design, as can be seen in figure 2.10. As a result, no significant warping of the acquired images was observed at practical resolutions (see Chapter 3).

2.5 Conclusion

A set of 3-axis miniature uniplanar gradient coils were produced for a portable single-sided imaging sensor. The gradients satisfied the requirements of sufficient linearity and high slew rates necessary for imaging on this device. The x and z gradient were optimally designed to produce a specified target field and have minimum inductance. Due to the computer design, the gradient coils can be produced rapidly. This is an important attribute since the magnet they were designed for has an adjustable imaging volume. Many sets of gradients are needed to accommodate the various positions of the sensitive region. Alternatively, one set of gradients could be produced on a many-layer PCB, in which each layer has a different target volume. Combined with a proper voltage dividing circuit, such an apparatus would be capable of producing a uniform gradient which is continuously adjustable [48] over the various sensitive regions of the adjustable sensor as shown in Figure 2.11.
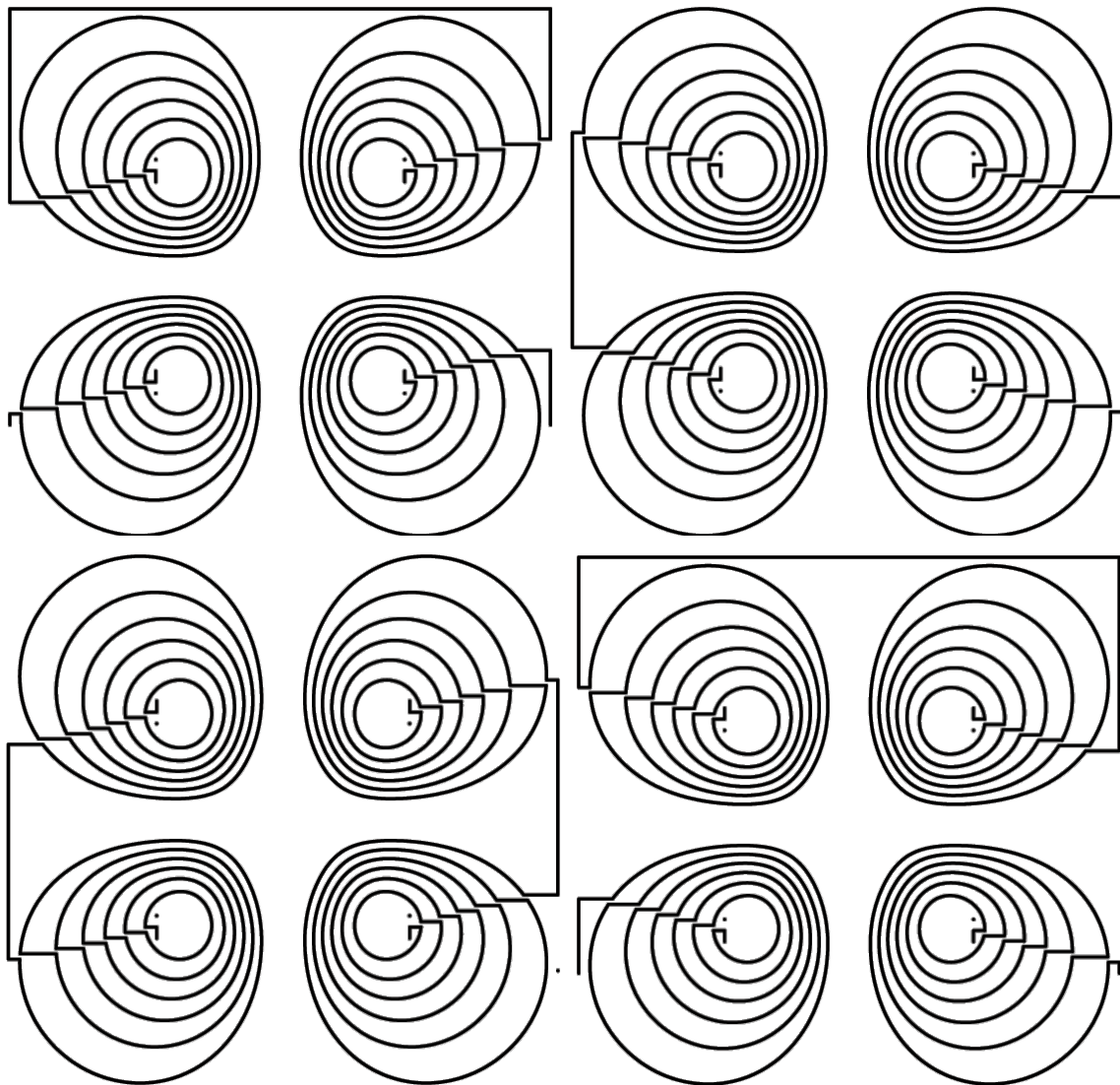
Figure 2.6: The four layer winding pattern of the x-gradient coil. The layers are in order going from the left to the right, top to bottom.
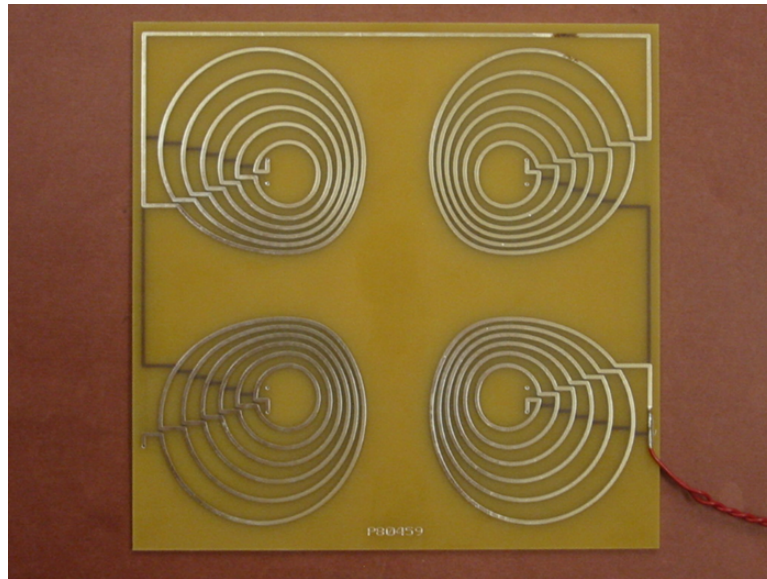
Figure 2.7: Photograph of the printed x-gradient coil.
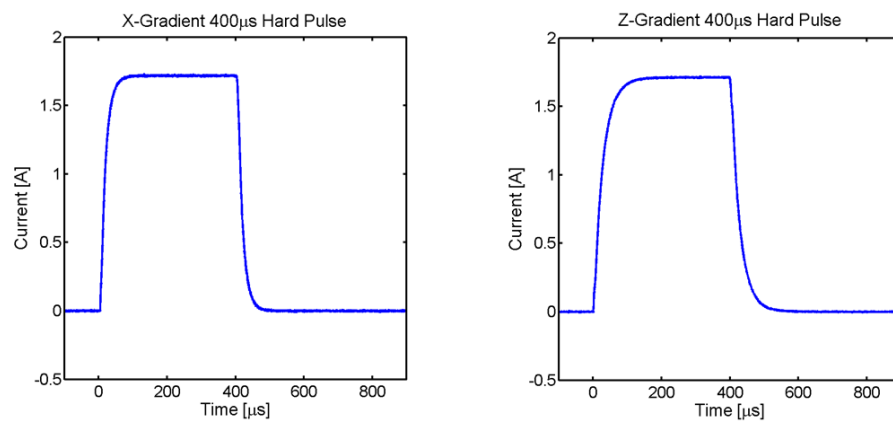
Figure 2.8: Measured response of the x and z gradients to a 400 μs square pulse.
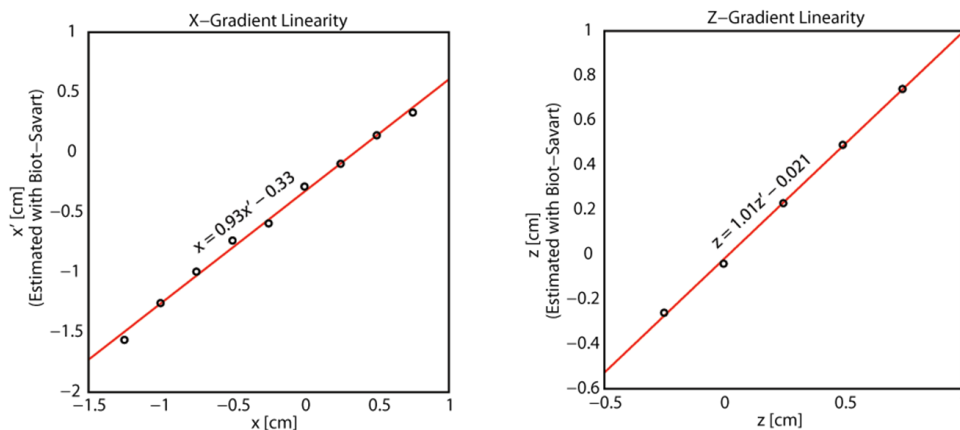
Figure 2.9: Experimental measurement of the linearity of the x and z gradient coils along the centerline of the target field. The horizontal axes correspond to the position of a small rubber sample in physical space and the vertical axes correspond to its position in image space.
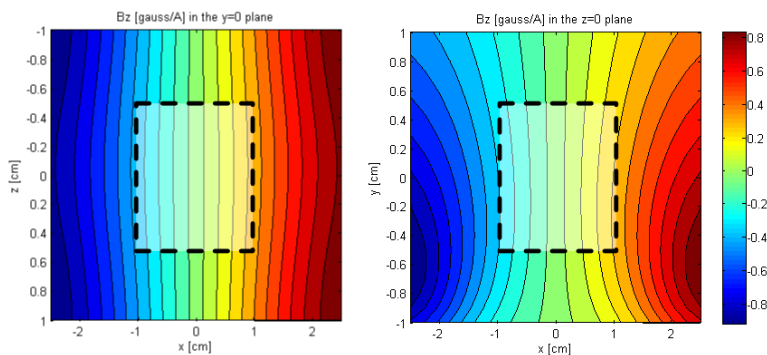
Figure 2.10: Magnetic field maps of the x-gradient along the $y = 0$ and $z = 0$ planes. The dashed rectangles represent the sensitive region of the magnet.
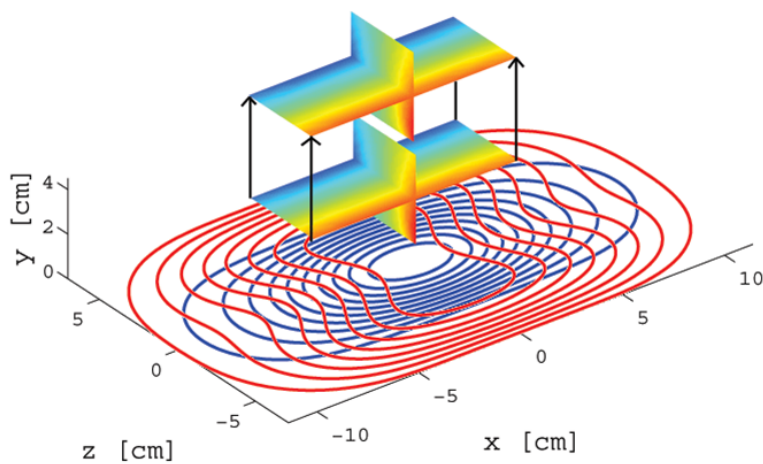
Figure 2.11: Multi-layer gradient coil design with a continuously adjustable uniform region.

Chapter 3

Volume-selective magnetic resonance imaging using an adjustable, single-sided, portable sensor

This section has been previously published in Paulsen et al. [76] and has been reproduced with permission from the authors.

Portable, single-sided nuclear magnetic resonance (NMR) sensors can operate under conditions inaccessible to conventional NMR while featuring lower cost, portability and ability to analyze arbitrary-sized objects. Such sensors can non-destructively probe inside of samples by collecting images, measure relaxation and diffusion constants, and, given careful shimming schemes, can even perform chemical analysis. The inherently strong magnetic-field gradients of single-sided sensors developed so far have prevented imaging of materials with high water content such as biological tissues over large volumes while designs with more homogeneous fields suffer from low field strength and cannot probe volumes larger than ca. 10 cm^3. We present the first design with a continuously adjustable sensitive volume, enabling the effective volume to be enlarged several fold. This allows for imaging in reasonable times of much bigger objects and opens the door to the possibility of clinical imaging with portable sensors. We demonstrate MRI in axial and sagittal planes, at varied depths of the sensitive volume and T_1-weighted contrast in a biological tissue sample.

3.1 Background

NMR and magnetic resonance imaging (MRI) can provide noninvasive chemical analysis and imaging using the endogenous contrast of materials, regardless of optical opacity. NMR can ascertain physical parameters such as diffusion, flow and structure of porous materials and biological tissue over length scales from nanometers to meters. Clinical MR imaging yields better soft-tissue contrast than either x-ray CT or ultrasound images. Clinical MR imaging is usually performed at high magnetic fields for improved signal-to-noise ratio, but

this requires bulky, expensive, immobile and often hazardous magnets. Low field NMR, on the other hand, has emerged as an attractive option for imaging in the field, in the presence of metal [69], and provides more versatile contrast for relaxation weighted images [53]. Because these smaller sensors typically operate in geometries where the static field is weak and inhomogeneous, the development of single-sided sensors has concomitantly resulted in novel methodologies and pulse sequences [73, 28, 31, 18, 59, 64, 58, 49, 68, 104, 78] to minimize image distortions and improve our ability to perform traditional chemical shift spectroscopy [13]. Therefore, objects can be non-destructively probed and one may obtain relaxation, diffusion or image data over relatively small regions and obtain chemical shift spectra with careful magnet shimming schemes [79]. In spite of these advances, only relatively small volumes can be imaged (10 cm^3 or less) or analyzed spectroscopically (20 mm^3 or less).

Mobile NMR sensors can vary in two aspects that have a fundamental impact on their performance: 1) the orientation of the field relative to the surface on the sensor and 2) the type of sensitive region the magnet produces (homogeneous field over a volume vs. thin slices in a strong gradient). In the first case, this dictates the type of RF excitation and detection coil that can be used. A field that is perpendicular to the sensor, for instance, requires an RF field parallel to the surface of the magnet, and this requires a figure-eight coil instead of a single loop which results in much lower SNR efficiencies for detection. In the second case, the sensitive region can be optimized for higher static magnetic fields at the expense of field homogeneity, which gives better sensitivity per unit volume but results in very small usable volumes and substantial signal losses to diffusion (which are a natural consequence of strong magnetic field gradients). Another option is to generate more homogeneous fields, which results in larger sensitive volumes and less diffusional losses but at the expense of field strength. These trade-offs are empirical findings that arise during magnet design processes and appear to be of a fundamental nature.

Sensors with strong gradients in the static field typically utilize the gradient select slice positions by retuning of the resonant RF circuit. Diffusion attenuation for large gradient devices is a serious impediment to SNR and does not normally allow measurements of samples with high water content[1]. The NMR MOUSE [28] features a 5 kG field in a ∼0.1 cm^3 volume near its surface whereas the NMR MOLE [58] design has a 767 G field over a 6.2 cm^3 volume located 5 cm above its surface. Because of the lower diffusion attenuation in homogeneous field sensors, they are better suited for studying liquid samples such as aqueous solutions and biological tissue [58]. The current homogeneous field sensors are fixed configurations and can only sample a single useful region in space, which is typically less than 10 cm^3 in size.

We present the novel concept of an adjustable sensitive volume, with the use of a continuously adjustable array of permanent magnets which can be mechanically tuned in a way similar to how guitar strings are tuned. Thus, we are able to perform MRI of liquid

---

[1]The free induction signal decays due to diffusion according to $\exp\left[-(1/3)\gamma^2 G^2 D t^3\right]$ from a uniform gradient [16] where G is the gradient, and D is self-diffusion coefficient. For a 1 kG/cm gradient, the signal from water decays by half in 2 ms whereas in a 10 G/cm gradient, this decay timescale is 50 ms.

samples over volumes that are much larger than a conventional magnet.[2] Our magnetic-field orientation and RF field configuration are optimized for low power requirements and high sensitivity.[3] The design follows a recently-developed inverse magnet design method [76] which is adapted to cylindrical geometries and is therefore straightforward to assemble. The cylindrical geometry naturally leads to the adjustability feature.

3.2 Methods

3.2.1 Magnet design, assembly, and characterization

The sensor was designed by an inverse technique we developed based on a least-squares fit of optimal dipole magnitudes to produce a desired target field [76]. For arrays of parallel permanent magnet rods, it yields optimal rod radii and orientations of the magnetization given a desired target field and rod locations. The rod positions were determined by a global search, where our inverse technique determines the optimal dipole strengths and orientations for each of a representative set of possible arrangements and the search picks the best array. To determine how the rod orientations should vary to move the sensor's sensitive volumes, the method uses constraints to optimize rod orientations given fixed magnet rod sizes. See ref [76] for details.

The magnet's implementation for our sensor consists of four pairs of cylindrical $Nb_2Fe_{14}B$ magnet rods (Fig. 3.1.i,v) magnetized perpendicular to their axes with μ_o M = 1.35 T, and held in place mechanically by an aluminum and bronze frame (Fig. 3.1) containing a few small stainless steel components for reinforcement. Each magnet rod pair consists of two collinear cylindrical magnet rods separated by small gap which allows for improved magnetic field homogeneity along the direction of the rod axes [5]. The magnet rods at the far ends are flattened in order to be gripped by a brace which connects the rod to its own axle. This axle is fixed to the frame to allow free rotation, and attached to it is a gear and wormdrive assembly to control the rod's orientation by turning a key, and a brake to fix its orientation once in position.

The frame consists of four boxes held together by a system of nuts and threaded rods and each box contains two of the magnet rods (Fig. 3.1). This division exists to provide a straightforward procedure to bring the magnet rods into position (Fig. 3.1). The rod orientations for Volume 1 corresponds to the original optimization in [76], whereas Volume 2 corresponds to a sensitive volume located an additional 1 cm away from the surface. All final rod orientations may need to be adjusted from their calculated values since the rod magnetizations will vary on the order of several percent from their ideal values. A coarse field map of the target volume is obtained and a fine tuning is performed as needed. Detailed field maps following this fine adjustment are shown in Fig. 3.2, where we measured the proton

---

[2] While a fixed field sensor could be scaled in order to sample larger volumes, it would have to be designed to produce a distant sensitive volume, but the magnetic field strength of a distant volume is inherently weak.

[3] The adjustability feature also provides a way to compensate for the variability across different permanent magnet blocks and imperfections within each block which inevitably arise during the manufacturing process.

resonance frequency of a 2 mm rubber sample at each position of an 11×11 grid spanning 2 cm × 2 cm in the yz-plane for each of 5 slices spaced 1 cm apart along the x-axis, three of which are shown in Fig. 3.2. This fine tuning only needs to be done once after the magnet is assembled for the first time.

3.2.2   Gradients

Single-sided gradient coils for spatial encoding along each axis were designed using a least-squares target field method which minimizes the stored energy allowing for higher slew rates. Each coil was printed as four copies in a spiral pattern on a single four-layered printed circuit board to maximize the gradient field strength per unit current. The coils produce a gradient field of 0.7, 1.1, and 0.7 $G\,cm^{-1}A^{-1}$ for the 'x', 'y', and 'z' gradient coils, respectively, with slew rates of 37, 64, and 49 $G\,cm^{-1}ms^{-1}$. The gradients were placed above the sample opposite the RF coil for Volume 1 whereas the gradients were right on top of the magnet with the RF coil raised above by 1 cm for Volume 2. Details of the gradient optimization and design can be found in Chapter 2.

3.2.3   Imaging

All images were collected using an Apollo LF Spectrometer (Tecmag, Houston, TX), an AE Techron LVC 2016 Linear amplifier (AE Techron, Elkhart, IN) and a CPC MRI Plus RF amplifier (CPC, Hauppauge, NY). The imaging pulse sequence (Fig. 3.3) is a basic pure phase encoding imaging sequence with a CPMG acquisition train. The sequence was implemented with a 8 μs nominal $\frac{\pi}{2}$ pulse length, 100 to 200, 810 μs acquisition echoes, a 700 μs gradient pulse length, and 200 ms and 75 ms recycle delays for the Gd-DPTA doped water and pork belly samples respectively. Sensitivity maps were collected with the same conditions as the images to be corrected using uniform phantoms that spanned most of the field of view. Image intensities are adjusted according to sensitivity maps by dividing the object image intensities by those of the sensitivity map with a soft threshold applied to regions below a certain sensitivity. The water phantom and pork belly samples uniformly span 1 cm and 0.5 cm, respectively, across the non-imaged axis.

A pure 2D phase encoding is used for spatial localization [18]. This has the advantage of reducing the effects of magnetic field inhomogeneities to an overall scaling factor across the image and leaving the image free of inhomogeneity artifacts. At low magnetic fields, multiple acquisitions are generally required to provide enough signal averaging, so pure phase encoding does not cost in additional scan time. The sequence begins with an initial RF excitation pulse followed by a gradient pulse for phase encoding (Fig. 3.3.a) and a CPMG train for signal averaging. For the CPMG train, we change the phase of the refocusing pulse by $\frac{\pi}{2}$ between each acquisition (Fig. 3.3c), taking advantage of the fact the sequence will effectively keep only the component of each spin initially along the axis of the refocusing pulse (Fig. 3.3d) as explained elsewhere [1, 45].

3.3 Results

The sensor consists of an array of four cylindrical permanent magnet rods with a prescribed orientation of the magnetization for each rod, and this set of orientations is dependent on the location and size of the desired sensitive volume. Flat RF and gradient coils placed near the surface of the magnet are used for imaging. The details of the sensor design, assembly and characterization are provided in the methods section. A volume size and position is chosen for the experiment and a computer program returns the magnet rod orientations which are then adjusted. To illustrate adjustability and imaging functionalities of the sensor, we picked two non-overlapping sensitive volumes centered at a distance 1.0 cm and 1.8 cm from the magnet's surface (or equivalently, 3.0 cm and 3.8 cm from the center of the magnet rods). We note that the magnet array can also produce sensitive volumes over a continuous range of distances [76]. Each of these volumes was characterized by acquiring a magnetic field map as shown in Fig. 3.2, which shows that the volumes are sufficiently homogeneous for RF excitation using a typical resonant circuit. The first sensitive volume (Volume 1) produces a (686 ± 6) G field over a 8.9 cm^3 region (Fig. 3.2a), and the more distant sensitive volume (Volume 2) produces a (518 ± 6) G field over 8.1 cm^3 (Fig. 3.2b). As the sensitive volume is pushed away from the sensor's surface, it shrinks along the direction of the magnet rod axes as homogeneity along this axis relies on how close these rods approximate those of infinite length; this approximation breaks down at large distances [76].

Magnetic resonance images along axial and sagittal planes for both sensitive volumes are shown in Fig. 3.4. The first set of 2D images (Fig. 3.4(a-d) are of phantoms consisting of Gd-DPTA doped water in polycarbonate frames and demonstrate the sensor's ability to image in orthogonal planes and the ability to obtain images of high water content samples, which is not possible with sensors that feature a large gradient. The doping was used to increase the water relaxation rates to be closer to tissues. All of these MRI images accurately depict the shape of the phantoms at reasonable in-plane spatial resolutions, as seen by the comparison with photographs of the phantoms shown in Fig. 3.4. Figure 3.4(a) and Figs. 3.4(c,d) show MR images obtained with extended acquisition times (34 min and 1 hr 37min, respectively). Figure 3.4(b) illustrates the result with a much shorter (10 min) acquisition time, which still yields good performance.

To demonstrate MR imaging of biological tissues, a T_1-weighted image of a pork belly sample is shown Fig. 3.4(e). Here, the fat and muscle tissues are clearly differentiated as red and green regions respectively within the chosen colormap. In this case, the imaging sequence uses a shortened repetition delay to produce T_1-weighted contrast between muscle and fat.

3.4 Conclusions

We have developed an MRI sensor with adjustable sensitive volume which can be moved away from the sensor's surface thereby enlarging the effective volume which can be probed with a single-sided, portable sensor. This allows for significantly larger effective imaging

volumes than otherwise possible with a fixed sensor of the same size. At each given depth, it can produce nearly a 10 cm^3 homogeneous volume with residual gradients small enough that biological tissues can be imaged without significant diffusion losses. While the imaging times and spatial resolution (5 min and 2 mm for Fig. 3.4(e) are quite reasonable in its current configuration, further improvements and acceleration are still possible with the use of subsampling techniques [55] and multiple coil techniques [82, 32]. These latter techniques are particularly advantageous with a pure phase encoding MR imaging scheme as used here. While much larger gains in SNR are also possible with the use of prepolarization [61], hyperpolarization [74, 63], microcoil [89], and remote-detection [72] techniques, the sensor can already achieve decent imaging performance in its current incarnation.
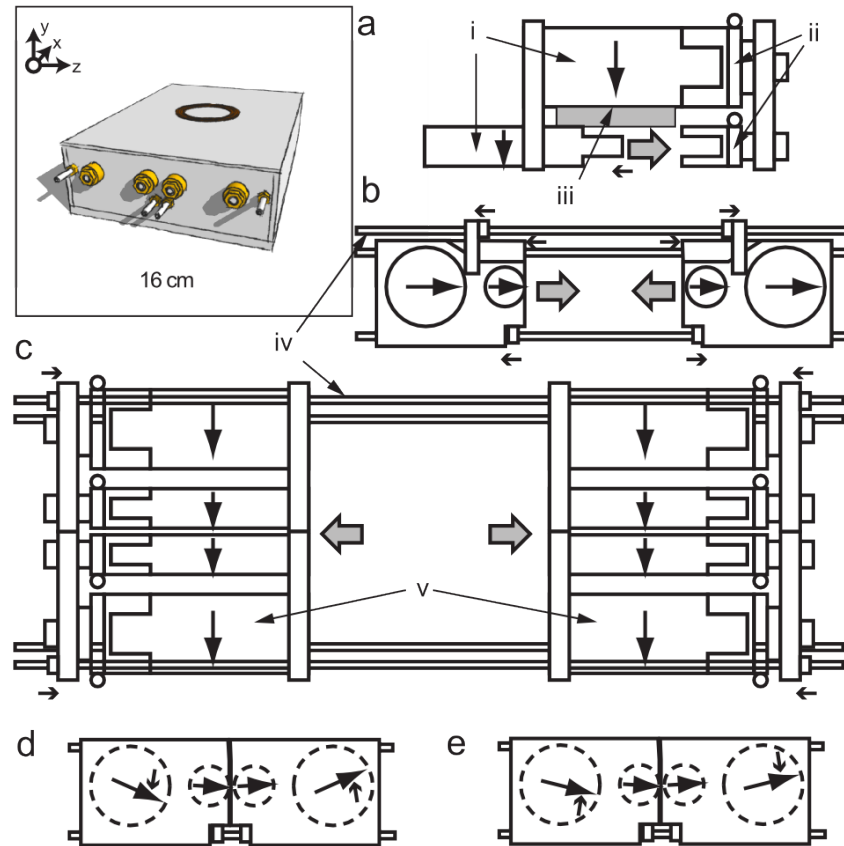
Figure 3.1: The magnet and a schematic of its assembly. **a)** Individual magnet rods (i) are placed into the frame's four sections by hand. **b)** These sections are brought together into halves, where a system of threaded rods and nuts (iv) opposes the attractive forces between the sections and allows them to come together gradually in the correct orientation. **c)** A system of threaded rods and nuts (iv) brings together the two halves holding them in place against the repulsion between the two halves. **d)** Rods are rotated to their calculated optimal values (24.1° and 3.5° for the outer and inner rods, respectively). These orientations are then adjusted several times according to a coarse field map of the target volume. **e)** To push the sensitive volume further out, the outer rods are turned 7.5° into the plane containing the rods. **i)** The $Nb_2Fe_{14}B$ cylindrical magnet rods are all 9 cm long and flatted for 1 cm on one of the ends to allow the frame to hold them in the desired orientations. The small and large rods have 2 and 4 cm diameters, respectively. **ii)** At the flattened end of each magnet rod, a gear and worm drive assembly controls the rod's orientation. **iii)** A temporary 1 cm thick board keeps the appropriate distance between the magnet rods while they are placed into each of the frame's sections. **iv)** A system of threaded rods and nuts bring the magnet's sections together in a controlled manner. **v)** In the final configuration each rod is paired with another to create a rod that is effectively 18 cm long.
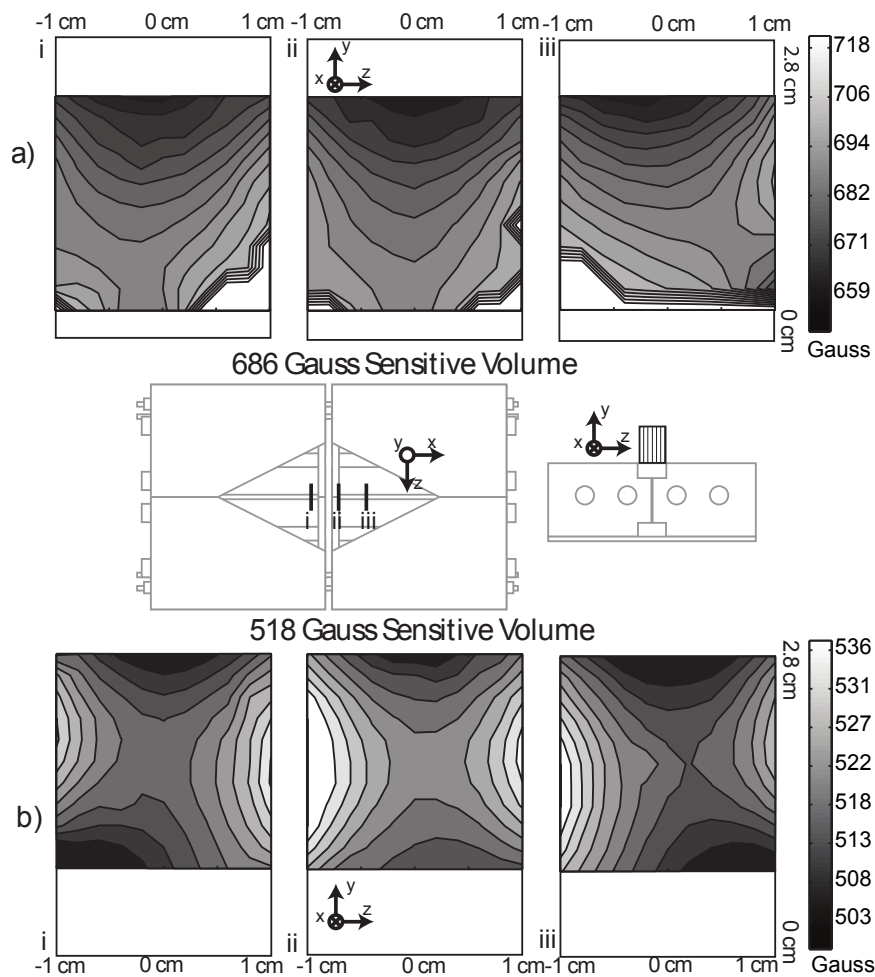
Figure 3.2: Contour field maps of **a)** sensitive volume 1 (686 Gauss) and **b)** 2 (518 Gauss) sensitive volumes for three slices above the magnet. The homogeneous region of each covers a different region of space. As the sensitive volume is pushed further out, its shape changes into a saddle point. The field strengths for each slice are based on the proton resonance frequency of a 2 mm in diameter, 2 mm long piece of rubber positioned over an 11×11 grid spanning 2×2 cm. The center shows a drawing of the magnet surface to identify positions i, ii, and iii.
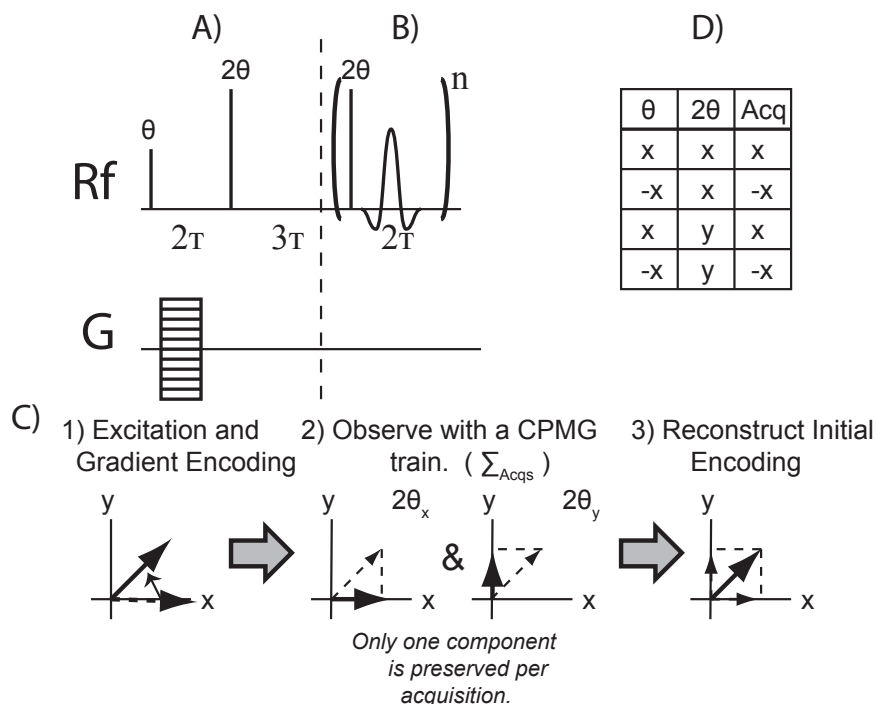
Figure 3.3: The MRI pulse sequence for imaging in inhomogeneous fields consisting of a 2D pure phase encoding step followed by a CPMG train for signal-averaging: **a)** an initial RF pulse, gradient pulse and echo excite and spatially encode the spins and **b)** a final echo train acquires the signal. **c)** The overall effect of the echo train in an inhomogeneous field is to retain only the component along the axis of the refocusing pulse. **d)** Thus the relative phases of the pulses and acquisition are cycled between runs so to obtain both components of the encoded phase. This phase cycle also eliminates any residual ringing from the refocusing pulse.
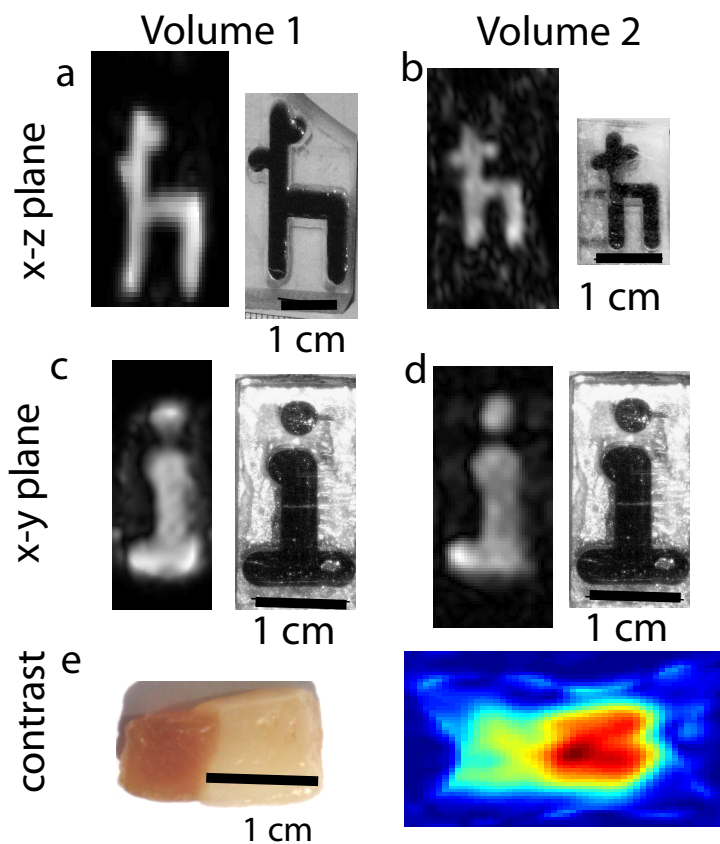
Figure 3.4: MRI images of the symbols "$\hbar$" **(a,b)** and "i" **(c,d)** carved into a polycarbonate block and filled with 2 mM Gd-DPTA solutions. Photographs of the phantoms filled with dyed water are shown next to the MR images. All samples are 10 mm thick. Within the sensitive region the phantom's shapes are accurately reproduced. Images a,c and b,d are acquired in Volumes 1 and 2, respectively. The true image resolution (field of view divided by acquisition matrix) was: a) 2 mm b) 2 mm c) 1 mm d) 1 mm. **(e)** An x-z plane MRI image of a piece of pork belly at 2 mm resolution showing T_1-weighted contrast between fat and muscle. All images are Gaussian filtered and adjusted according to a sensitivity map. The acquisition matrix was: a) 17×17, b) 25×25, c,d) 13×29 e) 17×17 and images were reconstructed by zero-filling to a) 51×51, b) 75×75, c,d) 39×87, e) 51×51.

Chapter 4

^{129}Xe signal enhancement by gas extraction and compression

4.1   Xenon magnetic resonance

^{129}Xe, a spin 1/2 nucleus, has been studied with magnetic resonance since the early days of NMR. Extreme pressures of tens to hundreds of atmospheres [81, 46], or liquid or solid xenon [111], were required in order to extract signal from the low density gas. As such, practical applications of xenon were limited at first. In the late 1970s and early 1980s, it was discovered that spin exchange optical pumping (SEOP) of xenon [35, 38] could enhance the magnetization of xenon by 4 to 6 orders of magnitude. In SEOP, angular momentum from circularly polarized laser light is transferred to the valence electron of rubidium. Through collisions and hyper-fine coupling, it is then transfered to the nucleus of xenon. As a result, the polarization of xenon can be enhanced beyond the thermal equilibrium dictated by the Boltzmann distribution and into a hyperpolarized state. The gain in magnetization compensates for the lack of density and allows for detection of xenon at partial pressures of a fraction of an atmosphere with suitable signal to noise ratios. Since the development of spin exchange optical pumping, the unique magnetic resonance properties of xenon have been exploited through a wide variety of practical applications.

The large magnetization of a low pressure gas has been widely utilized to study the void spaces of lungs where there is little to no natural signal in an MRI. By filling the lungs with a mixture of hyperpolarized xenon and oxygen, relatively high resolution images of both lung structure [21], and function [86, 88] can be obtained. Additionally, it has been used to study flow properties of gases around objects [37] and in porous media [97, 39]. Another interesting property of xenon that makes it attractive outside of gas phase applications is xenon's extraordinary chemical shift of around 0-7500 ppm [33]. The large electron cloud surrounding the xenon nucleus is highly polarizable and capable of shifting its resonance frequency over several hundred ppm by van der Waals interactions alone. Furthermore, since it is relatively soluble and inert under reasonable conditions, xenon is an ideal sensor of its chemical environment. It has been used to probe the surfaces of zeolites [84], the

chemical properties of lung and brain tissue [86, 101, 114], and for molecular detection when combined with a targeted biosensor [99].

The major challenge when using xenon as a chemical sensor is the further reduction in concentration when dissolved in a solution or adsorbed on a surface. Complicating the process further is the fact that the xenon must be transferred carefully and swiftly to the sample of interest in order to avoid a loss of magnetization due to relaxation. To compensate for these factors, sensitive chemical detection with xenon is often done with highly efficient polarization and gas mixtures of essentially pure xenon. Efficient polarization requires low pressures [6], so accumulating a useful amount of highly polarized xenon can take a substantial amount of time. As a result, there is motivation to develop polarizers with large pumping cells and extremely high power laser systems capable of rapidly producing xenon polarized to upwards of 60% [87]. Such polarizers are very effective, but are large and expensive, limiting the accessibility to xenon's incredible chemical shift.

4.2 Hyper-SAGE
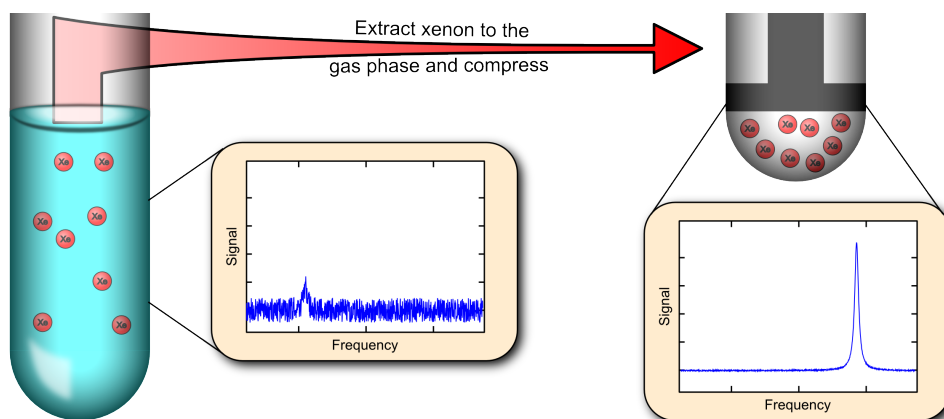
Figure 4.1: Schematic demonstrating the signal enhancement by extracting gas from solution and compressing it prior to detection.

Instead of focusing on highly efficient spin exchange optical pumping, we developed a potential low cost alternative to studying solution state xenon by extracting it from solution and detecting it in the gas phase. The primary advantage of detecting xenon in the gas phase is its compressibility (Fig. 4.1). By compressing the gas prior to detection, the spin density can be enhanced dramatically and the signal can be recovered from a xenon sample which was polarized with a cheaper less efficient polarizer design, or even thermally polarized. In addition to its compressibility, gas phase xenon has increased relaxation times relative to

xenon in solution corresponding to narrower linewidths for detection, or efficient averaging over an echo train. Finally, the high solubility of xenon relative to other gases provides an additional enhancement when working with continuous flow polarizer designs. Gas mixtures used for optical pumping are typically only 1-5% Xe, 5-10% N_2, and a balance of He. When operating under continuous flow (as opposed to freezing out and purifying the xenon in batch mode), the gas mixture being dissolved in solution is the same composition as the mixture used for optical pumping. Due to the enhanced relative solubility of xenon compared to N_2 and He [90], the composition of the extracted gas will contain a higher percentage of xenon if the input gas pressure is higher than the extraction gas pressure (see appendix B for a detailed analysis of this phenomenon).

Although the xenon signal can be enhanced through extraction and compression, the gas phase signal is simply a peak at 0 ppm. In order to extract information about the solution of interest from the gas phase xenon, we need a way to correlate the two environments. Two such techniques capable of accomplishing this task are remote detection and chemical exchange saturation transfer.

4.3   Remote detection

In a typical magnetic resonance experiment, spectroscopic and/or spatial information is encoded and detected by the same RF coil in the same environment. In a flowing system, these steps can be separated and optimized independently to maximize the efficiency of each, a technique called remote detection. Since detection in a magnetic resonance experiment consists of a measurement of a frequency, or a distribution of frequencies, the detection can be discretized by measuring a phase which has evolved over a given interval. By incrementing this interval between the individual acquisitions, the signal of interest is reconstructed. Furthermore, the phase can be stored by projecting the 'x' and 'y' components of the magnetization onto the longitudinal axis for detection at a later time. In a flowing system, a different time corresponds to a different physical location which can be optimized for sensitive detection. A classic practical application of this technique involves magnetic resonance of microfluidic chips [43, 65, 40, 41]. The optimal encoding coil for a microfluidic chip is one which contains the entire chip and is capable of exciting all spins instantly and uniformly. This type of coil is very inefficient for detection, though, because of the limited filling factor of the sample. A coil that can contain the entire chip is on the order of milliliters in volume and the sample volume contained in the microfluidic channels is on the order of microliters to nanoliters. By detecting the sample after it flows off of the chip and into a capillary, the filling factor is maximized and the signal is amplified. Similarly, with a system of flowing xenon solution, phase information from xenon in solution can be encoded and stored in the xenon magnetization. The gas can then be extracted and compressed to increase the spin density. Through a series of measurements of the residual longitudinal magnetization, the signal from the xenon solution can be reconstructed.

The "point-by-point" nature of a remote detection experiment can correspond to long acquisition times, resulting in a small signal amplification per $\sqrt{t}$ when compared to the

directly detected signal averaged over the same acquisition time. As a result, it turns out not to be a very effective acquisition scheme for signal amplification by gas extraction experiments. It is however useful for characterizing the amplification of the process since a directly acquired spectrum can be quantitatively compared to a remotely acquired spectrum of the same sample. Remote detection of extracted xenon is the focus of the following two chapters. Chapter 5 describes a proof of concept experiment in which hyperpolarized xenon was extracted from solution but not compressed. A spectrum and an image were reconstructed remotely demonstrating the ability to detect a sample at a later time, location, and physical phase. In chapter 6, an apparatus capable of performing remote detection with gas extraction and compression is described and its performance is analyzed.

4.4   Chemical exchange saturation transfer

Chemical exchange saturation transfer (CEST) techniques have been demonstrated with functionalized xenon sensors for the purpose of molecular detection [94]. A CEST experiment consists of two steps. First, the sample is prepared by continuously saturating the sample at the frequency of the xenon inside the molecular sensor cage. The nuclei of xenon atoms associated with the construct are depolarized, and through exchange with the bulk xenon in the solvent, the bulk magnetization of the sample is depleted. After the preparation phase, a broadband RF pulse is applied to excite the xenon sample and the magnitude of the remaining signal is recorded. By comparing the magnitude of the signal to an acquisition in which the preparation involved a saturation pulse at a frequency off resonance from the sensor, the presence of the sensor can be determined. The two steps required for a CEST acquisition are naturally distributed between the encoding and detection coils in a gas extraction experiment. Furthermore, since only two acquisitions are required for a complete experiment, CEST is an ideal acquisition scheme for the signal amplification by gas extraction technique. In chapter 7, a set of experiments are described which utilize this technique. Additionally, the possibility of using thermally polarized xenon with gas extraction and compression is explored in order to maximize the accessibility to xenon's chemical shift.

Chapter 5

Hyperpolarized xenon NMR and MRI signal amplification by gas extraction

This section has been previously published in Zhou et al. [112] and has been reproduced with permission from the authors.

A novel method is reported for enhancing the sensitivity of nuclear magnetic resonance (NMR) of dissolved xenon by detecting the signal after extraction to the gas phase. We demonstrate hyperpolarized xenon signal amplification by gas extraction in both NMR spectra and magnetic resonance images (MRI) with time-of-flight (TOF) information. Hyper-SAGE takes advantage of a change in physical phase in order to increase the density of polarized gas in the detection coil. At equilibrium, the concentration of gas phase xenon is roughly ten times higher than that of the dissolved phase gas. After extraction the xenon density can be further increased by several orders of magnitude by compression and/or liquefaction. Additionally, being a remote detection technique, the Hyper-SAGE effect is further enhanced in situations where the sample of interest would occupy only a small proportion of the traditional NMR receiver. Coupled with targeted xenon biosensors, Hyper-SAGE offers a new path to highly sensitive molecular imaging of specific cell markers by detection of exhaled xenon gas.

5.1 Background

MRI is a powerful technology, capable of routine and non-invasive imaging of the internal structures and functions of a multitude of subjects ranging from biological samples in medical imaging to porous media in materials science [52, 51, 12, 16]. Conventional MRI focuses mainly on the nuclear spin of the proton due to the fact that it is ubiquitous in most parts of the human body. However, the lung has a low proton spin density attributable to the large volume of air dispersed throughout the tissue. The low sensitivity of traditional magnetic resonance has motivated the development of techniques using hyperpolarized noble gases for NMR and MRI [84, 3]. Hyperpolarized noble gases can provide signal enhancements of 10,000

to 100,000 times that of thermally polarized gases [108, 115] making it possible to obtain MR images of the lung airspace with unprecedented spatial resolution and sensitivity [88, 70]. Xenon also has the unique characteristic of being soluble in many fluids and biological tissues, such as water, blood, lung tissue, and white and grey matter [20, 74, 33]. Being a trace element in the atmosphere, xenon has no natural background signal in the human body [20, 74, 33]. Therefore, dissolved phase xenon MRI and molecular imaging could provide rich information related to biological and physiological changes beyond void space lung imaging. Efforts have demonstrated the value of dissolved xenon MRI in the study of lung gas exchange [102, 86, 26], and brain perfusion [101, 27, 47, 114].

Xenon based molecular imaging has been demonstrated using cryptophane containing biosensors [42]. Sensitivity enhancement using a chemical amplification technique, hyperpolarized xenon chemical exchange saturation transfer (Hyper-CEST) [94], allows imaging at low concentrations; however for in vivo applications the small filling factor of a region of interest in the body relative to the NMR coil is a significant factor limiting sensitivity. In such cases remote detection methods [72, 43] can provide dramatic improvements in sensitivity. In remote detection, the normal NMR coil which contains the full region of interest, is used to encode spectroscopic and spatial information, then stores it as longitudinal magnetization. These encoded spins then flow into a second coil with an optimized filling factor for detection.

Remote detection can overcome the filling factor issue of dissolved xenon MRI, although a low concentration of xenon in solution can be another significant impediment to highly sensitive detection [71]. It has been shown that the solvated xenon signal can be amplified by xenon polarization transfer contrast (XTC) [86], in which the dissolved phase xenon is selectively saturated, and through exchange, the gas phase signal is attenuated. This method is able to indirectly image dissolved phase xenon, but is limited to tissue in direct exchange with the air in the lungs. The gas exchange process could be similarly exploited for direct signal amplification of dissolved xenon with the remote detection technique. Xenon gas can be extracted from the dissolved solutions, and concentrated in the gas phase for detection. Furthermore, with the long longitudinal relaxation time of gas phase xenon [20, 74, 33], extracted xenon gas from solution can be compressed or liquefied while preserving the encoded information. Since the xenon density in the liquid state is approximately four orders of magnitude higher than in aqueous solutions [20, 74, 33], this in principle could result in up to a ten thousand times enhancement of spin density, thus allowing substantial signal amplification.

In this report, we demonstrate the Hyper-SAGE method with enhanced NMR spectra and time-of-flight images using recently commercialized membrane technology for high efficiency xenon dissolution [8]. The Hyper-SAGE technique relies on physical amplification by exploiting a phase change and is completely distinct from chemical amplification. In combination with additional amplification techniques such as Hyper-CEST, this method promises to dramatically decrease the detection threshold of MRI and has the potential to benefit molecular imaging applications and medical diagnostics. Moreover, since the polarization of hyperpolarized xenon is not dependent on the magnetic field strength, this technique could

also be applied for use with low field portable MRI devices [7, 13, 76].

5.2 Materials and methods

5.2.1 Hyperpolarized xenon

A homebuilt xenon polarizer produces hyperpolarized ^{129}Xe by spin-exchange optical pumping (SEOP) [108]. The apparatus is similar to that in reference [115] except that the current setup allows for continuous gas flow. A gas mixture of 2% natural abundance Xe, 2% N_2, and 96% He flows through an optical pumping cell filled with Rb vapor at 140 C°. Three laser diode arrays optically pump the Rb at 794.7 nm with ca. 110 W of total laser power. Typical polarization levels of 8-10% are achieved at a flow rate of 0.5 SLPM.

5.2.2 Flow setup

Hyperpolarized ^{129}Xe is dissolved and extracted in three independent flow paths as depicted in Figure 5.1. The xenon gas mixture flows from the polarizer at 0.5 SLPM and a pressure of 50 psi (340 kPa), where it encounters the first of two membrane modules (Membrana model G543, 16 mL liquid volume, 25 mL gas volume). This module allows the gas to come into contact with recirculating distilled water pressurized to 80 psi (550 kPa) and flowing at a rate of 2 mL/s. The large surface area of the membrane module enables rapid dissolution of hyperpolarized xenon into the water. The water then flows into a cylindrical phantom (10.8 mL) inside a 38 mm saddle-shaped encoding coil where the NMR information is encoded into the longitudinal magnetization at 9.4 T. The dissolved xenon continues flowing to a second membrane module (Membrana model G591, ca. 1 mL liquid volume, 2.7 mL gas volume) where it is extracted from the liquid under a vacuum of 4 psi (28 kPa). The extracted gas is then detected with a 3.2 mm ID, 1 cm long solenoid detection coil with a detection volume of 0.02 mL.

5.2.3 Pulse sequences

The pulse sequences for the remotely detected spectrum, and the remotely detected time of flight images are depicted in Figure 5.2 (a) and (b) respectively. Both sequences follow the basic remote detection format where the magnetization in the encoding volume is excited, allowed to evolve, then stored to the longitudinal axis. The encoded spins then flow to the detection coil where the z-magnetization is read out with a series of excitation pulses. Since each storage pulse only stores one component of the magnetization, a minimum of two phase cycles is needed to collect both the real and imaginary components of the data. For the remotely detected spectrum, the spins are allowed to evolve under chemical shift for a time τ, which is then incremented to reconstruct the free induction decay (FID) point-by-point. To acquire the TOF images, the spins evolve under two phase encode gradients applied in the z and x directions to encode the spatial information. A 180° pulse is then applied at a
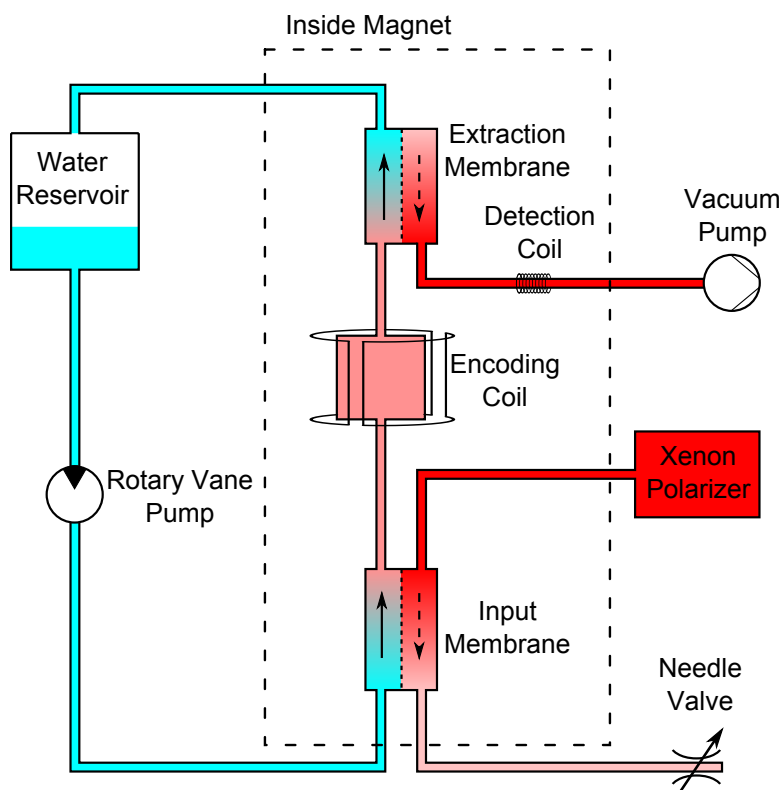
Figure 5.1: Schematic of the experimental setup. Blue and red shading represent the water and gas flow paths respectively. The intensity of the red coloring indicates the concentration of hyperpolarized xenon. Distilled water initially flows to the input membrane contactor where it comes into contact with hyperpolarized xenon produced by a homebuilt polarizer. The aqueous xenon solution then flows to an encoding coil where either spectral or spatial information is encoded into the sample. Finally, the solution travels to the extraction membrane contactor where the encoded hyperpolarized xenon is extracted into the gas phase and detected in the detection coil.

time τ to refocus the effects of any static field inhomogeneities. Finally, at a time 2τ, the encoded information is stored along the z-axis and the spins flow to the detection coil to be decoded. A four step phase cycle involving both the storage and detection pulses was used to acquire the remote spectrum in order to remove the baseline offset of the FID produced by unencoded spins in the detection coil. The time-of-flight images were collected with only a two step phase cycle of the storage pulse in order to save on acquisition time.

5.2.4 Data reconstruction

Spectrum - Due to the four step phase cycle used in acquiring the remote spectrum, only encoded spins contribute to the signal in the detection coil. Optimal signal to noise can be obtained by acquiring the entire encoded volume in one acquisition, however, due to the large volume of extracted gas compared to the detection volume, the encoded spins

were detected over 60 acquisitions. Each FID collected from the individual detection pulses was first apodized with a matched exponential function, and then Fourier transformed. All points in the TOF dimension were added together to reproduce as much of the original signal from the encoding phantom as possible. This process was repeated over the bandwidth of the detected gas signal and each reconstructed FID was added to produce the final remotely detected FID. Both the remotely detected and directly detected signals were first zero-filled from 41 to 82 points and apodized with the same Hamming function to reduce truncation artifacts before Fourier transformation.

Images - The TOF images were processed in a similar manner as the remote spectrum, with baseline correction applied in order to remove a DC offset due to the reduced two-step phase cycle. Additionally, the TOF dimension was exploited to reconstruct images as a function of the time taken to reach the detector. Each TOF image was averaged over 12 TOF points. All images were acquired with a resolution of approximately 6 mm and 7 phase encode steps in each dimension. Data were apodized with a Gaussian function and zero filled to 64x64 points before Fourier transforming.

5.3 Results and discussion

A remotely detected spectrum of xenon dissolved in water as well as a set of remotely detected TOF images were obtained for the first demonstrations of Hyper-SAGE. Figure 5.3(a) shows an NMR spectrum of xenon dissolved in water using the direct detection scheme of pulse and acquire. Figure 5.3(b) is the same spectrum acquired using the Hyper-SAGE method, where the spectral information is encoded in the dissolved phase, and detected at a later time in the gas phase (Figure 5.1). Not only has the spectrum been replicated accurately, but comparison of the remote and direct spectra show an enhancement in the signal to noise ratio (SNR) of approximately 3. This enhancement comes about because of the higher concentration of xenon as a gas relative to xenon dissolved in water. With the current implementation in which the extracted gas is neither compressed nor cooled, the maximum theoretical signal enhancement due to the change in concentration is approximately 9, determined by the Ostwald solubility coefficient at room temperature [22]. For this experiment, the xenon gas mixture was dissolved in water with a pressure of 50 psi (340 kPa), however, to decrease the travel time from the extraction membrane to the detector, the gas was extracted under vacuum with a pressure of 4 psi (28 kPa). Under these conditions, the maximum enhancement due to the concentration difference is approximately 4.4. In order to ensure the observed signal enhancement was due to the concentration difference and not a more traditional remote detection enhancement, the filling factor of both the encoding coil and the detection coil were made to be equal. The quality factor (Q) of the detection coil is 1.4 times higher than that of the encoding coil leading to an additional sensitivity of approximately 18%, which is small compared to the overall achieved enhancement.

Images of xenon dissolved in water in the cylindrical encoding phantom were also acquired as a function of the time of flight from the encoding coil to the detection coil (Figure 5.4). Once the encoded spins reach the detector, the acquisition is repeated in intervals of the

sample's residence time in the coil until all of the encoded spins have traveled through the detection coil. The first spins reaching the detector come from the outlet of the encoding phantom. The total travel time for these nuclei to travel from the encoding coil, through the gas extraction membrane, and into the detection coil is around 11 seconds. From a TOF of 17 to 41 s, encoded spins from the main body of the encoding phantom reach the detector, and finally after 47 seconds, the encoded xenon nuclei from the inlet of the phantom are detected.

These results demonstrate that the dissolved phase NMR spectrum of xenon can be obtained via remotely detecting the extracted xenon in the gas phase. Spatial information can also be encoded in order to obtain TOF images. The encoded phase of hyperpolarized xenon spins is stored as the longitudinal magnetization, and therefore survives the travel through magnetic field gradients, and more importantly, a phase change. Additionally, xenon gas has a very long longitudinal relaxation time so encoded information can persist for an extended period of time as can be seen in the TOF images. This allows ample time to prepare the xenon for optimal detection SNR. Through gas compression or liquefaction, the density of xenon could be increased on the order of 10^4 times over xenon dissolved in water. Being a point-by-point method, the time needed to acquire remote data scales with the number of points and therefore can take considerably longer than direct detection. However in situations with samples of low concentration and low filling factor, the signal amplification attainable by Hyper-SAGE surpasses direct signal averaging over a comparable time period.

With the potential of a very large signal enhancement combined with time of flight imaging (unattainable by conventional MRI), Hyper-SAGE seems to be a promising method for studying gas exchange. The TOF images shown in Figure 5.4 contain information about the geometry of the encoding environment as well as the flow path of the water. By including membrane material in the encoding phantom, properties of the gas exchange across the membrane could also be determined both by the time of flight properties of the encoded spins, as well as encoded diffusion information through the gradient [103]. The intrinsically low filling factors in membrane environments provide additional motivation for a remote detection experiment such as Hyper-SAGE. By adopting a microcoil for detection, as is used in microfluidic remote detection [43, 41], extremely high time resolution of the gas exchange process can be achieved in order to study membrane materials such as the gas exchange membranes used in this experiment, or biological samples such as lung tissues.

In conclusion, we have demonstrated a novel method to amplify the solvated hyperpolarized NMR and MRI signals via remote detection of the extracted gas. This method provides a signal enhancement due to concentration differences between dissolved xenon and gas phase xenon, and can be combined with remote detection enhancements in any environment with a low filling factor. Further amplification can be accomplished by either compressing or liquefying the extracted gas. Finally, Hyper-SAGE is also compatible with chemical exchange amplification techniques such as Hyper-CEST making it a valuable tool for diagnostics and molecular imaging in addition to gas exchange studies.
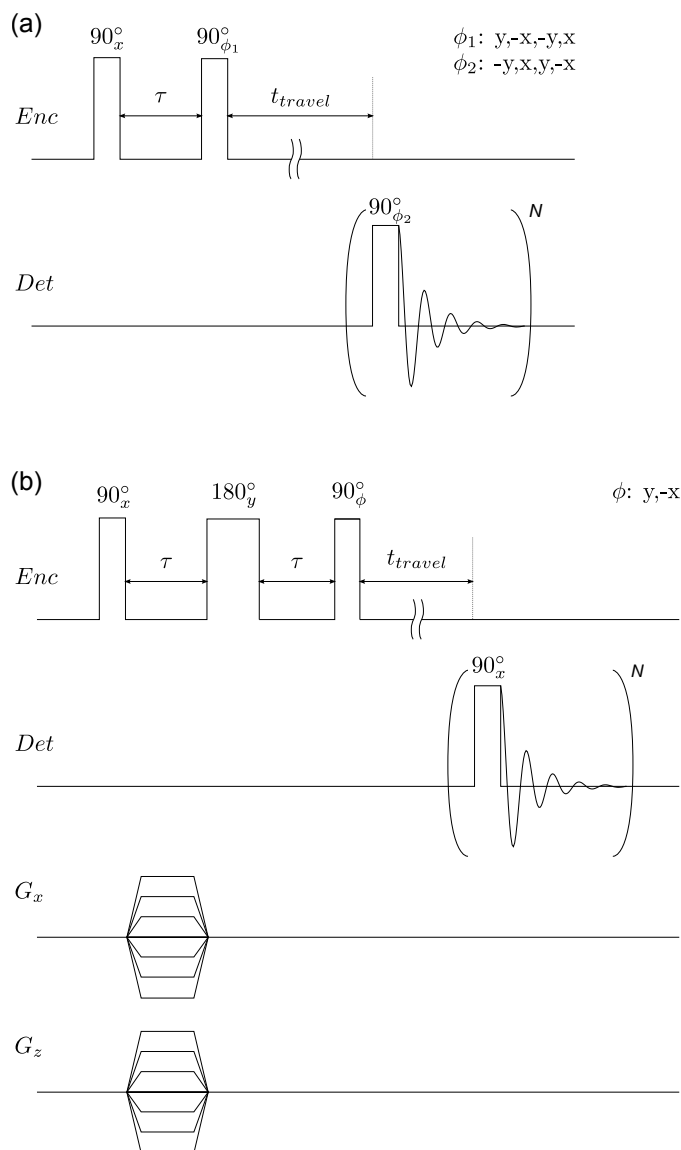
Figure 5.2: Remote detection pulse sequences. (a) Pulse sequence for remote spectroscopy. Initially, a 90° pulse is applied to excite the sample into the transverse plane. The spins are allowed to evolve under chemical shift for a time τ, at which point a second 90° pulse is applied to store the encoded information along the longitudinal axis. The spins then travel to the detection coil where the information is read out with a train of excitation pulses. (b) The pulse sequence for the remote images is similar to the remote spectroscopy, however instead of evolving under chemical shift, spatial information is encoded with phase-encode gradients in the x and z directions. A 180° pulse is also applied before storage to refocus any static field inhomogeneities.
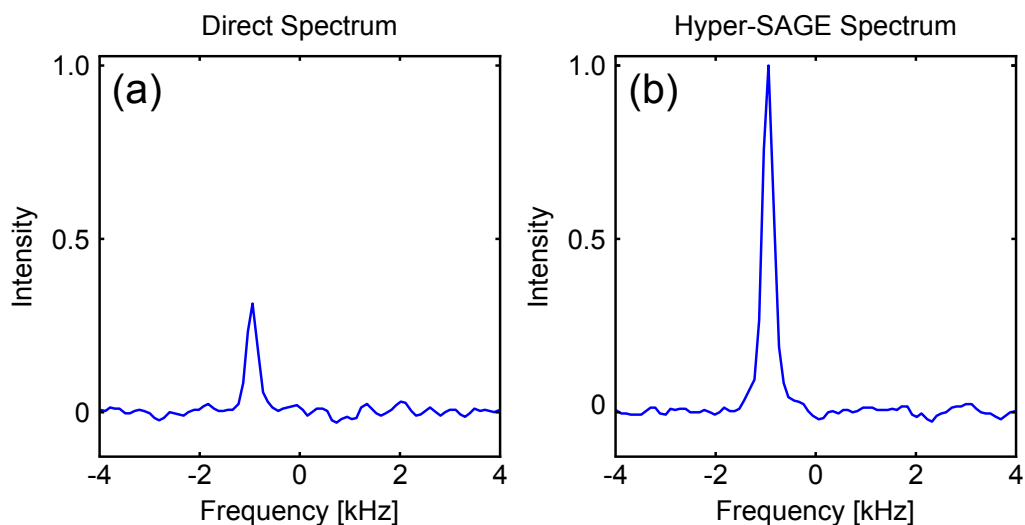
Figure 5.3: Directly detected spectrum (a) and remotely detected Hyper-SAGE spectrum (b) of ^{129}Xe dissolved in water. Both spectra were scaled by their respective noise levels, and an intensity of 1.0 was assigned to maximum signal in the remote spectrum. The same sample was used in both experiments with the detection coil of the direct spectrum being used as the encoding coil for the remote spectrum. Xenon gas is extracted from the encoding volume and flows to the detection coil in the remote experiment resulting in an increased concentration of hyperpolarized Xe, and hence an increase in SNR of approximately 3. Despite being detected at a later time, in a different location, and a different physical state, the original xenon in water spectrum is reproduced exactly.
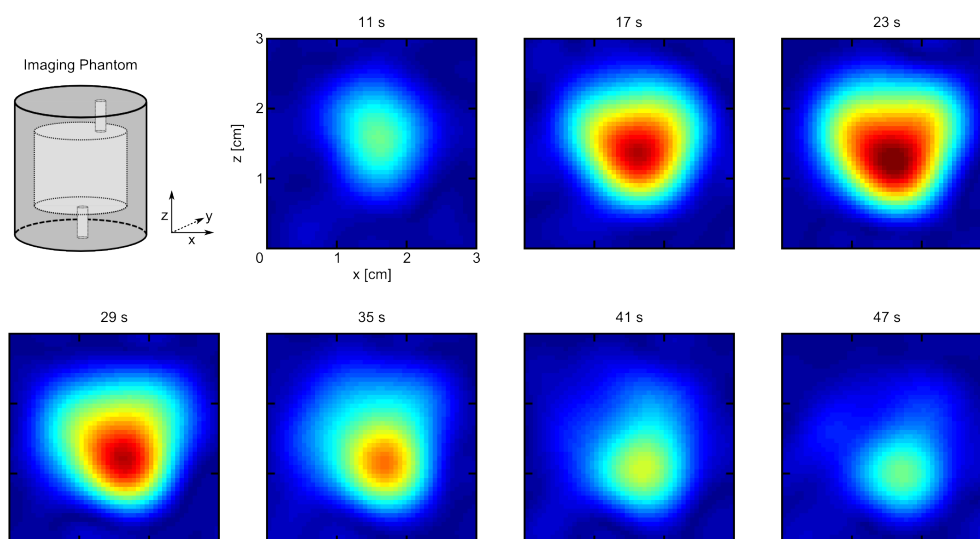
Figure 5.4: Time-of-flight Hyper-SAGE images of xenon dissolved in water continuously flowing through the encoding phantom depicted in the upper left corner. Each image is labeled with its average TOF. The flow is along the positive z-direction, and as such, signal from the top of the phantom at the outlet reaches the detection coil first. Over time, successive portions of the encoded volume are detected until the remaining signal is recovered after 47 s of travel time. The absence of signal at the bottom edges of the encoding phantom is likely due to flow vortices at the inlet preventing the xenon spins from reaching the detector within the longitudinal relaxation time.

Chapter 6

Modular probe design for amplifying the magnetic resonance signal of ^{129}Xe by gas extraction and compression

6.1 Introduction

Remote detection techniques require a minimum of two distinct steps - the encoding step, and the detection step. In order to perform the remote detection experiment proposed in chapter 4, three additional steps are needed. The input step involves getting the gas into solution rapidly and efficiently. The extraction step is responsible for pulling the gas out from solution after encoding has taken place. Finally, the compression step involves concentrating the encoded gas into the detection coil for acquisition. To demonstrate the signal amplification attainable by remotely detecting solution state xenon after it has been extracted and compressed, we developed a mechanical probe capable of performing each of these steps in the bore of a 9.4 T vertical bore superconducting magnet. The probe was designed in a modular fashion, so any of the five systems responsible for the steps listed above could be upgraded, repaired, or replaced without the need to completely disassemble the probe.

There are many challenges in designing such a probe. The probe needs to be constructed completely out of non-magnetic materials. This is straightforward in terms of structural components, tubing, and RF circuit elements. However, designing a non-magnetic compression system proved to be a challenging endeavor. The materials used need to be compatible with hyperpolarized xenon so they will not induce excessive T_1 relaxation. All mechanical components need to be as stable as possible to limit sources of shot noise (section 6.3.3). Finally, and perhaps most challenging, all of the systems need to fit in the 55 mm bore of a superconducting magnet. Descriptions of each stage of the probe can be found in the following section. A detailed schematic of the entire apparatus including the water flow path and all control systems is included at the end of this chapter (Fig. 6.11). Technical drawings of the probe showing critical dimensions can be found in appendix C.
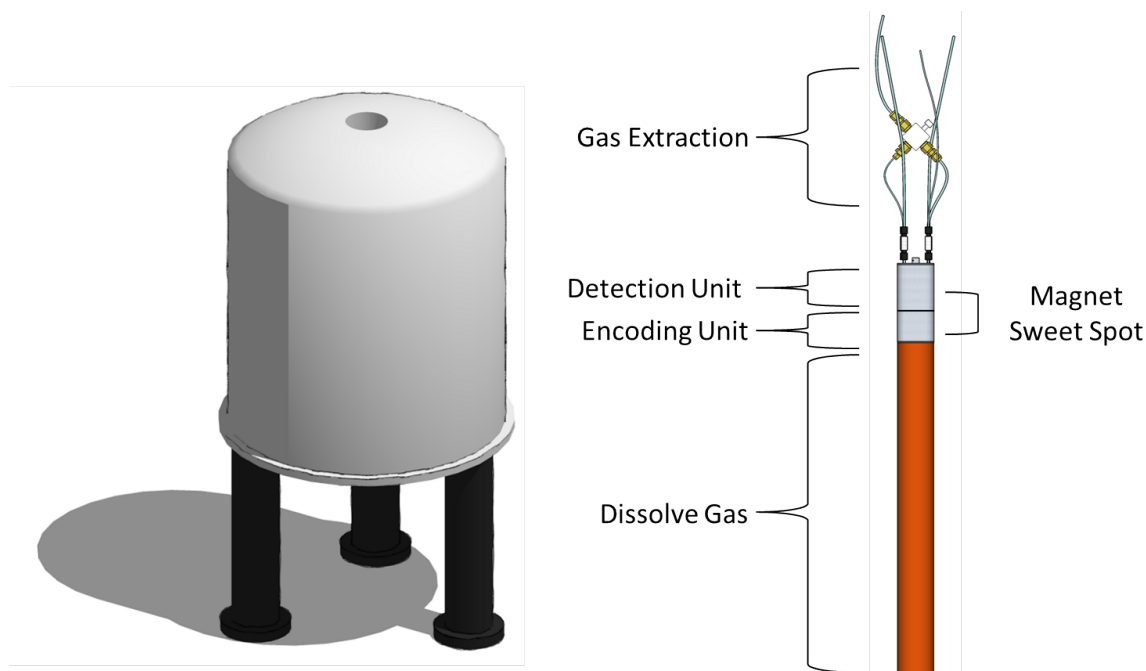
Figure 6.1: Overview of the experimental apparatus. The vertical bore 9.4 T superconducting magnet is shown on the left with the modular gas extraction and compression probe shown on the right. The "sweet-spot" of the magnet is centered between the encoding and detection stages of the probe.

6.2 Five-stage design

6.2.1 Input stage

There are three widely used techniques for getting xenon into solution, bubbling [42], shaking in the presence of a xenon atmosphere [109], and gas transfer with an artificial membrane [4]. The first two techniques require producing xenon batch by batch with stopped flow systems. With artificial gas transfer membranes, saturated solutions of xenon can be produced under continuous flow. Due to the added complexity of a stopped flow system, we chose to use gas transfer membranes for all gas exchange purposes in the probe. These membranes consist of highly hydrophobic polypropylene fibers molded into narrow tubes approximately 100 μm in diameter. The fibers contain pores on the order of a few tens of nanometers in diameter which gas can easily diffuse through, but water cannot due to its surface tension and the hydrophobic nature of the material. With thousands of these fibers packed into a plastic housing, the surface area to volume ratio of the water flowing through them is very high and efficient gas transfer can occur. The input stage of this modular probe simply houses one of these membrane modules (Membrana model G543). Examining figure 6.2, water flows in from the left at a pressure greater than or equal to the applied xenon atmosphere. If the water pressure falls below the gas pressure it will be displaced by the gas and forced out of the membrane. Xenon flows counter to the direction of water flow in order
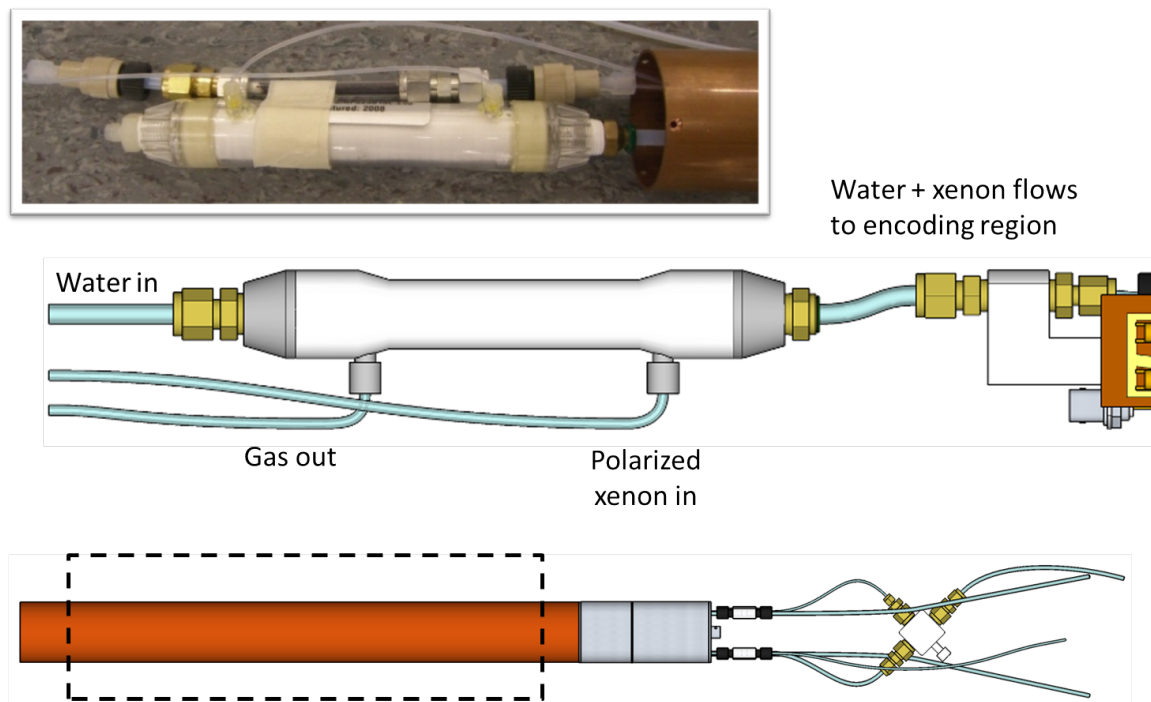
Figure 6.2: Input stage of modular probe.

to further increase the surface area of contact. The xenon flows continuously in order to prevent water vapor from diffusing back to the rubidium vapor cell of the polarizer, as well as to maintain the xenon polarization by not allowing it to spend too much time in transit from the polarizer. In general, higher flow rates of xenon result in larger polarizations at the encoding coil due to the fresh pool of polarized xenon. The water, which was contained in the membrane fibers as it flowed through the gas transfer module, becomes saturated with xenon and flows out the port on the right and into the encoding stage of the probe.

6.2.2 Encoding stage

The encoding stage consists of a teflon support piece, an aluminum shield, an aluminum union connecting the copper shield of the input stage to the aluminum shield of the encoding stage, and the RF coil and associated circuitry. The teflon support piece serves as a scaffolding for the RF circuit, but also provides structural support for the hanging input membrane and BNC cable. Once assembled, the RF coil is completely shielded by the aluminum pieces to prevent cross talk with the detection coil mounted directly above it. Two different encoding stages were built for this probe, one with a 38 mm saddle coil designed to accept a wide variety of samples, and the other was a 12.7 mm solenoid coil permanently wound around a glass phantom. The glass phantom was designed to contain a sample of beads with the xenon biosensor bound to them for the CEST experiments described in chapter 7. Once encoded, the aqueous xenon solutions flow past the detection stage and to the extraction
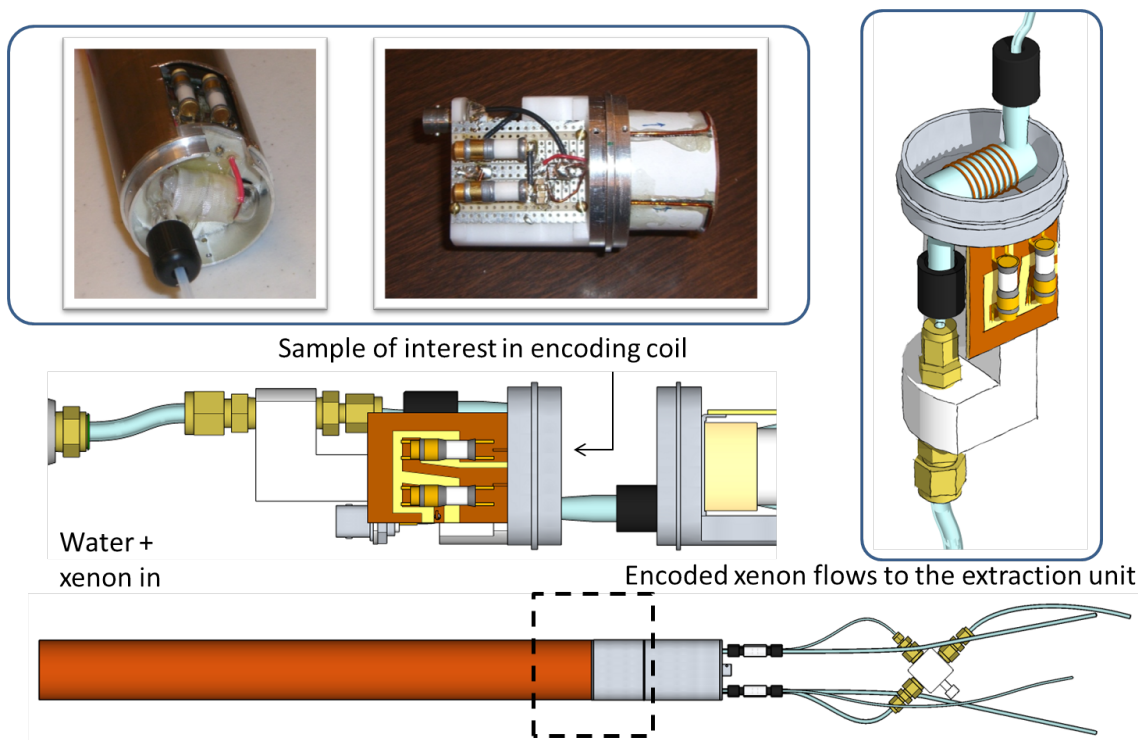
Figure 6.3: Encoding stage of modular probe.

membrane. The detection stage is mounted below the extraction stage in order to keep both the encoding and detection coils as close to the "sweet-spot" of the magnet as possible.

6.2.3 Extraction stage

Like the input stage, the extraction stage simply consists of a commercially available membrane module (Membrana model G591) with two ports for water flow and two for gas flow. This membrane is operated by sealing off one of the gas ports, and pulling a vacuum on the other. The vacuum efficiently extracts the encoded gas from solution at which point it flows back down into the detection stage of the probe.

6.2.4 Detection stage

The detection stage was the most technically difficult section of the probe to design. The primary feature of this section is two pneumatic valves connected by a hollow nylon cylinder with an RF coil wrapped around it. The valves are custom made, non-magnetic pneumatic valves produced by Takasago Electric Inc., Japan, specifically for this application. The valve body is made of PEEK and Teflon with Teflon wetted parts. The spring for the spring return mechanism was made from beryllium-copper, and the mechanical fasteners were made from silicon-bronze. These valves are capable of containing 100 psi at the center input port, with 70-85 psi actuation pressure. The ports are offset from center so when two valves are facing
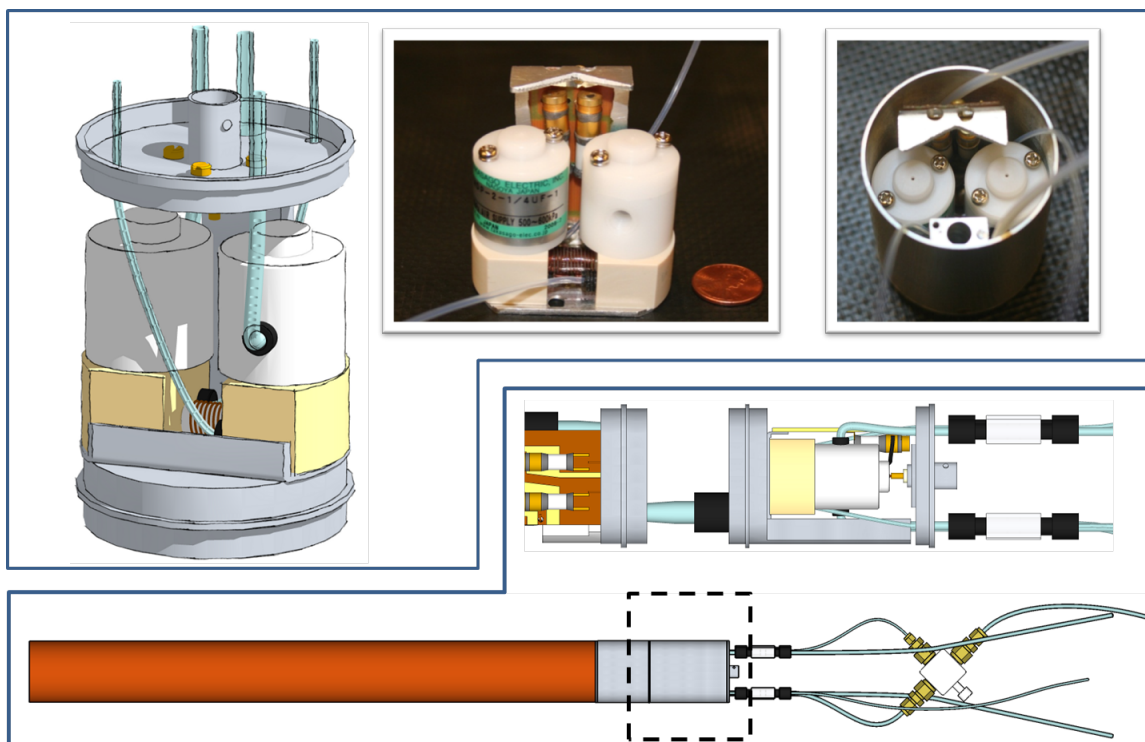
Figure 6.4: Detection stage of modular probe.

each other, the high pressure input ports are aligned forming a region capable of isolating the extracted gas at pressures up to 100 psi. The exhaust ports are aligned opposite each other leaving room for exhaust tubing. The detection unit, including the two valves and the detection coil are mounted to an aluminum union which couples the encoding stage shield to the detection stage shield. A hollow column of aluminum protrudes from this union and extends to the detection stage lid. The purpose of this column is to provide an electrically shielded passageway for the encoded aqueous xenon to travel to the extraction membrane. A BNC connector is mounted to the lid of the detection stage providing structural support between the flimsy BNC cable and the delicate RF circuit. The operation of the valves is primarily determined by the compression system which will be described in the following section.

6.2.5 Compression

The primary component of the compression system is a 10 mL plastic syringe. The plastic and rubber wetted parts are compatible with xenon polarization and the rubber plunger head is capable of maintaining an airtight seal over hundreds, if not thousands of compression cycles. With a narrow body and relatively thick plastic walls, the 10 mL syringe is capable of producing pressures up to 100 psi with minimal bowing. The syringe could be operated with a pneumatic actuator, but we found that a second syringe, 50 mL in volume, worked perfectly well at a fraction of the cost. The plungers of the two syringes were bound
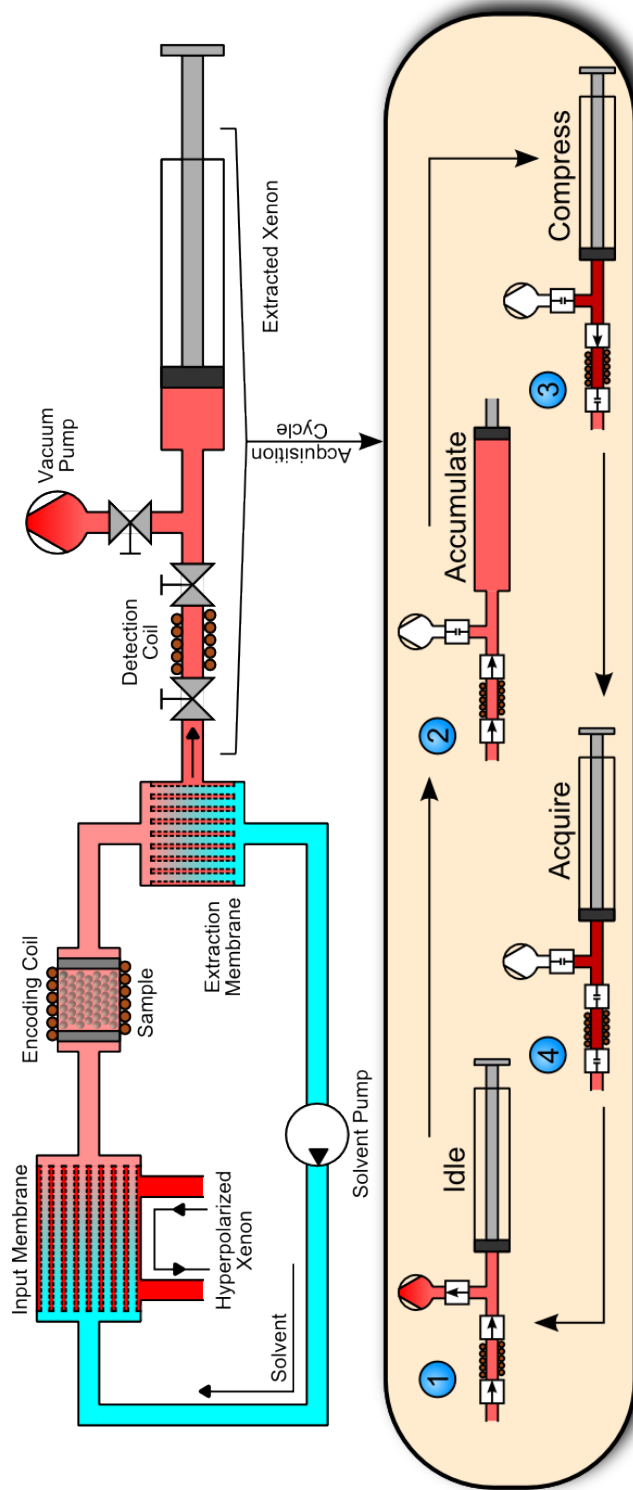
Figure 6.5: Schematic illustrating the operation of the compression system

with aluminum screws and nuts and the syringes were mounted on either side of a wooden box. To extend and compress the 10 mL compression syringe, a vacuum was pulled or pressure was applied on the 50 mL syringe. With twice the diameter of the 10 mL syringe, actuation with the 50 mL syringe provides a 4x mechanical advantage ensuring smooth and reliable extension and compression cycles.

The operation of the compression system is diagrammed in figure 6.5. It consists of a four step cycle which can be described as idle-accumulate-compress-acquire. In the idle phase, the two detection coil valves remain open. A third valve, responsible for isolating the detection system from the vacuum pump, is also open, and the compression syringe is fully compressed. In this orientation, xenon is extracted from solution, flows through the detection coil to the vacuum pump and is vented to atmosphere. Once the sample has been encoded, the system moves on to the accumulation phase. The valve isolating the vacuum closes and the compression syringe is extended. At this point, a closed system is created in which encoded xenon can be extracted from solution and accumulates in the body of the 10 mL syringe. When enough gas has been collected to sufficiently be compressed, the detection coil valve closest to the extraction membrane closes, and the syringe is compressed, forcing the accumulated xenon back into the detection coil. After a short settling time, the second detection coil valve is closed isolating the encoded sample within the RF coil. The second valve is necessary to prevent gas from diffusing in and out of the coil while the signal is being averaged over an echo train. Some of the encoded sample is lost due to the gas remaining in the extraction membrane body. For this reason, the smallest commercially available membrane module, with a gas volume of 2.7 mL, was used.

6.3 Limitations

6.3.1 Compression ratio

To maximize the sensitivity gains in this system, the ratio between the volume of the encoding region and the detection region should be maximized. The volume of the encoding coil is fixed by the dimensions of the sample of interest, so the best option is to minimize the detection region. The smaller the detection coil, the larger the compression ratio and therefore the sensitivity. However, once the detection coil volume is reduced to be on the order of the dead volume in the compression system created by the valves, tubing, extraction membrane, and connectors, further miniaturization of the coil has a negative return on sensitivity. Although the pressure will be marginally higher, the majority of the spin density will be located outside of the coil and only a fraction of the encoded sample will be acquired. Because of the limited space available in the relatively narrow bore of the superconducting magnet, there was little room for optimizing the compression ratio of the two regions in the probe described in this chapter. To partially circumvent this problem, multiple encoding steps can be performed for each detection step to effectively increase the size of the encoding region relative to the detection region. If there are N encoding steps for every detection step, the signal will go up by a factor of N in the detection coil due to

the increased pressure. However, each of these encoding steps is an opportunity to acquire a directly detected transient for averaging, so the actual signal enhancement goes only as the $\sqrt{N}$. Regardless, this approach was necessary for this particular probe due to the limited opportunity for volume optimization.

6.3.2 Longitudinal relaxation

When performing multiple encoding steps for each detection cycle, accumulation times can become quite long. At very long accumulation times, the gain in density of the compressed gas is offset by a loss of magnetization due to longitudinal relaxation. The length of time in which the gas remains in the aqueous phase is constant regardless of the accumulation time and is short compared to the T_1 of xenon in water ($\sim$ 60 s [10]). This leaves the T_1 of xenon in the gas phase as the limiting factor for the maximum gain in sensitivity due to compression. There are three potential sources of T_1 relaxation in this system. The first is relaxation through spin-rotation interactions during ^{129}Xe-^{129}Xe collisions [44]. This relaxation can be approximated by the following

$$\frac{1}{T_1} \simeq 5 \times 10^{-6} \rho \tag{6.1}$$

where T_1 is in seconds and the density ρ is in amagats. Examining the worst case scenario in which we have 100% ^{129}Xe at 100 psi (the maximum pressure maintainable by this probe), the T_1 due to spin-rotation relaxation is over eight hours. It is safe to assume, then, that this form of relaxation is negligible in this system. The second source of relaxation is due to collision of xenon and the walls of its container. This form of relaxation is dependent on the material of the container and the rate of the collisions. As a result, it is far less characterized than spin-rotation relaxation. During the accumulation process, the gas is stored at pressures less than an atmosphere and the collision rate is quite high. Wall relaxation is therefore likely to be the dominant source of relaxation in this system. The final source of relaxation is due to Brownian motion in the presence of a magnetic field gradient. Although it sounds similar to the relaxation causing the attenuation of echo amplitudes in an echo train as discussed in chapter 1, this effect is fundamentally different. The relaxation described previously involved a lack of refocusing of the transverse magnetization due to a difference in the magnitude of the magnetic field before and after a 180° pulse. In this case, the motion itself is inducing the relaxation. When gradients in the transverse magnetic field (e.g. $\partial B_y/dy$) are present, motion along the gradient axis cause the spin to experience an oscillating field in the transverse plane (Fig. 6.6). When the frequency of collisions between atoms is on the order of the Larmor frequency, transitions are induced causing a reduced T_1 relaxation time [93].

Gradient diffusion T_1 reduction is typically not a problem when studying xenon in a superconducting magnet because any gradients in the static field are dwarfed by the magnitude of the field. However, due to size restrictions, the compression syringe sits above the "sweet-spot" of the magnet close to the upper edge of the superconducting coils. The
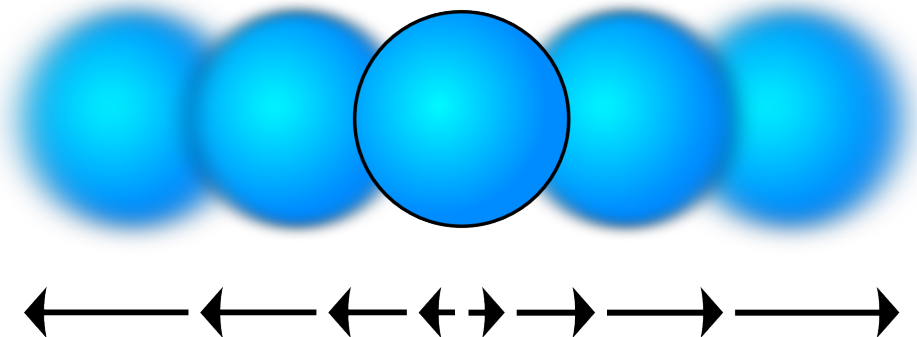
Figure 6.6: A transverse magnetic field gradient appears as an oscillating transverse magnetic field to a spin undergoing Brownian motion along the gradient axis.

gradients in this region can be massive, especially in an actively shielded magnet like the one used for this experiment. To get a rough idea, the field at the center of the magnet is 9.4 T, and 1.5 m directly above the center, the field decays to 0.0005 T. This corresponds to an average gradient of over 6 T/m. Figure 6.7 shows how T_1 is affected for given values of B_0 and gradient strength G. The dotted line represents an approximation of the field along the cylindrical axis of a 9.4 T actively shielded magnet. The relaxation induced by diffusion in a gradient field is on the order of billions of seconds in the "sweet-spot." However, it rapidly drops to be on the order of hundreds of seconds once outside the superconducting solenoid. At this point, the reduction in T_1 is on a time-scale that can start to interfere with the sensitivity gains of this experiment. The field profile used for this simulation had a zero-crossing which is responsible for the rapid dip into nearly instantaneous relaxation on the left of the curve. It's not known if the magnet used in this experiment has a zero-field region, but the effects would be substantial.

Determining the proper accumulation time should be a simple trade-off between the increased concentration at longer accumulation times and the decreased magnetizations due to the effective T_1 of the sample, which is a combination of the wall relaxation and gradient diffusion. However, it turns out to be much more complicated, and to date, we have not been able to determine the cause. Figure 6.8 shows a series of plots with unexplained behavior. In figure 6.8 a) the pressure of the gas in the detection coil after compression versus the accumulation time is shown in green. It's clear from this data that the pressure increases more or less linearly with the accumulation time as would be expected. In blue, the signal from the detection coil after compression is plotted relative to the accumulation time. The data displays an upward trend with accumulation time, but is clearly not linear with smooth peaks and sharp valleys. Figure 6.8 b) shows the same curve, but repeated twice to demonstrate reproducibility of this odd behavior. The position of the peaks and valleys can be shifted by adjusting the water flow rate, suggesting some sort of pressure dependence during the accumulation period. In figure 6.8 c) the same signal versus accumulation time curve is plotted in blue. The green curve is a measurement of T_1 for the same range of accumulation times. This data was determined by accumulating gas for a time τ_{acc}, at which
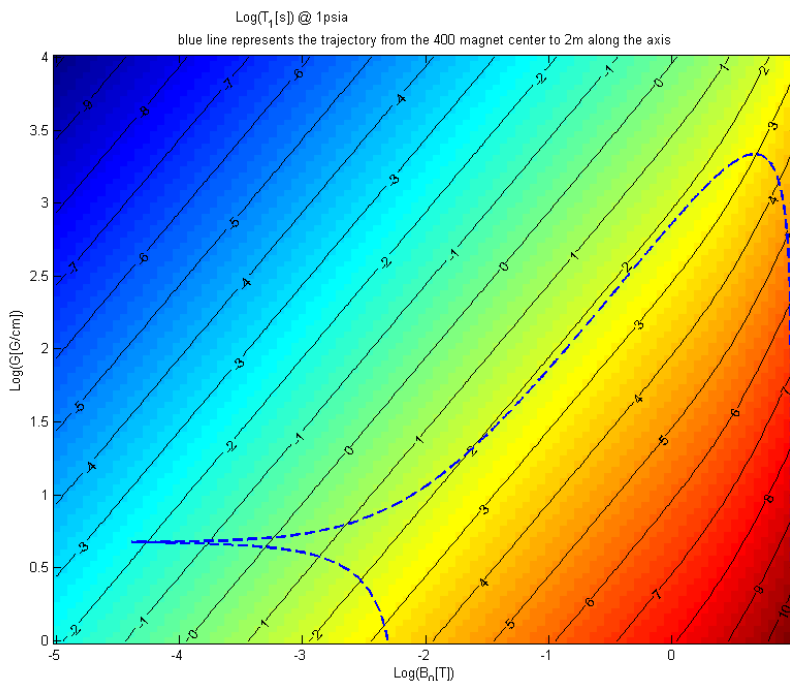
Figure 6.7: Gradient diffusion T_1 reduction in a 9.4 T actively shielded magnet.

point the valve closest to the extraction membrane was shut. No further gas is accumulated at this point. A delay was added before the compression and detection step, and this delay was arrayed in order to obtain an exponential decay representing the T_1 relaxation at a given accumulation pressure. Measuring this rate over the same range of accumulation times shows an effective T_1 that varies from 40 - 140 s and seems to follow the peaks and valleys of the signal curve but approximately 180° out of phase.

Significant effort was spent trying to determine the source of this relaxation with the hopes that eliminating it could greatly improve the performance of the probe. Without success, we were forced to limit accumulation times to approximately 60 seconds.

6.3.3 Shot noise

As mentioned in section 4.3, acquiring a xenon signal from the dissolved phase after it has been extracted to the gas phase requires acquiring each point of the acquisition individually. Variations of the signal intensity from point to point caused by mechanical fluctuations manifest as noise in the acquired data. This phenomenon is referred to as "shot noise." Since the shot noise is proportional to the signal intensity, further amplification of the signal through compression does not increase the signal to shot noise ratio. Due to the number of moving parts required to make gas extraction and compression possible, this apparatus is especially susceptible to shot noise.

Figure 6.9 demonstrates the stability of our apparatus over a set of ten acquisitions. Prior
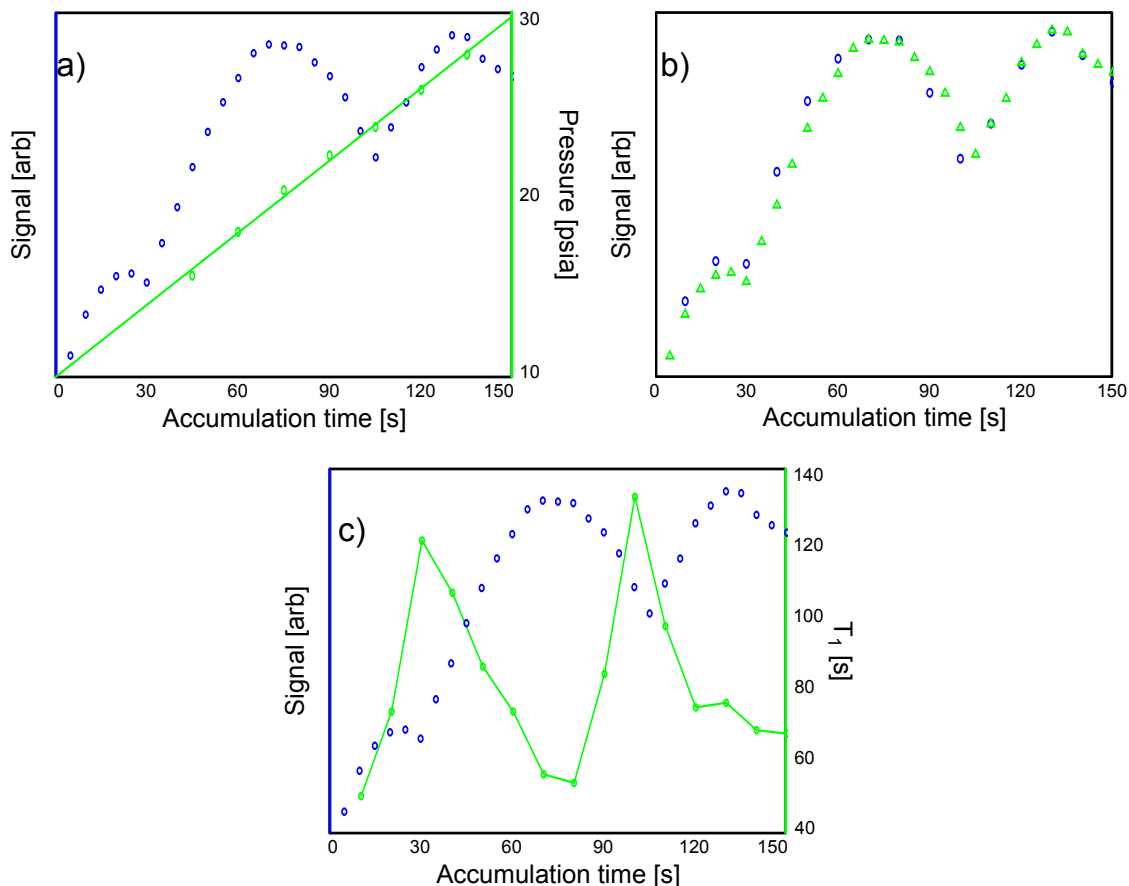
Figure 6.8: Non-linear behavior of the detected signal for various accumulation times. a) detected signal versus accumulation time in blue, and compressed gas pressure vs. accumulation time in green. b) Reproducibility of non-linear behavior. c) The effective T_1 varies with accumulation time (green) and seems to be related to the odd variation of the signal (blue).

to each acquisition, the gas was accumulated for 180 s and compressed to 2.7 atm. The signal varies by approximately 1 % over the course of the acquisition providing an upper limit of 100 on the SNR, regardless of the compression ratio. The data shown in figure 6.9 represents the variation in the amount of xenon, and/or the residual polarization of the xenon in the detection coil at the time of detection. This number is useful when describing the expected SNR of a saturation transfer experiment (described in section 4.4), but when attempting to encode precise phases as is required in a Fourier based remote detection acquisition scheme, the story is considerably different. Fluctuations in the water flow and the xenon input pressure tend to average out over the course of a many second accumulation. However, the time-scale involved in acquiring an NMR spectrum or image is on the order of microseconds to nanoseconds. The instabilities are not sufficiently averaged on such a short timescale and ultimately result in variations of the encoded phase for each acquisition. Therefore,
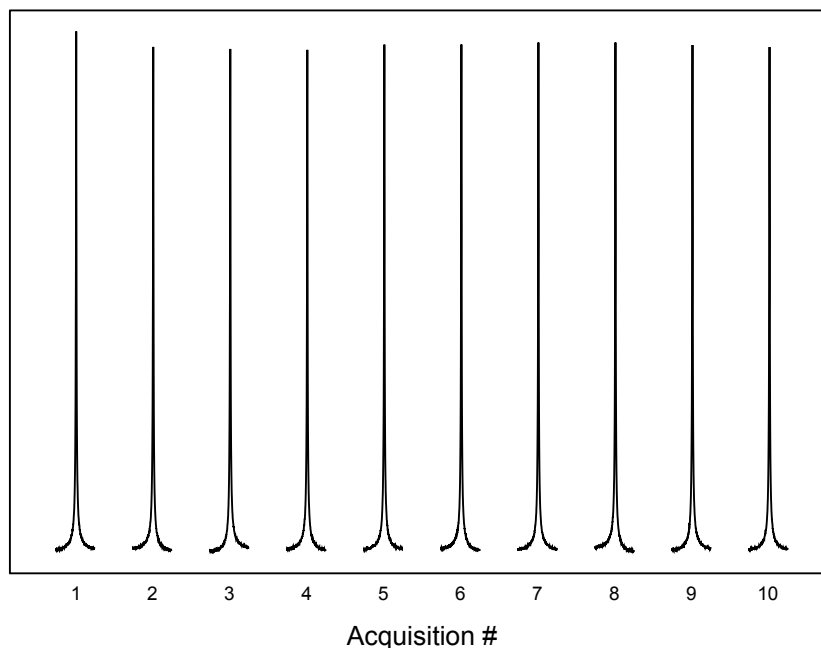
Figure 6.9: Shot to shot variation of the signal intensity in a gas extraction and compression acquisition.

when acquiring a Fourier encoded spectrum or image remotely, the actual signal to shot noise ratio observed with the system described in this chapter is around 10, due to these phase fluctuations. This limits the utility of the gas extraction and compression technique to situations where the signal to noise ratio of a directly acquired spectrum is considerably lower than the signal to shot noise level of the remotely acquired data. For xenon, low concentrations of hyperpolarized gas, or high concentrations of thermally polarized gas are attractive samples for the signal amplification by gas extraction and compression technique.

6.4 Performance of the current design

The maximum enhancement currently achieved with the probe design described above is approximately 20. This enhancement was determined by comparing the spectrum of the directly acquired signal of xenon in water to the remotely acquired spectrum of the same sample after it had been extracted and compressed. This comparison does not take into account the fact that the remotely acquired spectrum has to be detected point by point, so the enhancement of the signal per $\sqrt{t}$ is much less and dependent on the number of points acquired in the spectrum. This enhancement is therefore not large enough to justify the additional time needed to acquire a remotely detected spectrum. However, both a direct and remote saturation transfer experiment require only two acquisitions, one with a preparation pulse on resonance with the target complex, and one off resonance. As a result, we envision the gas extraction and compression technique to be most valuable when combined with the

indirect detection of the xenon biosensor with CEST. In such a scenario, the full enhancement of 20 applies to the remotely detected data.
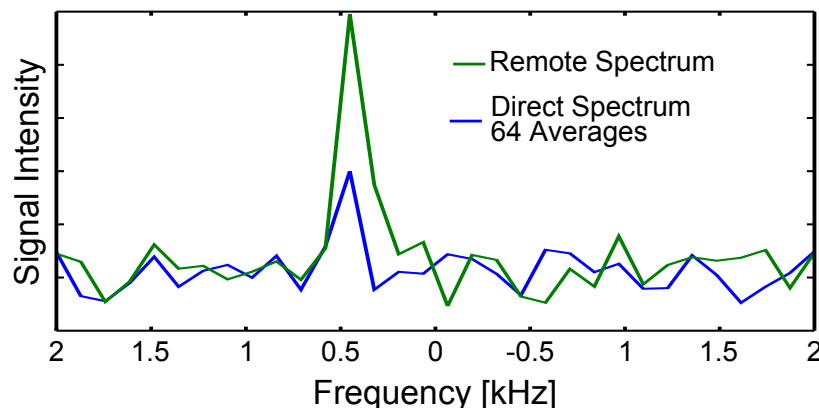
Figure 6.10: Comparison of a directly acquired spectrum (blue) averaged 64 times to the same spectrum acquired remotely after gas was extraction and compression.

The data shown in figure 6.10 was acquired with a sample of 2% natural abundance xenon polarized to 0.3%. The xenon, which is polarized to ∼10% when it exits the polarizer, was run over a bed of ∼100 mg of iron oxide powder to reduce its polarization by a factor of 30. This step was necessary in order to reduce the signal to noise ratio of the directly acquired data below that of the signal to shot noise ratio of the remotely acquired spectrum. Ideally, the enhancement would be determined under more relevant conditions of low xenon concentrations instead of polarization. However, due to the finite volume of the detection region, the accumulation time required with a low concentration of xenon would exceed the observed T_1 of the sample and the depolarization technique was required for the measurement.

The xenon gas mixture was dissolved in water at a pressure of 70 psi (480 kPa) and extracted from solution at a pressure of 2.5 psi (17 kPa). An encoding pulse was applied every 5 s corresponding to the residence time in the encoding phantom. Meanwhile the encoded and extracted gas accumulated in the compression syringe for a total of 60 s prior to compression. The concentration of xenon in the encoding coil was 0.5 mM. Taking into account the detection pressure of approximately 25 psi (170 kPa) and the composition enhancement described in appendix B, the concentration of xenon in the detection coil was approximately 7.5 mM. The increase in concentration from encoding to detection corresponds to an expected enhancement of 15. Comparing the directly detected spectrum to the remotely detected spectrum in figure 6.10, the observed enhancement is closer to 20. The discrepancy in the expected and observed enhancements is likely due to several factors. First, to maximize the enhancement, the pressure sensor and associated tubing was removed to eliminate as much of the dead volume as possible, so the actual pressure is higher than the measured pressure. It is hard to determine the magnitude of this error as the dead volumes of the valves, connectors, and pressure transducer are difficult to estimate. Visual inspection of these elements suggests an error of 10-30% depending primarily on the internal structures

of the valves and pressure transducer. Second, although the encoding coil and detection coil were constructed to have the same filling factor of approximately 25%, due to the solenoid geometry of the detection coil, it is likely that some of the sample beyond the edge of the solenoid and in the dead volume of the valves was detected, effectively increasing the filling factor. Finally, the quality factor, Q, is approximately 1.4 times greater for the 6.4 mm solenoidal detection coil than the 38 mm saddle shaped encoding coil corresponding to an additional gain in sensitivity of approximately 18%.
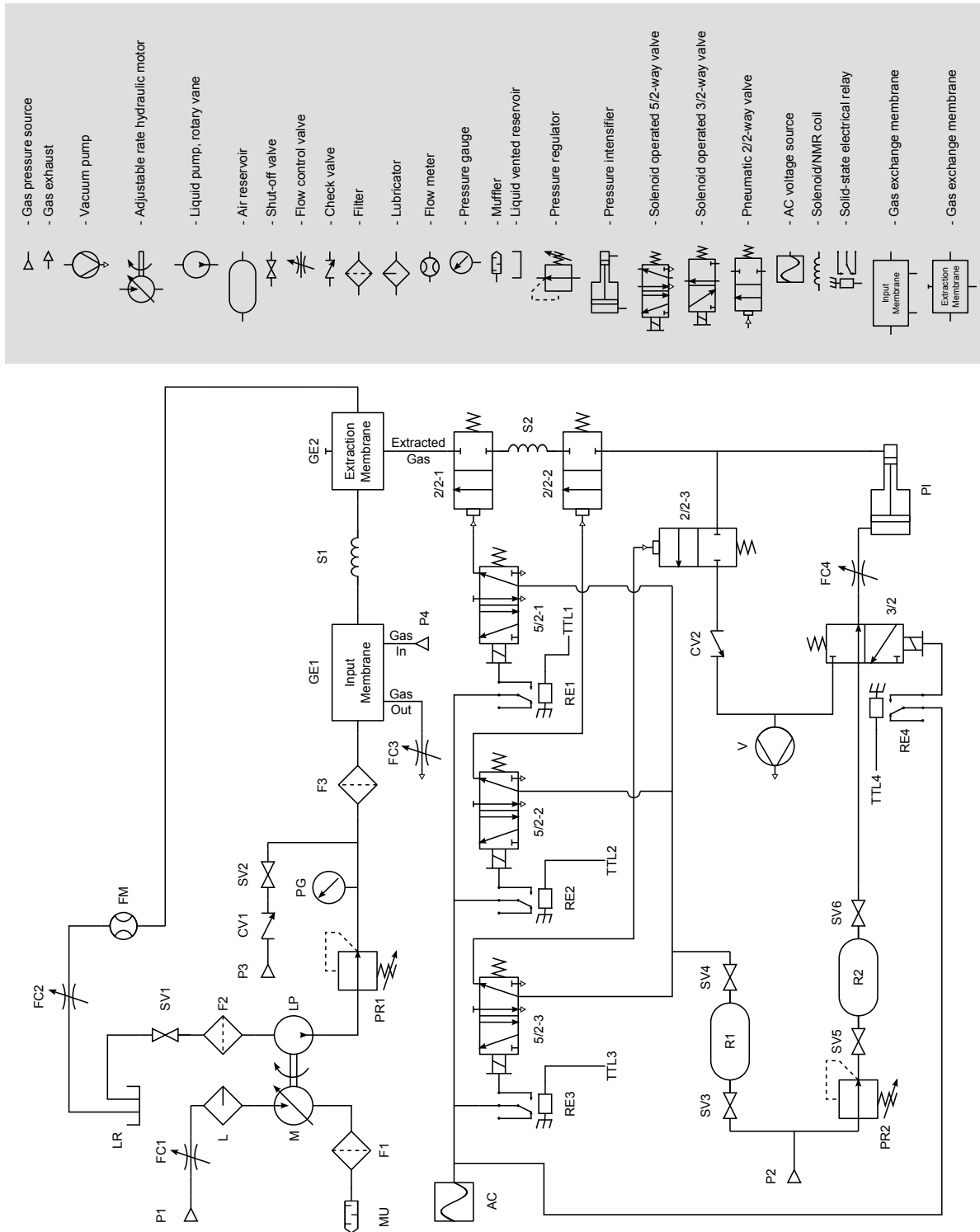
Figure 6.11: Schematic of complete Hyper-SAGE apparatus with compression.

Component	Description
2/2-1-3	Takasago electric PMDP-2-1/4UF-1, custom made, non-magnetic pneumatic 2/2-way valve, 100 PSI, 85 PSI Actuation, spring return
3/2	120 VAC solenoid 3/2-way valve, spring return
5/2-1-3	120 VAC solenoid actuated 5/2-way valve, spring return
AC	120 VAC source
F1-MU	Foam oil filter/muffler attached to the exhaust of the hydraulic motor
F2-3	Polypropylene, 5 micron, 2 GPM
FC1	1/4" needle valve
FC2-4	1/4" Swagelok low flow metering valve
GE1	Membrana model G543
GE2	Membrana model G591
L	In-line drip lubricator
LP	0.8 Max GPM, Rotary vane pump for water
LR	5 Gallon bucket with 1/4" Swagelok connectors added to the bottom and the lid
M	1.7 HP Air-Powered Motor
P1-2	Compressed Air, 85 PSI
P3	Dry Nitrogen, 45 PSI - Used for drying gas exchange membranes
P4	Hyperpolarized Xenon, 55 PSI
PI	50 mL plastic syringe mechanically coupled to a 10 mL plastic syringe
PR1	0-100 PSI liquid pressure regulator
PR2	0-100 PSI inert gas pressure regulator
R1-2	Stainless steel, approximately 1 L
RE1-4	Solid state 120 VAC relay, TTL 5-10 VDC activated
S1	12.7 x 17 mm solenoid coil
S2	6.4 x 12.1 mm solenoid coil
V	0-25" Hg, 1.2 CFM Max flow

Table 6.1: Component descriptions for Fig. 6.11.

Chapter 7

Remote detection of a xenon molecular sensor using thermally polarized xenon with single scan contrast

7.1 Introduction

[129]Xe is an attractive nucleus for use as a highly sensitive molecular contrast agent. The enhanced nuclear polarization attainable by spin-exchange optical pumping (SEOP) [108, 113] provides ample NMR signal to overcome the relatively low concentration of a gas, and the considerable polarizability of its electron cloud allows for efficient dissolution in a variety of solvents and biological tissues. Furthermore, this polarizability gives atomic xenon a chemical shift sensitivity of several hundred ppm in solution [33] making it an ideal sensor to its surrounding chemical environment. Because it has a large nuclear magnetization at low concentrations as well as a significant chemical shift range, hyperpolarized xenon is particularly suited for chemical exchange saturation transfer (CEST) techniques [95, 86, 94] which can lower the sensitivity threshold of xenon complexes by many orders of magnitude. Recently, xenon-cryptophane-based molecular sensors have been detected indirectly at sub-picomolar concentrations [67] with a saturation transfer technique called Hyper-CEST [94]. During a Hyper-CEST experiment, the sample is saturated at the xenon in cryptophane resonance frequency. Due to the chemical exchange, the freshly depolarized xenon atoms from the cryptophane cages reenter the bulk solution and the bulk xenon signal is depleted. By monitoring the depletion of bulk magnetization, the presence of the sensor can be detected indirectly.

Despite the substantial gain in sensitivity of xenon molecular sensors through Hyper-CEST, the technique requires a direct observation of the bulk xenon signal. Depending on the method of delivery, the concentration and/or polarization of bulk xenon in solution at the time of detection may be significantly reduced, e.g., in biological tissues or organs,
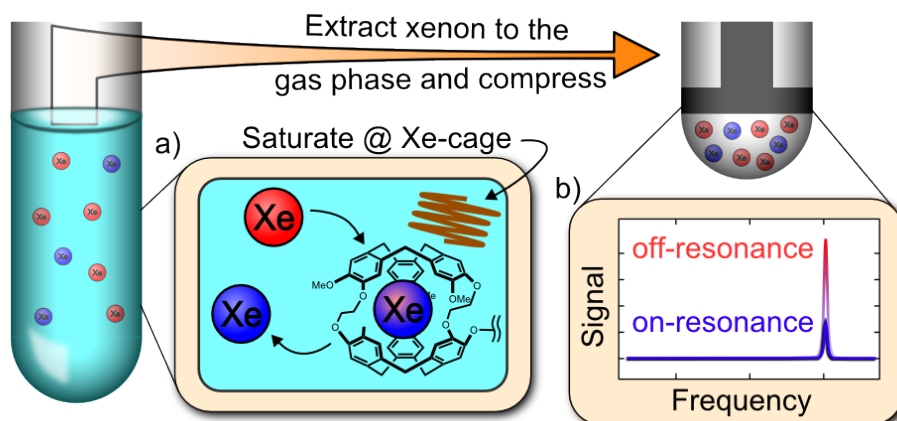
Figure 7.1: Schematic of the gas extraction and compression technique for xenon molecular detection. a) A solution of xenon and a cryptophane-based molecular sensor is saturated at the resonance frequency of xenon associated with the cryptophane cage. Through chemical exchange with the bulk xenon, the overall magnetization of the sample is depleted. Red and blue spheres represent polarized and unpolarized xenon atoms respectively. b) After saturation, the xenon is removed from solution and compressed to amplify the bulk xenon signal. By comparing the residual magnetization after off-resonant and on-resonant saturation pulses, the presence of the molecular sensor can be indirectly determined.

making the indirect detection of the sensor difficult without substantial signal averaging. In such situations, it is advantageous to extract the dissolved xenon into the gas phase prior to detection, a technique called Hyper-SAGE (hyperpolarized xenon signal amplification by gas extraction) [112]. The compressibility of the gas allows for a physical amplification of the bulk xenon signal by increasing its concentration and effectively reviving the detection of the xenon molecular sensor. Furthermore, with enough compression, the bulk xenon signal can be amplified enough to compensate for a lack of hyperpolarization. Using thermally polarized xenon, the effectiveness of CEST techniques is reduced since each saturation event accounts for a smaller percentage of the overall magnetization. However, the accessibility to xenons chemical sensitivity is drastically increased by eliminating the need for an expensive optical pumping apparatus.

7.2 Experimental

7.2.1 Production of aqueous xenon samples

Xenon was dissolved in water using a commercially available gas transfer membrane (Membrana model G543). Water flows through the membrane module at 550 kPa and 1 mL/s and is contained by the hydrophobic porous membrane fibers. Xenon gas mixtures flow through the modules counter to the direction of water flow and can freely penetrate

the porous fibers, efficiently saturating the solution. The hyperpolarized xenon solution was produced by flowing a 2% xenon, 10% N2, and 88% He gas mixture from a homebuilt xenon polarizer [113] at 480 kPa and a rate of 5 mL/s directly to the gas exchange module. A relatively high flow rate of the gas is necessary to minimize the travel time from the polarizer to the water sample. The depolarized sample was produced under similar conditions, but a bed of iron oxide powder (∼100 mg) was inserted in-line between the polarizer and the gas exchange module to decrease the polarization by a factor of 30. The thermally polarized xenon sample was produced by pressurizing the membrane module with 100% Xe at 380 kPa. In order for the polarization to efficiently reach thermal equilibrium, a larger bed of ∼1.3 g of iron oxide powder was inserted in the flow path inside the magnet to reduce the longitudinal relaxation rate. Unlike the two hyperpolarized samples, it is not necessary to flow the gas through the membrane with thermally polarized xenon as the polarization is always at equilibrium and a loss of polarization over time is not a concern. However, to ensure no water vapor would contaminate the source cylinder, the xenon was allowed to flow at an immeasurably small rate. All of the xenon samples were natural abundance 26.4% Xe^{129}.

7.2.2 Saturation transfer acquisition spectra

The acquisition cycle for saturation transfer spectra with gas extraction and compression is detailed in figure 7.2. The acquisition consists of four stages with respect to the mechanical components of the apparatus: idle, accumulation, compression, and acquisition. The idle stage is the default arrangement of the system. With this arrangement, all valves are open and the extracted xenon is vented to atmosphere through a vacuum pump maintaining a constant pressure of 17 kPa. When an acquisition cycle is initiated, the system converts to the accumulation phase. A low power continuous wave saturation pulse is applied to the encoding region which contains the bound molecular sensor. In order to ensure only encoded gas is included for detection, the extracted xenon is vented to atmosphere for a time τ_{trav}, the time required for the sample to flow from the encoding coil to the detection coil. After this delay, a pneumatic valve is closed (V3 in Fig. 7.2 a), isolating the system from the vacuum pump. Simultaneously, the plunger of a 10 mL plastic syringe is fully extended, providing a large volume for the extracted xenon to accumulate. Once a sufficient quantity of gas has been collected, the compression stage begins. After a delay of τ_{trav}, a second pneumatic valve situated between the extraction membrane and the detection coil is closed (V1). The plunger of the syringe is compressed, forcing the accumulated sample back into the detection coil with an elevated pressure. Before acquiring, another delay of two seconds is utilized to ensure compression is complete and the system has settled. The acquisition stage begins by closing a third pneumatic valve on the opposite side of the detection coil, completely confining the encoded sample within the coil. The presence of liquid-gas interfaces and pneumatic valves in close proximity to the detection coil causes a significant amount of susceptibility broadening. However, because the bulk magnetization is the property of interest, the signal can be efficiently averaged over an echo train to compensate for the

relatively broad linewidth. Once the acquisition is complete, the system returns to the idle state, and the process is repeated, varying the saturation frequency for each acquisition. For the spectra presented above, the travel time delay, τ_{trav}, was 2 seconds, and 200 echoes were acquired of each point in the spectra with a 2 ms echo interval. The accumulation time for the two samples involving the 2% Xe gas mixture was 60s, and only 20s for the sample involving 100% Xe. Both the encoding coil and the detection coil were solenoids with internal volumes of 1.9 and 0.1 mL respectively. The extraction module was a Membrana model G591 with a 1 mL liquid volume and 2.7 mL gas volume. Non-magnetic pneumatic valves were custom made by Takasago Electric, Inc. (PMDP-2-1/4UF-1) and are capable of maintaining pressures up to 700 kPa.
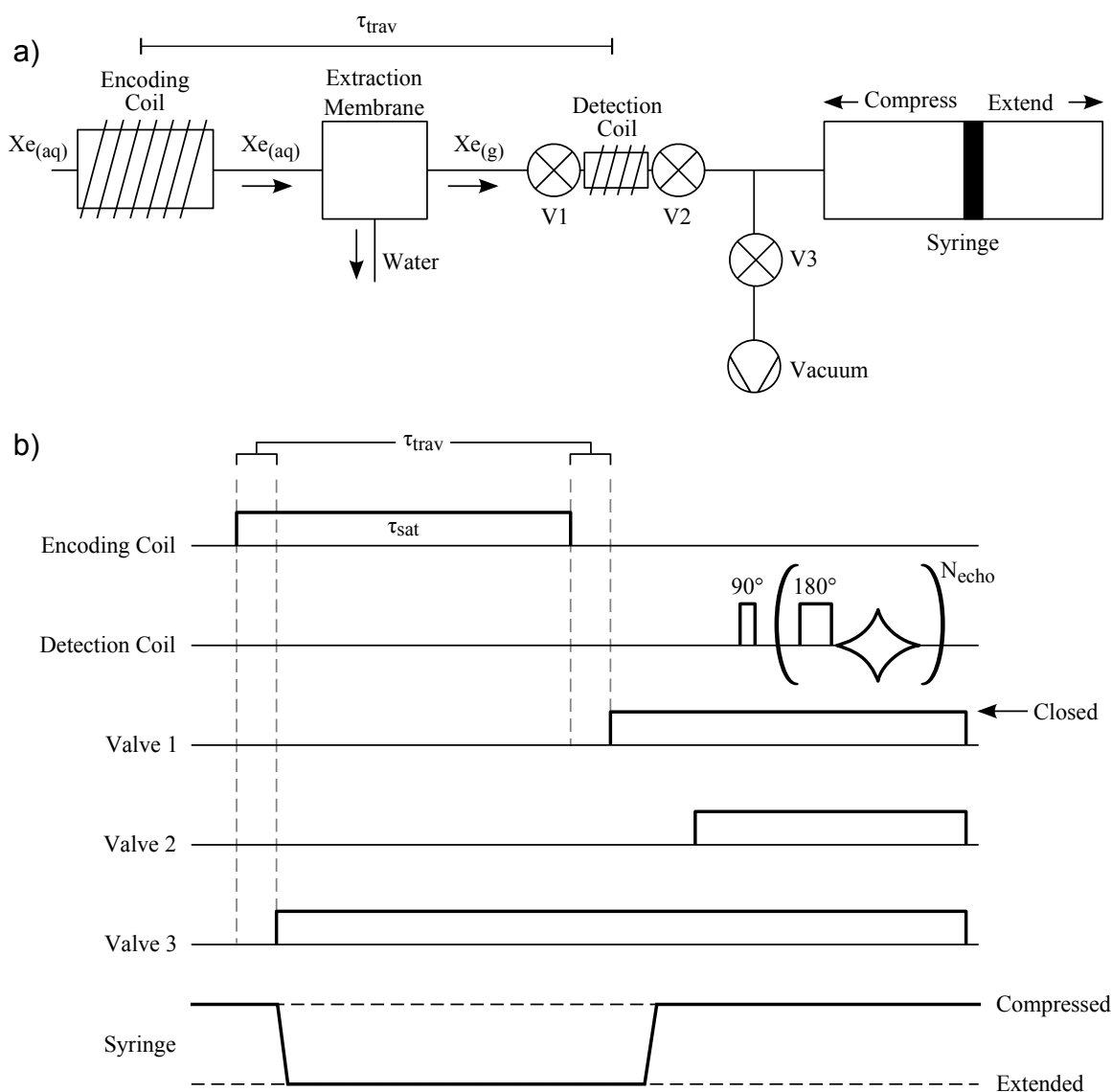

Figure 7.2: Schematic of the acquisition section of the experimental apparatus (a) and the pulse sequence for saturation transfer spectra with gas extraction and compression (b).

7.3   Results

In this study, a cryptophane-A cage based molecular sensor (1.3mM) was bound to polystyrene beads (Advanced Chem Tech, TentaGel S OH, 130 μm diameter) in the bore of a 9.4T superconducting magnet. Three solutions of aqueous xenon were passed over the immobilized sensor and direct spectra were obtained as shown in figure 7.3. The first spectrum (Fig 7.3 a) is from a solution of xenon at 0.4 mM and $\sim$10% polarization. Three peaks are clearly visible in the spectrum, with xenon in water referenced at 193 ppm, xenon associated with the cryptophane cage at 69 ppm, and xenon associated with the polystyrene beads at 220 ppm. In this spectrum, the xenon sensor peak is directly observable due to the relatively high concentration of cryptophane. However, the sensor could still be detected indirectly at much lower concentrations in a Hyper-CEST experiment because of the strong bulk signal from this xenon solution. The second spectrum (Fig 7.3 b) is from a solution of xenon at the same concentration as Fig 7.3 a, but with 30 times less polarization ($\sim$0.3%). Finally, Fig 7.3 c shows the spectrum of thermally polarized xenon ($\sim$0.0009%) at 17 mM. The spectra In Fig 7.3 b&c both required 64 averages to obtain a sufficient signal to noise ratio (SNR) of the bulk xenon in order to perform indirect detection of the xenon sensor. In these scenarios, the detection of the sensor becomes difficult, even at relatively high concentrations, because the limiting factor is now the significantly reduced bulk xenon signal.

To overcome this limitation, a gas extraction and compression system was developed to amplify the xenon signal after Hyper-CEST preparation (Fig 7.1). With this system, the aqueous solutions of xenon continuously flowed over the immobilized sensor, during which, a low power continuous wave (CW) saturation pulse was applied at the frequency of the xenon-cryptophane complex (65 ppm). Due to chemical exchange between xenon in water and in the cage, a depletion of the bulk magnetization occurs. The saturated xenon is then extracted from solution and stored until a sufficient quantity of gas had been collected for compression. After 60 seconds of accumulation, the encoded gas from extraction was compressed, recovering the bulk xenon signal. Upon comparison with a sample in which the preparation was done with an off resonance saturation pulse, the presence of the molecular sensor could be determined.

In order to demonstrate the effectiveness of this system, saturation transfer spectra were obtained for both the highly depolarized and thermally polarized aqueous xenon samples (Fig 7.4). In these spectra, the horizontal axis represents the frequency of the saturation pulse applied to the xenon solution as it flows over the immobilized sensor. The vertical axis is the signal from the bulk xenon after it has been extracted and compressed. Each point therefore represents a complete acquisition cycle from saturation to extraction and compression with saturation frequencies varying from 25 ppm to 250 ppm, at 7.3 ppm intervals. Spline interpolated lines were added to aid in the visualization of the two spectra. Direct acquisition of the bulk xenon signal for both of these samples was not possible without sufficient averaging, but after extraction and compression, the spectrum can be indirectly reconstructed. Additionally, because of the chemical exchange enhancement, the xenon-sensor contrast is enhanced relative to the direct acquisition. Acquiring a spectrum in this manner
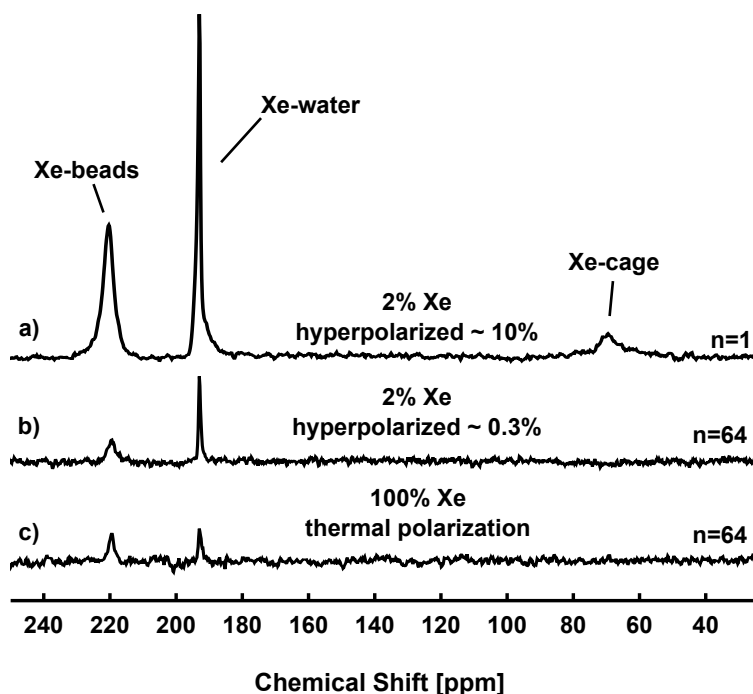
Figure 7.3: Direct spectra of three xenon solutions. Spectra (a) and (b) are from 0.4 mM solutions of Xe in water polarized to ∼10% and ∼0.3% respectively. Spectrum (c) is from a solution of 17 mM Xe with polarization at the thermal equilibrium of ∼0.0009%. Spectrum (a) was directly observable with a single acquisition while spectra (b) and (c) were averaged with 64 transients.

is not optimal as any gains in SNR achieved through the gas extraction and compression are offset by the additional time needed by adding a dimension to the experiment. However, with a priori knowledge of the xenon-sensor resonance frequency, its presence can be determined with only two acquisitions by comparing the residual magnetizations after on resonance and off resonance saturation pulses.

7.4 Conclusion

The combination of Hyper-CEST with gas extraction and compression greatly increases the accessibility of molecular detection using xenon. By physically amplifying the bulk xenon signal, concerns of depolarization during xenon delivery are reduced as the loss in total magnetization can be offset by a gain in magnetization density. Additionally, if the sensor molecule is present in higher concentrations such that a reduction in CEST efficiency can be afforded, this technique opens the door to utilizing thermally polarized xenon for molecular detection. Spin-exchange optical pumping generally requires expensive equipment and a significant investment in time to produce large volumes of highly polarized gas. Thermally
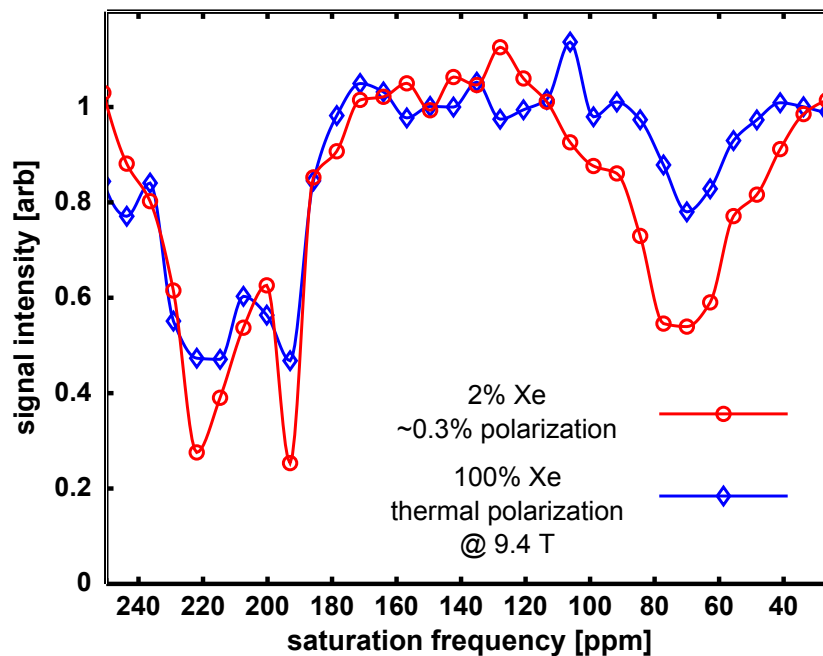
Figure 7.4: Saturation transfer spectra of hyperpolarized xenon after being depolarized by the equivalent of ∼3.5 T_1s (red) and thermally polarized xenon (blue). Each point in the spectra corresponds to an acquisition of the residual magnetization after being saturated at the frequency indicated by the horizontal axis. The xenon was extracted from solution and compressed to amplify the signal for detection. The depleted magnetization measured after saturation at 69 ppm indicates the presence of the xenon molecular sensor.

polarized xenon with gas extraction and compression could therefore provide a low cost alternative to xenon molecular detection.

Bibliography

[1] S. Ahola, J. Perlo, F. Casanova, S. Stapf, and B. Blümich. Multiecho sequence for velocity imaging in inhomogeneous rf fields. *Journal of Magnetic Resonance*, 182:143–151, Sept. 2006.

[2] B. Aksel, L. Marinelli, B. D. Collick, C. Von Morze, P. A. Bottomley, and C. J. Hardy. Local planar gradients with order-of-magnitude strength and speed advantage. *Magnetic Resonance in Medicine*, 58(1):134–43, July 2007.

[3] M. S. Albert, G. D. Cates, B. Driehuys, W. Happer, B. Saam, C. S. Springer Jr., and A. Wishnia. Biological magnetic resonance imaging using laser-polarized 129Xe. *Nature*, 370:199–201, 1994.

[4] N. Amor, P. P. Zänker, P. Blümler, F. M. Meise, L. M. Schreiber, A. Scholz, J. Schmiedeskamp, H. W. Spiess, and K. Münnemann. Magnetic resonance imaging of dissolved hyperpolarized 129Xe using a membrane-based continuous flow system. *Journal of Magnetic Resonance*, 201(1):93–99, Nov. 2009.

[5] S. Anferova, V. Anferov, J. Arnold, E. Talnishnikh, M. A. Voda, K. Kupferschläger, P. Blümler, C. Clauser, and B. Blümich. Improved Halbach sensor for NMR scanning of drill cores. *Magnetic Resonance Imaging*, 25:474–480, May 2007.

[6] S. Appelt, A. Baranga, C. Erickson, M. Romalis, A. Young, and W. Happer. Theory of spin-exchange optical pumping of 3He and 129Xe. *Physical Review A*, 58(2):1412–1439, Aug. 1998.

[7] S. Appelt, F. W. Häsing, H. Kühn, J. Perlo, and B. Blümich. Mobile High Resolution Xenon Nuclear Magnetic Resonance Spectroscopy in the Earths Magnetic Field. *Physical Review Letters*, 94(19):1–4, May 2005.

[8] D. Baumer, E. Brunner, P. Blümler, P. P. Zanker, and H. W. Spiess. NMR Spectroscopy of Laser-Polarized 129Xe Under Continuous Flow: A Method To Study Aqueous Solutions of Biomolecules. *Angewandte Chemie International Edition*, 45(43):7282–7284, 2006.

[9] A. Bax. Two-Dimensional NMR and Protein Structure. *Annual Review of Biochemistry*, 58:223–256, Jan. 1989.

[10] A. Bifone, Y. Q. Song, R. Seydoux, R. E. Taylor, B. M. Goodson, T. Pietrass, T. F. Budinger, G. Navon, and A. Pines. NMR of laser-polarized xenon in human blood. *Proceedings of the National Academy of Sciences*, 93(23):12932–12936, Nov. 1996.

[11] F. Bloch. Nuclear induction. *Physical Review*, 70(7-8):460–474, 1946.

[12] B. Blümich. *NMR imaging of materials.* Oxford University Press, Oxford, 2000.

[13] B. Blümich, J. Perlo, and F. Casanova. Mobile single-sided NMR. *Progress in Nuclear Magnetic Resonance Spectroscopy*, 52:197602, 2008.

[14] C. Bowers and D. Weitekamp. Parahydrogen and synthesis allow dramatically enhanced nuclear alignment. *Journal of the American Chemical Society*, 109(18):5541–5542, 1987.

[15] D. Budker and M. Romalis. Optical magnetometry. *Nature Physics*, 3(4):227–234, 2007.

[16] P. T. Callaghan. *Principles of Nuclear Magnetic Resonance Microscopy.* Clarendon, New York, 1991.

[17] H. Carr and E. Purcell. Effects of diffusion on free precession in nuclear magnetic resonance experiments. *Physical Review*, 94(3):630–638, 1954.

[18] F. Casanova and B. Blumich. Two-dimensional imaging with a single-sided NMR probe. *Journal of Magnetic Resonance*, 163:38–45, July 2003.

[19] J. Cavanagh, W. Fairbrother, A. Palmer III, M. Rance, and N. Skelton. *Protein NMR spectroscopy: principles and practice.* Academic Press, San Diego, 2007.

[20] A. Cherubini and A. Bifone. Hyperpolarised xenon in biology. *Progress in Nuclear Magnetic Resonance Spectroscopy*, 42:1–30, 2003.

[21] T. Chupp and S. Swanson. Medical imaging with laser-polarized noble gases. *Advances in Atomic, Molecular, and Optical Physics*, 45:41–98, 2001.

[22] H. L. Clever and R. Battino. *Krypton, Xenon and Radon: Gas Solubilities.* Pergamon Press, Oxford, 1979.

[23] R. Damadian. Tumor detection by nuclear magnetic resonance. *Science*, 19(3976):1151–1153, 1971.

[24] E. Danieli, J. Mauler, J. Perlo, B. Blumich, and F. Casanova. Mobile sensor for high resolution NMR spectroscopy and imaging. *Journal of Magnetic Resonance*, 198(1):80–87, 2009.

[25] W. Dickinson. Dependence of the F19 Nuclear Resonance Position on Chemical Compound. *Physical Review*, 77(5):736–737, 1950.

[26] B. Driehuys, G. P. Cofer, J. Pollaro, J. B. Mackel, L. W. Hedlund, and G. A. Johnson. Imaging alveolar-capillary gas transfer using hyperpolarized 129Xe MRI. *Proceedings of the National Academy of Sciences*, 103(48):18278–18283, Nov. 2006.

[27] G. Duhamel, P. Choquet, E. Grillon, J. L. Leviel, A. Ziegler, and A. Constantinesco. Global and regional cerebral blood flow measurements using NMR of injected hyperpolarized xenone-129. *Academy of Radiology*, Suppl 2:S498–500, 2002.

[28] G. Eidmann, R. Savelsberg, P. Bluemler, and B. Bluemich. The NMR MOUSE, a Mobile Universal Surface Explorer. *Journal of Magnetic Resonance*, 122(1):104–109, 1996.

[29] R. L. Fagaly. Superconducting quantum interference device instruments and applications. *Review of Scientific Instruments*, 77(10):101101, 2006.

[30] J. M. Franck, V. Demas, R. W. Martin, L.-S. Bouchard, and A. Pines. Shimmed matching pulses: simultaneous control of rf and static gradients for inhomogeneity correction. *The Journal of Chemical Physics*, 131(23):234506, Dec. 2009.

[31] E. Fukushima. Nuclear magnetic resonance as a tool to study flow. *Annual Review of Fluid Mechanics*, pages 95–123, 1999.

[32] G. Giovannetti, V. Hartwig, V. Viti, P. Zadaricchio, L. Meini, L. Landini, and A. Benassi. Low field elliptical MR coil array designed by FDTD. *Concepts in Magnetic Resonance Part B: Magnetic Resonance Engineering*, 33:32–38, 2008.

[33] B. M. Goodson. Nuclear magnetic resonance of laser-polarized noble gases in molecules, materials, and organisms. *Journal of Magnetic Resonance*, 155(2):157–216, 2002.

[34] D. Green, J. Leggett, and R. Bowtell. Hemispherical gradient coils for magnetic resonance imaging. *Magnetic Resonance in Medicine*, 54(3):656–668, Sept. 2005.

[35] B. Grover. Noble-gas NMR detection through noble-gas-rubidium hyperfine contact interaction. *Physical Review Letters*, 40(6):391–392, 1978.

[36] E. L. Hahn. Spin echoes. *Physical Review*, 80(4):580–601, 1950.

[37] S.-I. Han, K. Pierce, and A. Pines. NMR velocity mapping of gas flow around solid objects. *Physical Review E*, 74(1):1–6, July 2006.

[38] W. Happer, E. Miron, S. Schaefer, D. Schreiber, W. Van Wijngaarden, and X. Zeng. Polarization of the nuclear spins of noble-gas atoms by spin exchange with optically pumped alkali-metal atoms. *Physical Review A*, 29(6):3092–3110, 1984.

[39] E. Harel, J. Granwehr, J. A. Seeley, and A. Pines. Multiphase imaging of gas flow in a nanoporous material using remote-detection NMR. *Nature Materials*, 5(4):321–327, Apr. 2006.

[40] E. Harel, C. Hilty, K. Koen, E. McDonnell, and A. Pines. Time-of-Flight Flow Imaging of Two-Component Flow inside a Microfluidic Chip. *Physical Review Letters*, 98(1):5–8, Jan. 2007.

[41] E. Harel and A. Pines. Spectrally resolved flow imaging of fluids inside a microfluidic chip with ultrahigh time resolution. *Journal of Magnetic Resonance*, 193(2):199–206, 2008.

[42] C. Hilty, T. J. Lowery, D. E. Wemmer, and A. Pines. Spectrally Resolved Magnetic Resonance Imaging of a Xenon Biosensor. *Angewandte Chemie*, 118(1):76–79, Jan. 2006.

[43] C. Hilty, E. E. McDonnell, J. Granwehr, K. L. Pierce, S.-I. Han, and A. Pines. Microfluidic gas-flow profiling using remote-detection NMR. *Proceedings of the National Academy of Sciences*, 102:14960–14963, 2005.

[44] E. Hunt and H. Carr. Nuclear Magnetic Resonance of Xe129 in Natural Xenon. *Physical Review*, 130(6):2302–2305, 1963.

[45] M. Hürlimann. Spin Dynamics of CarrPurcellMeiboomGill-like Sequences in Grossly Inhomogeneous B0 and B1 Fields and Application to NMR Well Logging. *Journal of Magnetic Resonance*, 143(1):120–135, Mar. 2000.

[46] A. Jameson, C. Jameson, and H. Gutowsky. Density dependence of 129Xe chemical shifts in mixtures of xenon and other gases. *The Journal of Chemical Physics*, 53(6):2310–2321, 1970.

[47] W. Kilian, F. Seifert, and H. Rinneberg. Dynamic NMR spectroscopy of hyperpolarized (129)Xe in human brain analyzed by an uptake model. *Magnetic Resonance in Medicine*, 51(4):843–847, Apr. 2004.

[48] R. Kimmlingen, M. Gebhardt, J. Schuster, M. Brand, F. Schmitt, and A. Haase. Gradient system providing continuously variable field characteristics. *Magnetic Resonance in Medicine*, 47:800–808, 2002.

[49] R. L. Kleinberg. *Well Logging*, page 4960. John Wiley & Sons, Ltd, Chichester, UK, Mar. 1996.

[50] R. L. Kleinberg and J. A. Jackson. An introduction to the history of NMR well logging. *Concepts in Magnetic Resonance*, 13(6):340–342, 2001.

[51] A. Kumar, D. Welti, and R. R. Ernst. NMR Fourier Zeugmatography. *Journal of Magnetic Resonance*, 18:69–83, 1975.

[52] P. C. Lauterbur. Image Formation by Induced Local Interactions: Examples Employing Nuclear Magnetic Resonance. *Nature*, 242:190–191, 1973.

[53] S. Lee, M. Mössle, W. Myers, N. Kelso, A. Trabesinger, A. Pines, and J. Clarke. SQUID-detected MRI at 132 microT with T1-weighted contrast established at 10 microT-300 mT. *Magnetic Resonance in Medicine*, 53(1):9–14, 2005.

[54] H. Liu and L. S. Petropoulos. Spherical gradient coil for ultrafast imaging. *Journal of Applied Physics*, 81(8):3853–3855, 1997.

[55] M. Lustig and J. M. Santos. Compressed Sensing MRI. *IEEE Signal Processing Magazine*, 25:72–82, Nov. 2008.

[56] T. Maly, G. T. Debelouchina, V. S. Bajaj, K.-N. Hu, C.-G. Joo, M. L. Mak-Jurkauskas, J. R. Sirigiri, P. C. A. van Der Wel, J. Herzfeld, R. J. Temkin, and R. G. Griffin. Dynamic nuclear polarization at high magnetic fields. *The Journal of Chemical Physics*, 128(5):052211, Feb. 2008.

[57] P. Mansfield. Multi-planar image formation using NMR spin echoes. *Journal of Physics C: Solid State Physics*, 10:L55–58, 1977.

[58] B. Manz, A. Coy, R. Dykstra, C. D. Eccles, M. W. Hunter, B. J. Parkinson, and P. T. Callaghan. A mobile one-sided NMR sensor with a homogeneous magnetic field: the NMR-MOLE. *Journal of Magnetic Resonance*, 183:25–31, Nov. 2006.

[59] A. E. Marble, I. V. Mastikhin, B. G. Colpitts, and B. J. Balcom. An analytical methodology for magnetic field control in unilateral NMR. *Journal of Magnetic Resonance*, 174:78–87, May 2005.

[60] M. A. Martens, L. S. Petropoulos, R. W. Brown, J. H. Andrews, M. A. Morich, and J. L. Patrick. Insertable biplanar gradient coils for magnetic resonance imaging. *Review of Scientific Instruments*, 62(11):2639–2645, 2009.

[61] N. Matter, G. Scott, R. Venook, S. Ungersma, T. Grafendorfer, A. Macovski, and S. Conolly. Three-dimensional prepolarized magnetic resonance imaging using rapid acquisition with relaxation enhancement. *Magnetic Resonance in Medicine*, 56:1085–1095, 2006.

[62] J. R. Maze, P. L. Stanwix, J. S. Hodges, S. Hong, J. M. Taylor, P. Cappellaro, L. Jiang, M. V. G. Dutt, E. Togan, A. S. Zibrov, A. Yacoby, R. L. Walsworth, and M. D. Lukin. Nanoscale magnetic sensing with an individual electronic spin in diamond. *Nature*, 455(7213):644–647, Oct. 2008.

[63] E. R. McCarney, B. D. Armstrong, M. D. Lingwood, and S. Han. Hyperpolarized water as an authentic magnetic resonance imaging contrast agent. *Proceedings of the National Academy of Sciences*, 104:1754–1759, Feb. 2007.

[64] P. J. McDonald, P. S. Aptaker, J. Mitchell, and M. Mulheron. A unilateral NMR magnet for sub-structure analysis in the built environment: the Surface GARField. *Journal of Magnetic Resonance*, 185:1–11, Mar. 2007.

[65] E. E. McDonnell, S. Han, C. Hilty, K. L. Pierce, and A. Pines. NMR analysis on microfluidic devices by remote detection. *Analytical chemistry*, 77(24):8109–8114, Dec. 2005.

[66] S. Meiboom and D. Gill. Modified Spin-Echo Method for Measuring Nuclear Relaxation Times. *Review of Scientific Instruments*, 29(8):688–691, 1958.

[67] T. Meldrum, K. L. Seim, V. S. Bajaj, K. K. Palaniappan, W. Wu, M. B. Francis, D. E. Wemmer, and A. Pines. A xenon-based molecular sensor assembled on an MS2 viral capsid scaffold. *Journal of the American Chemical Society*, 132(17):5936–5937, May 2010.

[68] C. A. Meriles, D. Sakellariou, H. Heise, A. J. Moule, and A. Pines. Approach to high-resolution ex situ NMR spectroscopy. *Science*, 293(5527):82–85, July 2001.

[69] M. Moessle, S. Han, W. Myers, S. Lee, N. Kelso, M. Hatridge, A. Pines, and J. Clarke. SQUID-detected microtesla MRI in the presence of metal. *Journal of Magnetic Resonance*, 179(1):146–151, 2006.

[70] H. E. Möller, X. J. Chen, B. Saam, K. D. Hagspiel, G. A. Johnson, T. A. Altes, E. E. de Lange, and H.-U. Kauczor. MRI of the lungs using hyperpolarized noble gases. *Magnetic Resonance in Medicine*, 47(6):1029–1051, June 2002.

[71] A. J. Moule. *Ex situ and remote detection nuclear magnetic resonance.* PhD thesis, University of California, Berkeley, 2003.

[72] A. J. Moule, M. M. Spence, S.-I. Han, J. A. Seeley, K. L. Pierce, S. Saxena, and A. Pines. Amplification of xenon NMR and MRI by remote detection. *Proceedings of the National Academy of Sciences*, 100:9122–9127, 2003.

[73] D. P. Murphy. Advances in MWD and formation evaluation for 1995. *World Oil*, 216:39–49, 1995.

[74] A.-M. Oros and N. J. Shah. Hyperpolarized xenon in NMR and MRI. *Physics in Medicine and Biology*, 49(20):R105–R153, Oct. 2004.

[75] J. L. Paulsen. *The design and application of an adjustable NMR sensor and the MRI imaging of flow in microfluidics with remote detection.* Doctoral thesis, University of California, Berkeley, 2009.

[76] J. L. Paulsen, L. S. Bouchard, D. Graziani, B. Blumich, and A. Pines. Volume-selective magnetic resonance imaging using an adjustable, single-sided, portable sensor. *Proceedings of the National Academy of Sciences*, 105(52):20601–20604, Dec. 2008.

[77] J. L. Paulsen, J. Franck, V. Demas, and L.-S. Bouchard. Least Squares Magnetic-Field Optimization for Portable Nuclear Magnetic Resonance Magnet Design. *IEEE Transactions on Magnetics*, 44(12):4582–4590, Dec. 2008.

[78] J. Perlo, F. Casanova, and B. Blümich. Single-sided sensor for high-resolution NMR spectroscopy. *Journal of Magnetic Resonance*, 180:274–279, June 2006.

[79] J. Perlo, F. Casanova, and B. Blümich. Ex situ NMR in highly homogeneous fields: 1H spectroscopy. *Science*, 315:1110–1112, Feb. 2007.

[80] R. Powers. NMR metabolomics and drug discovery. *Magnetic Resonance in Chemistry*, 47 Suppl 1:S2–11, Dec. 2009.

[81] W. Proctor and F. Yu. The dependence of a nuclear magnetic resonance frequency upon chemical compound. *Physical Review*, 77(5):717, 1950.

[82] K. P. Pruessmann, M. Weiger, M. B. Scheidegger, and P. Boesiger. SENSE: sensitivity encoding for fast MRI. *Magnetic Resonance in Medicine*, 42:952–962, Nov. 1999.

[83] E. Purcell, H. Torrey, and R. Pound. Resonance absorption by nuclear magnetic moments in a solid. *Physical Review*, 69(1-2):37–38, 1946.

[84] D. Raftery, H. Long, T. Meersmann, P. J. Grandinetti, L. Reven, and A. Pines. High-Field NMR of Adsorbed Xenon Polarized by Laser Pumping. *Physical Review Letters*, 66(5):584–587, 1991.

[85] N. Ramsey. Magnetic shielding of nuclei in molecules. *Physical Review*, 78:699–703, 1950.

[86] K. Ruppert, J. Brookeman, K. Hagspiel, and J. Mugler III. Probing lung physiology with xenon polarization transfer contrast (XTC). *Magnetic Resonance in Medicine*, 44(3):349–357, 2000.

[87] I. Ruset, S. Ketel, and F. Hersman. Optical Pumping System Design for Large Production of Hyperpolarized Xe129. *Physical Review Letters*, 96(5):8–11, Feb. 2006.

[88] B. T. Saam, D. A. Yablonskiy, V. D. Kodibagkar, J. C. Leawoods, D. S. Gierada, J. D. Cooper, S. S. Lefrak, and M. S. Conradi. MR imaging of diffusion of (3)He gas in healthy and diseased lungs. *Magnetic Resonance in Medicine*, 44:174–179, Aug. 2000.

[89] D. Sakellariou, G. Le Goff, and J.-F. Jacquinot. High-resolution, high-sensitivity NMR of nanolitre anisotropic samples by coil spinning. *Nature*, 447:694–697, June 2007.

[90] R. Sander. Compilation of Henry's law constants for inorganic and organic species of potential importance in environmental chemistry, 1999.

[91] I. Savukov and M. Romalis. NMR Detection with an Atomic Magnetometer. *Physical Review Letters*, 94(12):1–4, Mar. 2005.

[92] I. M. Savukov, S. J. Seltzer, and M. V. Romalis. Detection of NMR signals with a radio-frequency atomic magnetometer. *Journal of Magnetic Resonance*, 185(2):214–220, Apr. 2007.

[93] L. D. Schearer and G. K. Walters. Nuclear Spin-Lattice Relaxation in the Presence of Magnetic-Field Gradients. *Physical Review A*, 139(5A):1398–1402, 1965.

[94] L. Schroder, T. Lowery, C. Hilty, D. Wemmer, and A. Pines. Molecular imaging using a targeted magnetic resonance hyperpolarized biosensor. *Science*, 314(5798):446–449, 2006.

[95] A. Sherry and M. Woods. Chemical exchange saturation transfer contrast agents for magnetic resonance imaging. *Annual Review of Biomedical Engineering*, 10:391–411, 2008.

[96] R. Shulman and D. Rothman, editors. *Metabolomics by in vivo NMR*. Wiley, West Sussex, 2005.

[97] Y. Song, H. Gaede, T. Pietrass, G. Barrall, G. Chingas, M. Ayers, and A. Pines. Spin-polarized 129Xe gas imaging of materials. *Journal of Magnetic Resonance, Series A*, 115(1):127–130, 1995.

[98] R. E. D. Souza, K. Schlenga, A. Wong-foy, R. Mcdermott, A. Pines, and J. Clarke. NMR and MRI Obtained with High Transition Temperature DC SQUIDs. *Journal of the Brazilian Chemical Society*, 10(4):307–312, 1999.

[99] M. Spence, S. Rubin, I. Dimitrov, E. Ruiz, D. Wemmer, A. Pines, S. Yao, F. Tian, and P. Schultz. Functionalized xenon as a biosensor. *Proceedings of the National Academy of Sciences*, 98(19):10654–10657, 2001.

[100] M. K. Stehling, R. Turner, and P. Mansfield. Echo-Planar Imaging: Magnetic Resonance Imaging in a Fraction of a Second. *Science*, 254(3):43–50, 1991.

[101] S. D. Swanson, M. S. Rosen, B. W. Agranoff, K. P. Coulter, R. C. Welsh, and T. E. Chupp. Brain MRI with Laser-Polarized 129Xe. *Magnetic Resonance in Medicine*, 38(5):695–698, Nov. 1997.

[102] S. D. Swanson, M. S. Rosen, K. P. Coulter, R. C. Welsh, and T. E. Chupp. Distribution and dynamics of laser-polarized (129)Xe magnetization in vivo. *Magnetic Resonance in Medicine*, 42(6):1137–1145, Dec. 1999.

[103] V.-V. Telkki, C. Hilty, S. Garcia, E. Harel, and A. Pines. Quantifying the diffusion of a fluid through membranes by double phase encoded remote detection magnetic resonance imaging. *The Journal of Physical Chemistry B*, 111(50):13929–13936, Dec. 2007.

[104] D. Topgaard, R. W. Martin, D. Sakellariou, C. A. Meriles, and A. Pines. "Shim pulses" for NMR spectroscopy and imaging. *Proceedings of the National Academy of Sciences*, 101(51):17576–17581, Dec. 2004.

[105] V. Tugarinov, P. M. Hwang, and L. E. Kay. Nuclear magnetic resonance spectroscopy of high-molecular-weight proteins. *Annual Review of Biochemistry*, 73:107–146, Jan. 2004.

[106] R. Turner. Minimum inductance coils. *Journal of Physics E: Scientific Instrumentation*, 21:948–952, 1988.

[107] R. Turner. Gradient coil design: a review of methods. *Magnetic Resonance Imaging*, 11:903–920, 1993.

[108] T. G. Walker and W. Happer. Spin-exchange optical pumping of noble-gas nuclei. *Reviews of Modern Physics*, 69(2):629–642, 1997.

[109] J. Wolber. Measuring diffusion of xenon in solution with hyperpolarized 129Xe NMR. *Chemical Physics Letters*, 296(3-4):391–396, Nov. 1998.

[110] S. Xu, V. V. Yashchuk, M. H. Donaldson, S. M. Rochester, D. Budker, and A. Pines. Magnetic resonance imaging with an optical atomic magnetometer. *Proceedings of the National Academy of Sciences*, 103(34):12668–12671, Aug. 2006.

[111] W. Yen and R. Norberg. Nuclear Magnetic Resonance of Xe129 in Solid and Liquid Xenon. *Physical Review*, 131(1):269–275, 1963.

[112] X. Zhou, D. Graziani, and A. Pines. Hyperpolarized xenon NMR and MRI signal amplification by gas extraction. *Proceedings of the National Academy of Sciences*, 106(40):16903–16906, 2009.

[113] X. Zhou, J. Luo, X. Sun, X. Zeng, M. Zhan, S. Ding, and M. Liu. Experimental and dynamic simulations of radiation damping of laser-polarized liquid 129Xe at low magnetic field in a flow system. *Applied Magnetic Resonance*, 26:327–337, 2004.

[114] X. Zhou, M. L. Mazzanti, J. J. Chen, Y. Tzeng, J. K. Mansour, J. D. Gereige, A. K. Venkatesh, and Y. Sun. Reinvestigating hyperpolarized 129 Xe longitudinal relaxation time in the rat brain with noise considerations. *NMR in Biomedicine*, 30(June 2007):217–225, 2008.

[115] X. Zhou, X.-P. Sun, J. Luo, X.-Z. Zeng, M.-L. Liu, and M.-S. Zhan. Production of Hyperpolarized 129Xe Gas Without Nitrogen by Optical Pumping at 133Cs D2 Line in Flow System. *Chinese Physical Letters*, 21(8):1501–1503, 2004.

Appendix A

Single-sided gradient optimization code

A.1   Source code for optimal uniplanar gradient coil

The following code performs all three steps of the gradient optimization procedure: magnetic field inversion, current discretization, and field verification. This code in particular is used to calculate an x gradient coil. It can easily be modified for the other two dimensions by specifying a gradient along y or z for $\mathcal{B}_{z,j}$ and substituting in the appropriate symmetry simplifications. The Biot-Savart estimation of the magnetic field is done in a separate program which was written in Fortran in order to decrease the processing time. This code can be found in section A.2.

```
%This m−file computes an optimal coil winding for a single sided
%x gradient minimizing the inductance and matching a target field
function [] = optimal_x_coil()

%declare global variables needed for the numerical integration
global a x y z lambda index_i index_j

%'a' is the distance from the gradient plane to the center of the
%sweetspot
a=0.015;          %[m]
num_cont = 20;    %number of contours − determines number of
                  %windings
gamma = 7000;     %filter coefficient for gaussian filtering

%define the constraints for the linear x gradient field
x = [0.00025  0.00025     0.02      0.00025     0.002];        %[m]
y = [0        0.01        0         0          −0.01];         %[m]
z = [0        0           0         0.01        0];            %[m]
```

```
Bz=([0.010    0.008        1.125        0.008        0.2]*1e-3)';    %[T]


%define permeability constant [si units]
mu0 = 4*pi*1e-7;


%limits for numerical integration of Cij
%alpha=k_x and beta=k_z
alpha_min = -1000;
alpha_max = 1000;
beta_min = -1000;
beta_max = 1000;


%tolerance for the numerical integration. Smaller values yield
%more precise results
tol = 1e-6;


%plot each function being integrated in order to check if the
%integration limits are high enough
alpha = linspace(alpha_min, alpha_max, 100);
beta = linspace(beta_min, beta_max, 100);
[AA,BB] = meshgrid(alpha, beta);
H1 = figure(1);
set(H1,'name','CHECK_INTEGRATION_LIMITS');
plot_index = 1;
for index_i = 1:length(x)
    for index_j = 1:length(x);
        %plot the integrand
        subplot(length(x),length(x),plot_index);
        cish = integrnd(AA,BB);
        surf(AA,BB,cish);
        shading flat;

        %integrate to determine the Cij matrix
        c(index_i, index_j) = mu0/(8*pi^2)*...
            dblquad(@integrnd, alpha_min, alpha_max+0.000001,...
            beta_min, beta_max+0.000001, tol);
        axis([min(min(alpha)) max(max(alpha)) min(min(beta))...
                max(max(beta)) min(min(cish)), max(max(cish))]);
        axis off;

        %increment
        plot_index=plot_index+1;

        %pause for a ms in case we want to abort with ctrl C
        pause(0.01);
```

```
      end
end

%pause long enough to ensure the integration
%limits on the previous plot are high enough
pause(1);

%determine the lagrange multipliers lambda with the pseudoinverse
%of C
lambda = c\Bz;

%set up the coords for jx(alpha,beta) which we will FT to Jx(x,z)
%SW_x = delta lambda_x = 2*pi/delta_alpha
alpha = (−1000*pi−1e−6)/1:4*pi/1:1000*pi/1;        %SW_x = 0.5 [m]
beta = −1000*pi−1e−6:4*pi:1000*pi;                 %SW_z = 0.5 [m]
[AA,BB]=meshgrid(alpha,beta);

%set up the coords for the real space Jx(x,z)
[XX,ZZ]=meshgrid(linspace(−0.25,0.25,length(alpha)),...
    linspace(−0.25,0.25,length(beta)));

%calculate jx(alpha,beta) with the lambdas determined previously,
%filter and FT to obtain the real current density Jx(x,z)
[jx,jz] = j_ab(AA,BB,x,y,z,a,lambda);
jx = jx.*exp(−gamma*(XX.^2+ZZ.^2));
Jx = real(fftshift(ifftn(ifftshift(jx))));

%set up a large figure for plotting the final gradient design
close(1)
H1 = figure(1);
pos = get(H1,'position');
set(H1,'position',[14,40,1000,650]);

%integrate Jx approximately by a cumulative sum to get the stream
%function
Sy = cumsum(Jx,1);

%plot the contours of SY which represent discrete wires of
%current saving the contours in the variable cont in order to be
%used by the biot−savart program
figure(2);
cont = contour(XX,ZZ,Sy,num_cont);
title('x_gradient_winding_pattern');
xlabel('x_[cm]');
ylabel('z_[cm]');
```

```matlab
axis equal

%calculate the magnetic field using biot−savart and plot
figure(1);
subplot(2,1,1)
[XX,YY,ZZ,Bz]=CoilField(cont, a);

%plot contours of Bz in the x−z plane
subplot(2,2,3);
contourf(linspace(−1,1,21),linspace(−2.5,2.5,21),...
    squeeze(Bz(11,:,:)),20);
xlabel('z [cm]');
ylabel('x [cm]');
title('Bz [gauss/A] in the y=0 plane');
view(90,90);
axis square;
colorbar;

%plot contours of Bz in the x−y plane
subplot(2,2,4);
contourf(linspace(−2.5,2.5,21),linspace(−1,1,21),...
    squeeze(Bz(:,:,11)),20);
xlabel('x [cm]');
ylabel('y [cm]');
title('Bz [gauss/A] in the z=0 plane');
axis square;
colorbar;

%—————————————————————————————————————————————

%This function is used by dblquad in order to numerically
%integrate the coefficients of the lagrange multipliers Cij
function out = integrnd(alpha,beta)

%These variables have to be global instead of being passed into
%the function because of the way dblquad works
global a x y z index_i index_j

%This is the integrand for Cij
out = beta.^2./sqrt(alpha.^2+beta.^2).*sin(alpha*x(index_i))*...
    i.*sin(alpha*x(index_j))*i.*cos(beta*z(index_i)).*...
    cos(beta*z(index_j)).*exp(−sqrt(alpha.^2+beta.^2)*...
    (y(index_i)+a)).*exp(−sqrt(alpha.^2+beta.^2)*(y(index_j)+a));

%—————————————————————————————————————————————
```

```
%This function takes in values of alpha, beta, the constraint
%points, and the lagrange multipliers determined by minimization
%and returns a function of the current density in k−space
function [jx_out,jz_out] = j_ab(alpha,beta,x,y,z,a,lambda)

%reshape x,y,z, and lambda which are vectors if there is more
%than one constraint in order to vecorize the summing process
x = repmat(reshape(x,1,1,[]),[size(alpha,1),size(alpha,2),1]);
y = repmat(reshape(y,1,1,[]),[size(alpha,1),size(alpha,2),1]);
z = repmat(reshape(z,1,1,[]),[size(alpha,1),size(alpha,2),1]);
lambda = repmat(reshape(lambda,1,1,[]),[size(alpha,1),...
    size(alpha,2),1]);

%reshape alpha and beta for vectorized summing purposes
alpha_fs = repmat(alpha,[1,1,size(x,3)]);
beta_fs = repmat(beta,[1,1,size(x,3)]);

%calculated jx(alpha,beta)
jx_out = −beta.^2./sqrt(alpha.^2+beta.^2).*...
    sum(lambda.*sin(alpha_fs.*x)*i.*cos(beta_fs.*z).*...
    exp(−sqrt(alpha_fs.^2+beta_fs.^2).*(y+a)),3);

%calculate jz(alpha,beta)
jz_out = −jx_out.*alpha./beta;

%————————————————————————————————————————————————————————

%This function takes in a set of contour lines produced by the
%make_coil funtion and calculates the magnetic field over a
%region of interest using the biot−savart law.
function [XX,YY,ZZ,Bz] = CoilField(cont,a)

%number of points to evaluate on the grid
npx = 21;
npy = 21;
npz = 21;

%length of each side of the ROI
lx = 0.05;
ly = 0.02;
lz = 0.02;

%length of each side of the coil
cx = 0.241; %[m]
```

```
cz = 0.168; %[m]


%wire_thickness is used to avoid evaluating the magnetic field at
%small values of R where the field blows up.  Since the field is
%always above our current plane, we can simply set wire_thickness
%to 0
wire_thickness = 0;


%since the field is going to be summed up from each wire, we need
%to initialize these variables to 0
Bx = zeros(npx,npy,npz);
By = zeros(npx,npy,npz);
Bz = zeros(npx,npy,npz);


%initialize the coords of the grid
xx = linspace(-lx/2,lx/2,npx);
yy = linspace(-ly/2,ly/2,npy);
zz = linspace(-lz/2,lz/2,npz);
[XX,YY,ZZ]=meshgrid(xx,yy,zz);


%loop through each contour line plotting it and summing up its
%contribution to the magnetic field
index = 1;
while(index <= size(cont,2))
    %see documentation for the matlab contour function to see how
    %the contour data is organized into the matrix cont
    level = cont(1,index);
    num_pairs = cont(2,index);
    x = cont(1,index+1:index+num_pairs);
    z = cont(2,index+1:index+num_pairs);
    y = -a*ones(size(x));

    %if x or z exceeds the size of the coil, don't include this
    %contour
    if(~isempty(find(abs(x)>cx/2)))
        index = index+num_pairs+1;
        continue
    end
    if(~isempty(find(abs(z)>cz/2)))
        index = index+num_pairs+1;
        continue
    end

    %need to determine which way the current is flowing in the
    %loop.  this is determined by the sign of the level.  We want
```

```matlab
%to plot loops of oppossite current flow in different colors.
%z and y are switched in this case so it's plotted in the
%more natural coordinate system where z points up.
if(sign(level) == -1)
    plot3(x,z,y,'b');
    hold on
else
    plot3(x,z,y,'r');
    hold on
end

%whether or not the level is positive or negative, matlab
%arbitrarily describes the curve in either direction so we
%need to determine which way the points describing the
%contour line were entered in the vector and make them
%correlate to the direction of the current
if(sign(level) == 1)
    %determine the cross product of two consecutive points
    %from a reference point in the center of the coil. The
    %sign of this value will tell the direction of the
    %current as it currently is in the vector. This method
    %of using the mean of the x and z values may not work if
    %the coil has sharp features
    cr = cross([x(1)-mean(x),y(1)-mean(y),z(1)-mean(z)],...
        [x(2)-mean(x),y(2)-mean(y),z(2)-mean(z)]);

    %if the vector is backwards, flip it
    if(sign(cr) == -1)
        x = fliplr(x);
        y = fliplr(y);
        z = fliplr(z);
    end
else
    cr = cross([x(1)-mean(x),y(1)-mean(y),z(1)-mean(z)],...
        [x(2)-mean(x),y(2)-mean(y),z(2)-mean(z)]);
    if(sign(cr) == 1)
        x = fliplr(x);
        y = fliplr(y);
        z = fliplr(z);
    end
end

%The program CoilField.exe takes in a text file as its input.
%This file must be tab-delimited ASCII formatted in the
%following way
```

```
% x_min          x_max          x_step
% y_min          y_max          y_step
% z_min          z_max          z_step
% coil_length    0              0
% wire_thcknss   0              0
% x_coil_1       y_coil_1       z_coil_1
% x_coil_2       y_coil_2       z_coil_2
% ...            ...            ...
% x_coil_N       y_coil_N       z_coil_N
M = [min(xx) max(xx) xx(2)-xx(1);...
     min(yy) max(yy) yy(2)-yy(1);...
     min(zz) max(zz) zz(2)-zz(1); num_pairs, 0, 0;...
     wire_thickness,0,0; x' y' z'];
output_file = 'Coil.txt';
dlmwrite(output_file,M);


%Run the fortran program 'CoilField.exe' passing the coil
%text file
eval(['!CoilField_' output_file])

%Open the output data file from the CoilField program and
%process it into a 4d matrix
fp = fopen('b1_field.dat','r');
field = fread(fp,'double');
field = reshape(field,npx,npy,npz,6);
Bx = Bx + field(:,:,:,4);
By = By + field(:,:,:,5);
Bz = Bz + field(:,:,:,6);
fclose(fp);

index = index+num_pairs+1;

%pause for a millisecond in case we want to abort with ctrl C
pause(0.01);
end

%scale the field (mu0/4pi)*10^4 Gauss/Tesla
Bz = Bz*1e-3;

%plot the field and rotate it to the more natural coordinate
%system where z points up
H = slice(XX,YY,ZZ,Bz,[],[0],[0]);
shading interp
rotate(H,[1 0 0],90);
```

```
xlabel('x [m]');
ylabel('z [m]');
zlabel('y [m]');

axis equal
```

A.2 Biot-Savart calculation

Fortran code used to numerically evaluate the Biot-Savart law for an arbitrarily shaped coil. This code requires formatted input in the form of a text file. The formatting is described in the source code in section A.1.

```fortran
!**********************************************************************
!
!   CoilField.f90
!
!   FUNCTIONS:
! CoilField       - Entry point of console application.
! cross       - Calculates the cross product between two
!                     vectors
! norm       - Calculates the norm of a vector
! calculate_b1   - Calculates the magnetic field (b1) at a
!                     given point
!
!**********************************************************************
!
!   PROGRAM: CoilField
!
!   PURPOSE: Caclulates the magnetic field from an arbitrary coil
!
!**********************************************************************

 program CoilField
   !declare variables
   double precision, dimension(3) :: v1, v2, cp, b1, point,&
           x_range, y_range, z_range
   double precision :: mag, x_step, y_step, z_step, &
                       wire_thickness
   integer coil_length, x_length, y_length, z_length, &
           x_index, y_index, z_index
   double precision, dimension (:,:), allocatable :: coil
   double precision, dimension (:,:,:,:), allocatable :: &
```

```
                        field
character *100 filename

!get the filename for the coil input from the command
      !line argument
call getarg(1 , filename)

!open the coil file and read in the x_range , y_range ,
      !z_range , coil_length , and wire_thickness
open (unit = 1, file=filename)
read(1,*) x_range(1), x_range(2), x_range(3)
read(1,*) y_range(1), y_range(2), y_range(3)
read(1,*) z_range(1), z_range(2), z_range(3)
read(1,*) coil_length
read(1,*) wire_thickness

!determine the length of each dimension
x_length = ((x_range(2)-x_range(1)))/x_range(3)+1
y_length = ((y_range(2)-y_range(1)))/y_range(3)+1
z_length = ((z_range(2)-z_range(1)))/z_range(3)+1

!allocate memory for dynamic arrays coil and field
allocate(coil(coil_length ,3))
allocate(field(x_length ,y_length ,z_length ,6))

!read in the coil array from the coil file
do i=1,coil_length
 read(1,*) coil(i,1), coil(i,2), coil(i,3)
end do

!loop through the physical dimensions
!y comes before x in order to make the output comparable
      !to meshgrid in Matlab
y_loop: do y = 1, y_length
 x_loop: do x = 1, x_length
  z_loop: do z = 1, z_length

    !determine the values of x, y, and z for the
                  !grid
    point(1) = x_range(1) + (x-1)*x_range(3);
    point(2) = y_range(1) + (y-1)*y_range(3);
    point(3) = z_range(1) + (z-1)*z_range(3);

    !calculate the b1 vector for the current
                  !point
```

```fortran
      call calculate_b1(coil_length, coil, &
          wire_thickness, point, b1)

      !store the x, y, z, u, v, w values for
                      !the current point
      field(y,x,z,1) = point(1)
      field(y,x,z,2) = point(2)
      field(y,x,z,3) = point(3)
      field(y,x,z,4) = b1(1)
      field(y,x,z,5) = b1(2)
      field(y,x,z,6) = b1(3)

    end do z_loop
   end do x_loop
 end do y_loop

 !dump the field 4d array to a binary file 'b1_field.dat'
      inquire(iolength=itemp) field
      open(unit = 2,file='b1_field.dat')
      close(2,status='delete')
      open(unit = 2,access='direct', &
  file='b1_field.dat',recl=itemp,status='new')
      write(2,rec=1) field
      close(2)

end program CoilField

!calculates the cross product of two vectors, vec1 and vec2
subroutine cross(vec1, vec2, cross_product)

 double precision, dimension(3) :: vec1, vec2, &
              cross_product

 cross_product(1) = vec1(2)*vec2(3)-vec1(3)*vec2(2)
 cross_product(2) = vec1(3)*vec2(1)-vec1(1)*vec2(3)
 cross_product(3) = vec1(1)*vec2(2)-vec1(2)*vec2(1)

 return

end subroutine cross

!calculates the norm of a vector, vec
subroutine norm(vec, mag)

 double precision, dimension(3) :: vec
```

```fortran
 double precision :: mag

mag = sqrt(vec(1)*vec(1) + vec(2)*vec(2)+vec(3)*vec(3))

 return

end subroutine norm

!calculates the magnetic field at a given point
subroutine calculate_b1(coil_length, coil, wire_thickness, &
                        point, b1)

 integer :: coil_length
 double precision, dimension(coil_length, 3) :: coil
 double precision, dimension(3) :: b1, point, dl, radius,&
                       cp
 double precision :: mag, wire_thickness

 b1 = 0

 !integrate over the coil geometry
 all: do i=1,coil_length-1
  !determine the finite difference, dl for the coil
  dl(1) = coil(i+1,1)-coil(i,1)
  dl(2) = coil(i+1,2)-coil(i,2)
  dl(3) = coil(i+1,3)-coil(i,3)

  !determine the radius from the coil to the given
          !point
  radius(1) = point(1)-coil(i,1)
  radius(2) = point(2)-coil(i,2)
  radius(3) = point(3)-coil(i,3)

  !determine dl x radius
  call cross(dl, radius, cp)

  !determine the norm of this cross product
  call norm(radius, mag)

  !calculate |r|^3
  denom = mag*mag*mag

  !set b1 to 0 if it is too close to the coil
  if(mag<wire_thickness) then
   b1(1) = 0
```

```
   b1(2) = 0
   b1(3) = 0
   continue
 else
  b1(1) = b1(1) + cp(1)/denom
  b1(2) = b1(2) + cp(2)/denom
  b1(3) = b1(3) + cp(3)/denom
 end if

 end do all

 return

end subroutine calculate_b1
```
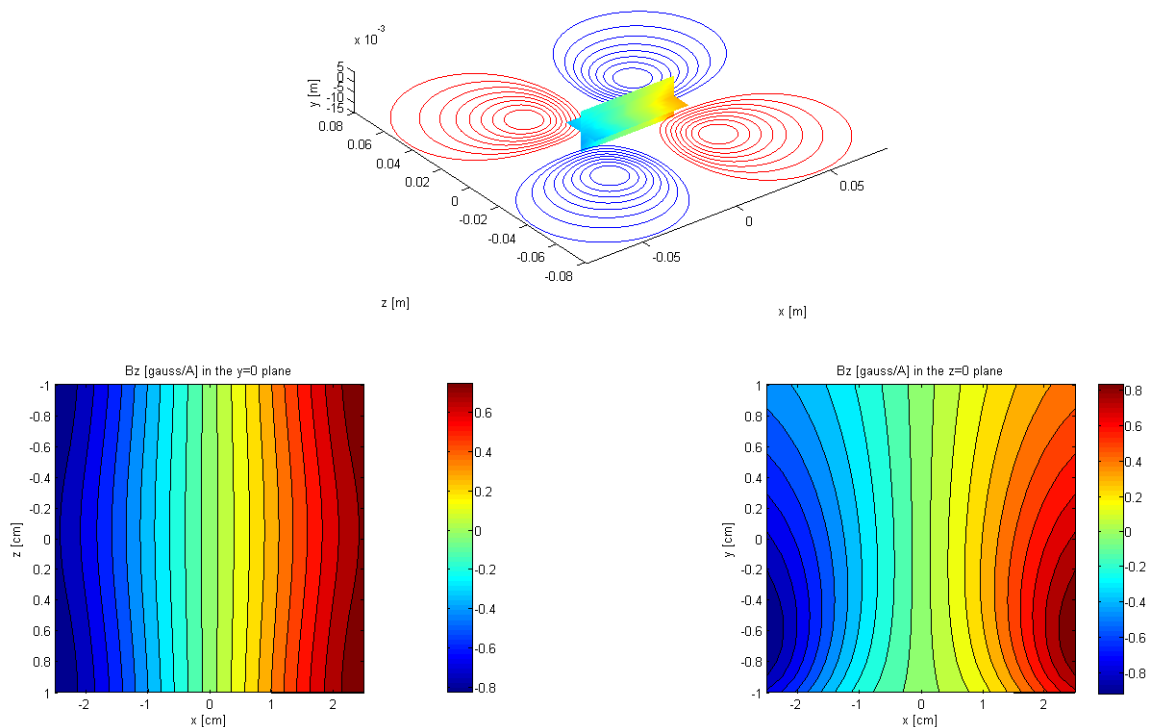
A.3 Sample output

Figure A.1: Sample output from the gradient optimization code. The top figure is a three dimensional representation of the winding pattern with the calculated field centered above it. The two figures on the bottom are contours of the calculated field in the y=0 and z=0 plane.

Appendix B

Composition enhancement through gas extraction

When performing a xenon signal amplification by gas extraction (SAGE) experiment as discussed in chapter 4, an additional enhancement can be obtained when working with gas mixtures. Typically mixtures of xenon, nitrogen, and helium are used for optical pumping. For the sake of simplicity we'll examine a mixture of xenon and helium only. The composition enhancement is intuitively realized when considering two scenarios for a SAGE experiment: one in which the extraction pressure in the second membrane matches the input pressure of the first membrane, and the other in which the extraction is carried out under a perfect vacuum. In the first scenario, the concentrations of xenon and helium in solution after passing through the first membrane are dictated by Henry's law and proportional to the partial pressure of each gas. Inversely, upon entering the extraction membrane, the partial pressure of each extracted gas will be proportional to the concentration of each gas in solution. Since the overall pressure in each membrane is the same, the composition of the gas from the input membrane to the extraction membrane does not change. However, in the second scenario, the gas is extracted under a perfect vacuum and the composition of the extracted gas therefore reflects the concentrations of the gases in solution. Because xenon is more soluble than helium, this composition is enhanced.

In a typical SAGE experiment, the extraction pressure is some finite value, lower than the input pressure. To calculate the composition enhancement, we will use the following model. A volume of liquid, V_l, is initially saturated with xenon and helium at concentrations of $[Xe]_i$ and $[He]_i$ respectively. Instantaneously, the airspace is removed and the volume of liquid is placed in a constant pressure piston container, with the piston initially at the surface of the liquid. As the solution outgasses and comes to equilibrium, a volume of gas, V_g, displaces the piston. The pressure of the gas, P_{tot}, is composed of the partial pressures of the extracted xenon and helium, P_{Xe} and P_{He}.

$$P_{tot} = P_{Xe} + P_{He} \tag{B.1}$$

From Henry's law, we have

$$[Xe]_f = K_{Xe}P_{Xe} \tag{B.2}$$

and

$$[He]_f = K_{He}P_{He} \tag{B.3}$$

where $[Xe]_f$ and $[He]_f$ are the final concentrations of xenon and helium in solution at equilibrium, and K_{Xe} and K_{He} are the solubility constants of xenon and helium. Through the conservation of mass, we know the initial quantity of xenon that was dissolved in solution must equal the quantity of xenon left in solution plus the quantity of xenon in the gas phase.

$$[Xe]_f V_l + \frac{P_{Xe}V_g}{RT} = [Xe]_i V_l \tag{B.4}$$

and similarly for helium

$$[He]_f V_l + \frac{P_{He}V_g}{RT} = [He]_i V_l \tag{B.5}$$

Equations B.1-B.5 represent a system of five equations with five unknowns: P_{Xe}, P_{He}, $[Xe]_f$, $[He]_f$, and V_g. Upon solving this system of equations, the liquid volume V_l drops out and we arrive at a quadratic equation for P_{Xe}.

$$(K_{Xe} - K_{He})P_{Xe}^2 + [(K_{He} - K_{Xe})P_{tot} - [Xe]_i - [He]_i]P_{Xe} + P_{tot}[Xe]_i = 0 \tag{B.6}$$

Evaluating this expression for the two scenarios described above produces the expected results. These equations can be expanded to include a third gas in the mixture, such as nitrogen. The solution to the equations involving a mixture of three gases is cubic with respect to P_{Xe}.

Appendix C

Hyper-SAGE probe technical drawings

Figure C.1: Hyper-SAGE compression probe
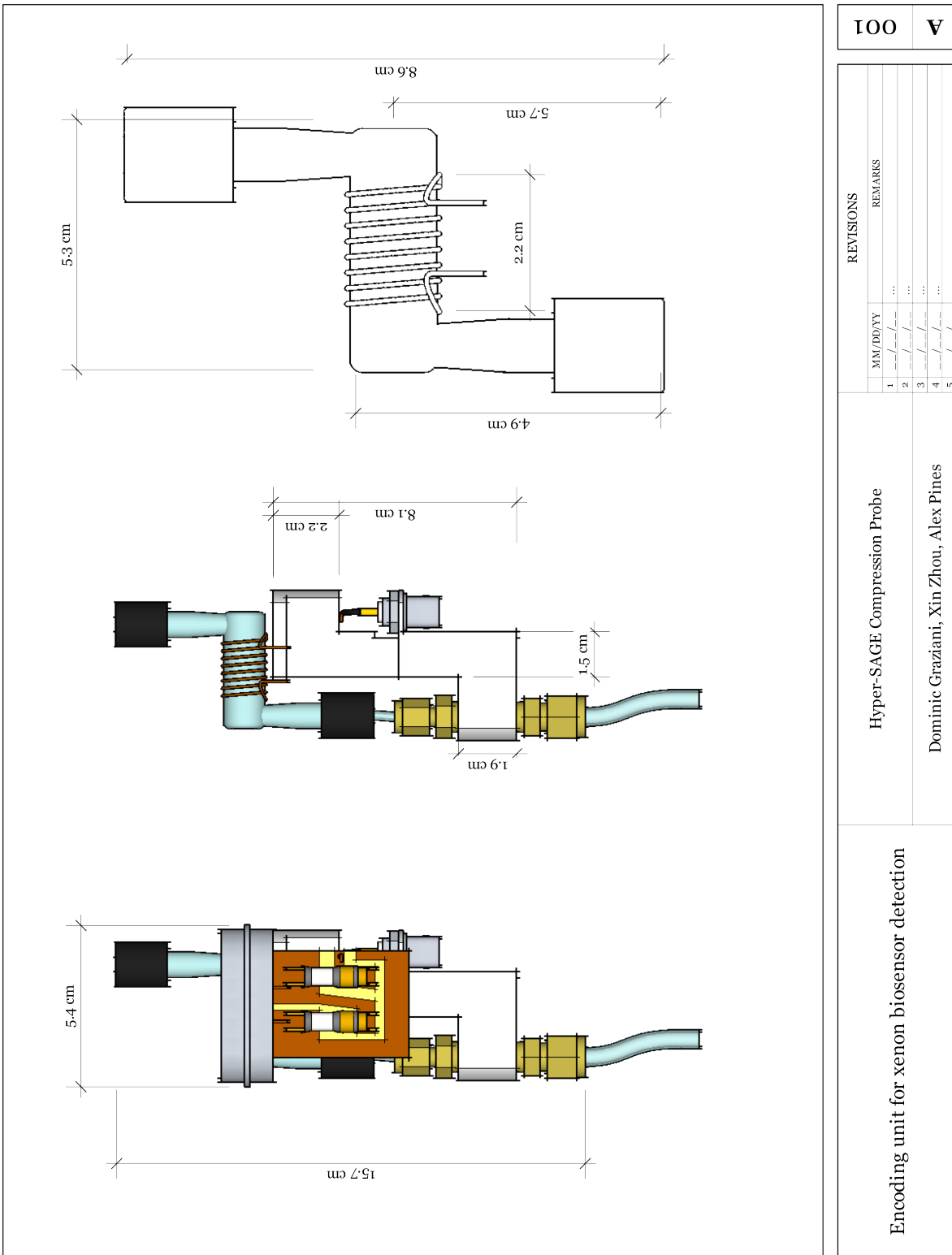
Figure C.2: Encoding region dimensions

The following dimensions and labels appear within the technical drawing:

4.5 cm

0.6 cm

1.2 cm

5.3 cm

7.8 cm

7.1 cm

5.4 cm

6.3 cm

1.0 cm

5.1 cm

REVISIONS

REMARKS

MM/DD/YY

Hyper-SAGE Compression Probe

Dominic Graziani, Xin Zhou, Alex Pines

Detection unit with valve coil

A   001
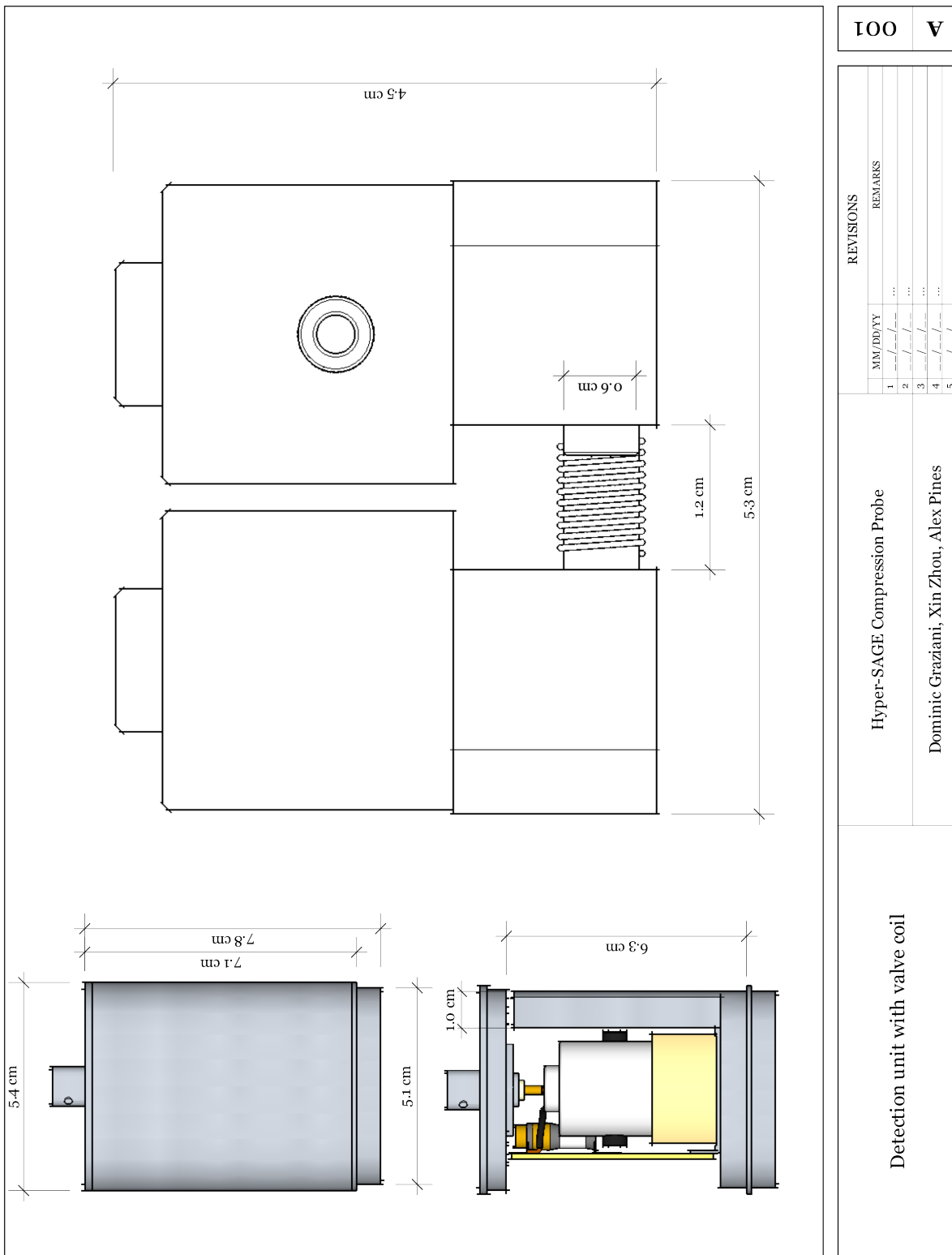
Figure C.3: Detection region dimensions

Figure C.4: Non-magnetic custom valves